Liquid Aerosol Photochemistry

A thesis
submitted in partial fulfilment
of the requirements for the Degree
of
Doctor of Philosophy in Chemistry
in the
University of Canterbury

by

David L. Bones

University of Canterbury
2008

Acknowledgements

A big thank you to Professor Leon Phillips for inspiring me and guiding me through this project. Thank you also to my family: Dad, Mum and Helen, for keeping me as sane as I ever was and for plenty of proof reading.

Thank you to Dr Colin Freeman and Professor Barbara Finlayson-Pitts for your suggestions and guidance as well as the last-minute proof reading. Georgina and Ron lit up the Chemistry social scene, but everyone in the Phillips Group and the Finlayson-Pitts group has been great to work with. Huda, it was a pleasure to be able to work with you on your smog chamber experiments.

This experiment would have got nowhere without the technical support from the department: Sandy, Danny, Nick, Russell, Gill, Rob and Roger all provided vital help.

This project was supported by the Marsden Fund. The exchange to Irvine, California was courtesy of AirUCI, which is funded by the National Science Foundation.

Contents

1 Introduction **1**

1.1 The polluted troposphere 2

1.1.1 The role of the hydroxyl radical in the atmosphere 4

1.1.2 Photochemistry 6

1.2 Tropospheric aerosol 9

1.2.1 Sources of atmospheric aerosol 9

1.2.2 Ammonium nitrate aerosol in the fine mode 11

1.2.3 Processing of natural aerosol into secondary nitrate aerosol: a tale of two cities 11

1.2.4 Aerosol concentration, particle size and composition 13

1.3 Motivations for the present study 15

1.3.1 Enhancement of light intensity in aerosols 16

1.3.2 Diffusion and mass transport across interfaces 19

1.4 Aim 20

1.5 Light intensity in an aerosol chamber 22

1.5.1 The Beer-Lambert law for a one-phase system 22

1.5.2 Extinction and absorption in ensembles of particles 23

1.6 Diffusion and mass transport in droplets 27

1.6.1 Gas uptake 27

1.6.2 Gas phase diffusion 28

1.6.3 Transport across the interface and diffusion within the droplet . . 28

1.7 Comparison with previous experiments 29
1.7.1 Smog chambers and aerosol flow tubes 29
1.7.2 Investigations of nitrate photochemistry 31
1.7.3 Radical scavengers 31

2 Experimental: Flow chamber and particle size distribution 33
2.1 History of the experimental set-up 33
2.1.1 Modifications to Knox's set-up 34
2.2 Aerosol flow chamber 35
2.2.1 Chamber specifications 35
2.2.2 Aerosol behaviour during transport 37
2.2.3 The aerosol nebuliser 41
2.2.4 Downstream impactor 42
2.2.5 Upstream impactor 44
2.2.6 Solution reservoir 45
2.3 Flow meters 45
2.3.1 MKS flow meters 48
2.4 Aerodynamic Particle Sizer 49
2.4.1 Principles of operation 49
2.4.2 Aerosol Instrument Manager 50
2.4.3 Dilution of flow 51
2.4.4 Tests of the APS with the VOAG 53
2.5 Optics 53
2.5.1 Lamp 53
2.5.2 Optical path 53
2.5.3 Filters 56
2.5.4 Light exclusion 56
2.6 Other instruments 57

2.6.1 Vaisala humidity meter 57
2.6.2 Baratron manometer 57
2.6.3 Carbon monoxide detector 57
2.7 Materials 58
2.8 Statistical descriptions of particle size distributions 58
2.8.1 Displaying particle size distributions with frequency histograms . 58
2.8.2 Log-normal particle size distributions 60
2.9 Particle size distribution characterisation 63
2.9.1 Experimental set-up for measurement of particle size distributions with the APS 63
2.9.2 Operational issues 65
2.9.3 Median particle diameter 66
2.9.4 Particle size distribution changes over time 70
2.9.5 Mass-weighted particle distribution 71
2.9.6 Total particle concentration 72
2.9.7 Calculations of geometric mean and standard deviation 74

3 Experimental: Actinometry 77

3.1 Chemical actinometers 78
3.1.1 Potassium ferrioxalate 78
3.1.2 Alternative actinometers 80
3.2 Experimental procedures 81
3.2.1 Analysis of ferrioxalate actinometer 82
3.2.2 Calibration of spectrometer 84
3.2.3 Precautions necessary for ferrioxalate actinometry 84
3.2.4 Effect of ionic strength of solution 85
3.2.5 Measurement of total iron deposited on walls of chamber 86
3.3 Calculations 86

4 Experimental: Measurement of gas phase hydroxyl radical yields 87

4.1 Inline gas phase analysis with carbon monoxide as radical scavenger . . . 87

4.1.1 Residual Gas Analyser . . . 87

4.1.2 Experimental set-up and procedure . . . 91

4.1.3 Composition of aerosols studied . . . 97

4.1.4 Analysis and calculations . . . 100

4.1.5 Wall effects . . . 104

4.1.6 Filter bandwidth . . . 105

4.2 Inline gas phase detection with cyclohexane as radical scavenger . . . 105

4.2.1 Analysis . . . 108

4.3 Offline gas phase detection with carbon monoxide as radical scavenger . . 108

4.4 Benzene as a radical scavenger; offline analysis . . . 112

4.4.1 Attempts to trap gas phase phenol . . . 112

4.4.2 Measurement of hydroxyl radical with trapped phenol . . . 113

5 Experimental: Aqueous phase measurement of hydroxyl radical 115

5.1 Nitrate/scavenger solutions as actinometers . . . 115

5.2 Method . . . 116

5.3 High Performance Liquid Chromatography (HPLC) . . . 116

5.3.1 HPLC theory . . . 117

5.3.2 Shimadzu HPLC . . . 118

5.3.3 HPLC calibration . . . 119

5.3.4 Detection of peaks . . . 120

5.3.5 Acidification of samples . . . 120

5.3.6 Internal standard . . . 123

5.4 Calculations . . . 124

5.5 Benzene as an aqueous phase radical scavenger . . . 125

5.5.1 Nitrate concentration analysis with the UV-visible spectrometer . 126

5.5.2 HPLC analysis . . . 126
5.5.3 Nitrate analysis with the HPLC . . . 126
5.5.4 Product concentration calculations . . . 130
5.6 Summary of experimental chapters . . . 130

6 Results and discussion 131
6.1 Particle size distribution trends . . . 132
6.1.1 Particle concentration for concentrated nitrate solutions . . . 132
6.1.2 Particle concentration for dilute nitrate solutions . . . 133
6.1.3 Particle size distributions of potassium ferrioxalate aerosol . . . 133
6.1.4 Median and geometric mean of particle size distributions . . . 133
6.1.5 Aerosol absorption coefficients . . . 134
6.2 Actinometry results . . . 137
6.2.1 Bulk phase actinometry results . . . 137
6.2.2 Aerosol phase actinometry results . . . 138
6.3 Aqueous phase radical scavenger . . . 141
6.3.1 Bulk liquid results . . . 141
6.3.2 Aerosol results . . . 143
6.4 Gas phase results . . . 147
6.4.1 Carbon monoxide as the radical scavenger . . . 147
6.4.2 Comparison with aqueous phase scavenger experiments . . . 149
6.4.3 Cyclohexane as the radical scavenger; inline detection of products 150
6.5 Benzene as an aqueous phase radical scavenger . . . 151
6.6 Physical processing of the aerosol droplets . . . 152
6.7 Comparison of radical scavenger systems . . . 153
6.7.1 Cyclohexane compared with carbon monoxide . . . 153
6.7.2 Relative yields in the gas and aqueous phases . . . 154
6.8 Experimental limitations . . . 156

6.9 Future work 157

7 Conclusion **159**

7.1 Techniques used 159

7.2 Summary of results 160

A Aerosol smog chamber experiments at UC, Irvine **162**

A.1 Sulfur dioxide and marine aerosol 162

A.2 Previous DRIFTS experiments 164

A.2.1 DRIFTS cell 164

A.2.2 Investigation by Shaka' into the uptake and reaction of sulfur dioxide on deliquesced salts 165

A.3 Uptake and processing of sulfur dioxide on NaCl aerosol 165

A.3.1 Instrumentation 165

A.3.2 Calibration of long path cell 167

A.3.3 Experimental procedure 167

A.4 Analysis and results 168

References **171**

Abstract

Aerosols of nitrate solutions were irradiated in the presence of radical scavengers in an attempt to measure the yield of hydroxyl radical in both the aqueous phase and the gas phase. Carbon monoxide, benzoic acid, benzene and cyclohexane were used as scavengers to trap hydroxyl radical. The products from the reaction of these scavengers with hydroxyl radical were analysed with High Performance Liquid Chromatography and mass spectrometry. The radiant flux in the chamber was measured via ferrioxalate actinometry, both with bulk liquid and aerosol droplets. Many quantitative results were obtained but several anomalies were found. This suggests that Mie theory is not capable of predicting rates of photochemical reactions within droplets.

"Science ... is a thin flame of reason burning across ample reservoirs of ignorance"
- Robert P. Kirshner, *The Extravagant Universe*

Chapter 1

Introduction

This thesis focuses on a photochemical liquid phase reaction: the production of hydroxyl radical from the solvated nitrate anion. Nitrate is a common component of atmospheric particulate matter and its liquid phase photochemistry has been well studied [1]. The concentration of the hydroxyl radical has been termed the fundamental measure of oxidative capacity of the atmosphere: it is a key species in the NO_x-O_3-VOC[1] cycle responsible for photochemical smog. A better understanding of the sources (and sinks) of the hydroxyl radical will aid greatly in the understanding of tropospheric chemistry, particularly that of polluted urban environments. The aim of this project was to measure the yield of hydroxyl radical from irradiated sodium nitrate aerosol and to discover if there was any enhancement in the yields from the aerosol.

The presence of photochemically active species in an aqueous aerosol could result in a large yield of gas phase products, since not only is there the potential for interfacial or multiphase chemistry, but also the radiant flux within the aerosol droplets would be enhanced at particular locations, depending on wavelength, due to a combination of refraction effects and resonance enhancements inside the droplets [2, 3]. Although the production of hydroxyl radical from nitrate in the snowpack has received some attention [4], there has been relatively little interest in the photolysis of nitrate in aqueous atmospheric aerosol [5].

In this chapter, Section 1.1 introduces the polluted urban atmosphere and explains its basic gas phase chemistry. The hydroxyl radical is introduced and its photochemical sources are discussed. Section 1.2 introduces aerosols, explains their importance, what creates them and what they are composed of and gives some examples of where they occur. Section 1.3 details the specific motivations for this study: the reasons why nitrate

[1]VOC stands for Volatile Organic Compound. NO_x stands for NO plus NO_2.

aerosol may be a significant source of hydroxyl radical, in terms of enhancements in light intensity and a reduced solvent cage effect. This leads to Section 1.4 which explains the aims of this project. Sections 1.5 and 1.6 introduce the mathematics of absorption in aerosols and the diffusion of gaseous compounds within droplets respectively. The final section is a brief review of similar experiments from the published literature.

1.1 The polluted troposphere

The troposphere is the section of the atmosphere extending from the surface of the earth to the tropopause, at a height of around 10 to 15 kilometres above sea level. The troposphere is characterised by a negative temperature gradient; the higher one goes, the lower the temperature becomes, until one reaches the tropopause where the temperature gradient becomes positive.

The chemistry of even the remote atmosphere is changing due to anthropogenic emissions; long lived anthropogenic pollutants can be transported great distances. While in all but the most extreme cases the resulting mixing ratios are those of so called 'trace' gases, the effects on the environment and on human health can be serious, particularly on a local scale. Trace gases, especially volatile organic compounds (VOC) are responsible for the complex tropospheric ozone chemistry that results in photochemical smog. VOC are of particular interest because of their role in tropospheric ozone chemistry and because of concerns about their effects on human health and the environment. The major fraction of these pollutants comes from incomplete combustion in automobile engines.

Other important pollutants, also resulting from the combustion process in automobile engines, are nitric oxide (NO) and nitrogen dioxide (NO_2). Together, these compounds are classed as 'NO_x', or reactive odd nitrogen. The complex chemistry involved in the catalytic oxidation of volatile organic compounds by NO_x and ozone is responsible for photochemical smog, the brown haze commonly seen over major cities.

The hazy nature of smog is due in part to the particulate matter (PM) it contains; the brown colour is partly due to nitrogen dioxide. The volatile components (primary, from automobile emissions and secondary, from subsequent reactions) can condense to form liquid and solid aerosols (particulate matter). As well as obscuring visibility,

United States National Ambient Air Quality Standards		
Pollutant	24-hour standard	Annual standard
$PM_{2.5}$	$35\,\mu g\,m^{-3}$	$15\,\mu g\,m^{-3}$
$PM_{10-2.5}$	$70\,\mu g\,m^{-3}$	none
New Zealand National Environmental Standards		
PM_{10}	$50\,\mu g\,m^{-3}$	$20\,\mu g\,m^{-3}$

Table 1.1: National air quality standards of the United States and New Zealand [10, 11].

particulate matter has also been found to cause chronic respiratory problems and premature mortality [6]. The air-quality standard 'PM_{10}' refers to all particulate matter below 10 micrometres (μm) in diameter. Recently, $PM_{2.5}$ was defined as a more specific measure when it was recognised that particulate matter smaller than $2.5\,\mu$m in diameter could have important additional health implications since it is small enough to penetrate as far as the alveolar region of the lungs [7].

Primary emissions are not typically the direct sources of the chemicals which have the worst effects on human morbidity and mortality. A wide range of non-mutagenic organic compounds react in the presence of sunlight and nitrogen oxides to form mutagenic compounds. Toluene is one of many non-mutagenic volatile organic compounds that will produce peroxyacetal nitrate, formaldehyde, methyl gloxal and nitrocresols when irradiated in the presence of NO_2, all of which are mutagens or suspected mutagens [8].

Ozone itself has been implicated as a health hazard. Health problems attributed to ozone range from symptoms like irritation of the eyes and headaches to more serious symptoms such as lung irritation and decreased pulmonary function (breathing difficulties). Even in centres like Montreal, with relatively low average ozone concentrations ($20\,\mu g\,m^{-3}$), there is a correlation between ozone concentrations and mortality [9]. Although the average concentration of ozone measured in Montreal was low, spikes were measured at levels known to be harmful to humans (80 - $400\,\mu g\,m^{-3}$); the spike durations amounted to 5% of the total time.

To limit the concentrations of pollutants in the atmosphere, most countries have standards setting the maximum desirable levels of trace gases and particulate matter. Some of the relevant standards of New Zealand and the United States are presented in Table 1.1.

Air quality standards such as these are chosen based on the predictions of models of tropospheric chemistry. Because the chemistry of photochemical smog is so complex, it is not simply a matter of measuring the effects of a particular pollutant on human (or animal) morbidity and mortality and setting upper limits on the concentrations of this pollutant to reduce the adverse health effects to satisfactory levels. The chemical interactions of all the species in the air must be taken into account. For example, a recent model of the contribution of the gas phase oxidation of volatile organic compounds to carbon monoxide levels [12] solved kinetic rate expressions for 120 different chemical species over a 30×80×5 three dimensional grid. Models like this must include meteorological conditions and geography to accurately predict pollutant levels, but comprehensive data on chemical abundances and reaction kinetics is also vital if these models are to be of any use for modelling air pollution.

An understanding of the sources and sinks of the hydroxyl radical, the key atmospheric oxidant, is especially important given the central role it plays in the chemistry of photochemical smog.

1.1.1 The role of the hydroxyl radical in the atmosphere

The hydroxyl radical functions as a catalyst in the oxidation of volatile organic compounds (VOC) together with the nitrogen oxides (NO_x). The major consequence of this cycle of reactions is the production of ozone and highly reactive carbon-containing radicals.

Radicals are highly reactive chemical species because they have unpaired electrons. They are commonly involved as chain carriers in chain reactions since the radical reacts with other stable molecules to pair its unpaired electron and hence stabilise itself, leaving the other molecule with an unpaired electron. The other molecule goes on to react further, propagating the reaction. The chain reaction only terminates when two radicals combine to form a stable species:

$$\begin{aligned} \mathrm{X}\cdot + \mathrm{RH} &\rightarrow \mathrm{HX} + \mathrm{R}\cdot, \\ \mathrm{R_1}\cdot + \mathrm{R_2}\cdot &\rightarrow \mathrm{R_1R_2}. \end{aligned}$$

The primary source of ozone (O_3) in the atmosphere is the reaction between atomic and molecular oxygen (O_2). In the troposphere, atomic oxygen is formed when nitrogen

dioxide (NO_2) is photolysed to form nitric oxide (NO) and an oxygen atom (in the ^3P ground state). Both NO and NO_2 are stable radical species. The oxygen atom rapidly reacts with an oxygen molecule to form ozone. Ozone, however, rapidly reacts with NO to reform NO_2 and O_2, at rates sufficiently high to keep the total concentration of O_3 low [13, 14, 15]:

$$\begin{aligned} NO_2 + h\nu &\longrightarrow NO + O, \\ O + O_2 + M &\longrightarrow O_3 + M, \\ O_3 + NO &\longrightarrow NO_2 + O_2. \end{aligned} \tag{1.1}$$

If NO is being removed by another chemical species the concentration of O_3 will be much higher. This role is fulfilled by the products from the oxidation of carbon containing compounds. The simplest atmospheric carbon containing compound is carbon monoxide, CO. While CO does not react directly with NO, it can react with the hydroxyl radical (OH). OH is formed when $O(^1D)$ from the photolysis of ozone reacts with a water molecule. OH reacts with CO to form carbon dioxide (CO_2) and a hydrogen atom. The hydrogen atom reacts rapidly with molecular oxygen forming a hydroperoxyl radical (HO_2), so the effective reactions are:

$$\begin{aligned} O_3 + h\nu &\longrightarrow O_2 + O(^1D), \\ O(^1D) + H_2O &\longrightarrow 2OH, \\ CO + OH &\xrightarrow{O_2} CO_2 + HO_2. \end{aligned} \tag{1.2}$$

The HO_2 radical produced is relatively stable but will react with NO to reform NO_2 and hydroxyl radical. Thus, the net result of the oxidation of carbon monoxide is the production of ozone and carbon dioxide. The hydroxyl radical and the nitrogen oxides are recycled and can therefore be said to play a catalytic role. The major sink for these radicals is the reaction of hydroxyl radical with NO_2 to produce nitric acid:

$$\begin{aligned} HO_2 + NO &\longrightarrow NO_2 + OH, \\ NO_2 + OH &\longrightarrow HNO_3. \end{aligned}$$

The major consequence of the oxidation of carbon containing compounds is the production of alkyl peroxy radicals (RO_2) and hydroperoxyl radicals via the reaction of the hydroxyl radical with VOC [13]:

$$\begin{aligned} \mathrm{RH} + \mathrm{OH} &\xrightarrow{\mathrm{O_2}} \mathrm{RO_2} + \mathrm{H_2O}, \\ \mathrm{RO_2} + \mathrm{NO} &\longrightarrow \mathrm{RO} + \mathrm{NO_2}, \\ \mathrm{NO_2} + h\nu &\longrightarrow \mathrm{NO} + \mathrm{O}. \end{aligned}$$

Peroxyacyl nitrates (PAN) are formed when the hydroxyl radical reacts with species like acetaldehyde (CH_3CHO). Acetaldehyde, after several steps, reacts with nitrogen dioxide to produce peroxyacetyl nitrate ($CH_3C(O)O_2NO_2$, also known as PAN):

$$\begin{aligned} \mathrm{CH_3CHO} + \mathrm{OH} &\longrightarrow \mathrm{CH_3CO\cdot} + \mathrm{H_2O}, \\ \mathrm{CH_3CO\cdot} + \mathrm{O_2} &\longrightarrow \mathrm{CH_3C(O)O_2}, \\ \mathrm{CH_3C(O)O_2} + \mathrm{NO_2} + \mathrm{M} &\rightleftharpoons \mathrm{CH_3C(O)O_2NO_2} + \mathrm{M}. \end{aligned} \tag{1.3}$$

Peroxyacyl nitrates are relatively inert and insoluble. The main pathway for their removal from the atmosphere is thermal decomposition. Their lifetimes are therefore highly temperature dependent and can vary from 0.5 to 8 hours [13].

The levels of hydroxyl radical are highly variable, ranging from 10^4 to 10^8 molecules cm^{-3}. Concentrations vary greatly between locations and decrease with altitude [15]. Hydroxyl radical concentrations increase during the day, due mainly to the photochemical reactions that drive the VOC-NO_x-O_3 chemistry. Other potential sources are the photolysis of gas phase and surface adsorbed nitrous acid (HONO) and the photolysis of aqueous nitrate anions.

1.1.2 Photochemistry

Much of the chemistry happening in the Earth's atmosphere is driven by light from the sun. This is particularly true for ozone, formed in the stratosphere by the reaction of photoproduced O atoms with O_2. Other photochemical reactions play important roles lower in the atmosphere. One atmospherically relevant reaction is the photolysis of the nitrate anion (NO_3^-). Nitrate absorbs strongly at far ultraviolet wavelengths (210 nm), but also has a weak absorption at 305 nm.

The sunlight reaching the lower regions of the atmosphere has already been modified by the atmosphere. This light is said to be actinic. In the atmospheric sense, *actinic*

flux is the solar flux incident on a point inside the Earth's atmosphere, spherically integrated over all angles of incidence. Because of UV absorbing species like oxygen and ozone, in the troposphere the light is limited to wavelengths of 290 nm and longer [15]. All radiation below 200 nm is absorbed by the oxygen in the atmosphere, while ozone absorbs wavelengths between 200 and 300 nm[14].

The nitrate anion is photolysed by UV light. The UV absorption spectrum of aqueous nitrate solution shows a broad band between 260 and 330 nm, corresponding to a weak n to π^* transition (Figure 1.1). At shorter wavelengths, nitrate is very strongly absorbing, due to a π to π^* transition. Two of the major pathways arising from the weak absorption at 305 nm are [1]:

$$\begin{aligned} {NO_3}^- + h\nu &\longrightarrow {NO_2}^- + O(^3P) \\ &\longrightarrow NO_2 + O^-. \end{aligned} \tag{1.4}$$

O^- then reacts with water molecules to produce hydroxyl radical (OH):

$$O^- + H_2O \longrightarrow OH^- + OH.$$

Since this protonation of O^- is fast ($k = 1.8 \times 10^6$ L mol^{-1} s^{-1} [16]) at pH levels lower than 10, other reactions of O^- are precluded. However, it is possible that NO_2 and O^- can recombine in the solvent 'cage' of water molecules holding them together (see Section 1.3.2). Mark *et al.* [17] investigated the photochemistry of nitrate in the presence and absence of oxidisable additives, namely radical scavengers such as propanol and cyclopentane. They followed the reaction primarily by measuring the concentration of the nitrite anion, ${NO_2}^-$, produced and the concentrations of the oxidised products from the radical scavengers [17].

Previous investigations into the nitrate photochemistry in droplets have focussed on the aqueous chemistry occurring in clouds [18, 19, 20]. The concentration of nitrate varies considerably, but is around 1×10^{-4} mol L^{-1} on average. In spite of this relatively high concentration, the low quantum yields reported suggest that the nitrate anion is not an important source of hydroxyl radical in cloud waters. Cloud droplets also take up HO_2 and NO_3 radicals from the gas phase. HO_2 undergoes termination, but NO_3 can react with OH^- or Cl^- to produce the nitrate anion and eventually hydroxyl radicals [13]:

$$\begin{aligned} HO_2 + HO_2 &\rightarrow H_2O_2 + O_2, \\ NO_3 + {Cl^-}_{(aq)} &\rightarrow {NO_3}^- + Cl_{(aq)}. \end{aligned}$$

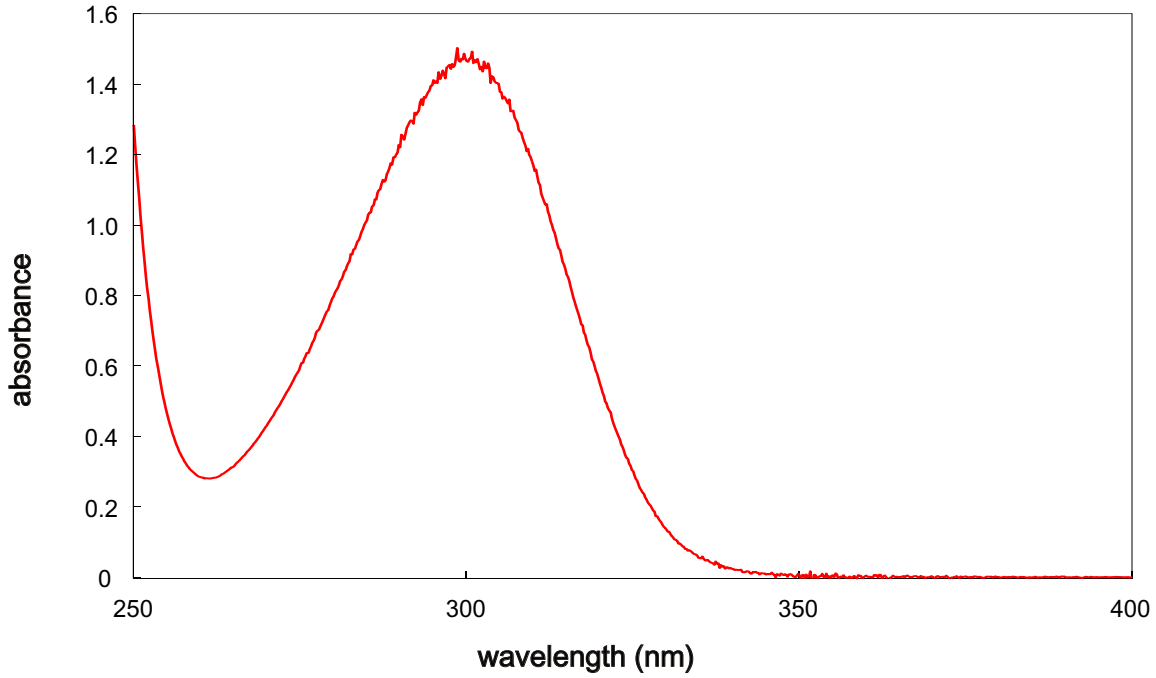

Figure 1.1: UV-visible absorption spectrum of sodium nitrate ($2\,\mathrm{mol\,L^{-1}}$, 1 mm path length).

A comparison of nitrate with nitrite suggests that nitrite might be a more important source of hydroxyl radicals. Nitrite occurs at lower concentrations in atmospheric waters than nitrate and typically is around one percent of the nitrate. However, nitrite is more photochemically active and absorbs at longer wavelengths, with an absorption maximum at 354 nm. The rate of destruction of nitrite can be calculated from the actinic flux, the quantum yield and the absorption coefficient over the actinic region of interest. This results in a rate of destruction for nitrite 70 times that for nitrate at the same concentration [21].

Reactions of adsorbed chemicals on natural and manmade surfaces have also been proposed as a source of OH. For example, nitrogen dioxide adsorbed on an aqueous layer of an atmospheric particle can react in the dark to produce HONO (nitrous acid) and nitric acid. Both of these species can be photolysed in sunlight to form hydroxyl

radical:

$$\begin{aligned} 2NO_2 &\xrightarrow{surface} HONO + HNO_3, \\ HNO_3 + h\nu &\rightarrow NO_2 + OH, \\ HONO + h\nu &\rightarrow NO + OH. \end{aligned}$$

1.2 Tropospheric aerosol

Aerosols, defined as suspensions of solid or liquid particles in a gas, are currently of interest for a number of reasons. Their potential to offset global warming has, unsurprisingly, received a lot of attention. The optical properties of aerosols mean that they are efficient scatterers of light (this will be examined in more depth in Section 1.3.1) as evidenced by the brilliant sunsets seen after volcanic eruptions like that of Mt Pinatubo in 1991 [22]. Aerosols have the potential to both heat and cool the surface of the earth. If they have a high albedo (that is, if they are reflective), they can reflect solar light back into space. Less reflective aerosols absorb more solar light and can scatter this as thermal infrared radiation in all directions, resulting in less light reaching the Earth's surface and a cooling of the atmosphere. They can also act like a greenhouse gas and scatter light reflected from the Earth's surface back to the surface, hence warming the atmosphere [13].

The total mass of aerosols in the troposphere (not including cloud droplets) has been estimated as 1.5×10^{10} kg [14]. The combined surface area of these particles is of the order of 6.6×10^{13} m^2, equivalent to 13% of the surface area of the Earth [23]. This is a vast potential surface area for heterogeneous reactions. Reactions taking place within the particles can augment the surface reactions and contribute to the unique interfacial chemistry. Aqueous nitrate aerosol is but one potential example of this. This section investigates the sources and atmospheric concentration of nitrate aerosol.

1.2.1 Sources of atmospheric aerosol

Atmospheric nitrate aerosol is formed when natural aerosols react with gaseous nitric acid (HNO_3). Similarly, sulfur dioxide (SO_2) reacts with natural aerosols to generate sulfate aerosol. The major sources of these gases are anthropogenic, and the effect

on aerosols is significant over major industrial and urban areas. The original aerosol precursor is either natural mineral dust or sea salt aerosol.

Mineral dust is transported from deserts into the atmosphere by dust storms. These are a regular seasonal occurrence in central Asia. Mineral dust from central Asia can be blown by the prevailing westerly winds as far as North America [24]. Mineral dust consists chiefly of calcium carbonate or aluminosilicates [25]. The dust particles can vary from 5 μm to 15 μm in aerodynamic diameter[2], depending on the source region [26]. The type of mineral dictates to a large extent how the particle forms and how it weathers as it is transported. For example, calcite (hexagonal-rhombohedral $CaCO_3$) is fairly resistant to weathering in dry conditions [27]. The variability in aerosol, combined with effects like gravitational settling which remove the larger particles, complicates attempts to obtain representative size distributions.

The other predominant natural aerosol, sea salt aerosol, is produced mechanically at the surface of the sea. The two major mechanisms are the bursting of bubbles and the disruption of wave crests by wind [28]. If the aerosol is formed near the coast, it may be transported over land. Here it can undergo transformation and reaction with anthropogenic pollutants.

The action of wind on the surface of the ocean produces waves. When these waves break, bubbles are formed and then rise to the surface to burst. As the film of the bubble bursts, microdroplets of sea water are ejected into the atmosphere. In addition, jet drops are formed when the cavity left behind from the bursting bubble fills back up with water and briefly forms a jet. The radii of film drops can range from 0.1 μm to 100 μm, while jet drops tend to be around 10 % of the size of the parent bubble, having radii of 30 μm or so.

The disruption of wave crests by the wind results in spume drops. These tend to be large, with radii of several hundred micrometres. However, the formation of these droplets is not well understood or well quantified. The resultant size distribution of sea salt aerosol particles from all of these processes shows a maximum at diameters from 1 to 5 μm.

Sea salt aerosols, like aerosols in general, can be removed by wet and dry deposition. Wet deposition refers to particles being removed by rain, while dry deposition is removal

[2]The aerodynamic diameter is defined as the diameter of a spherical particle of unit density with the same terminal falling velocity as the particle in question.

on a surface (the surface can be wet or dry). The residence time[3] for particles affected by wet deposition is the time between rain events, typically three days. The dry deposition rates depend much more on particle size. Particles 1 μm in diameter can have residence times of up to several weeks, long enough to be transported thousands of kilometres.

1.2.2 Ammonium nitrate aerosol in the fine mode

A third source of nitrate aerosol results from the acid-base titration of gas phase ammonia (NH_3) and nitric acid. Ammonia is produced by agriculture, in the form of animal waste, as well as from natural sources like the oceans and vegetation. The ammonium nitrate formed condenses to solid particles of submicron diameter. Aerosols of particles of this size are classified as fine mode aerosol, as distinct from 'coarse' aerosol ($PM_{10-2.5}$).

$$NH_{3(g)} + HNO_{3(g)} \longrightarrow NH_4NO_{3(s)} \tag{1.5}$$

This reaction is temperature dependent, hence a seasonal variation in concentrations of ammonium nitrate particles has been observed [13, 29].

1.2.3 Processing of natural aerosol into secondary nitrate aerosol: a tale of two cities

In this section, two particularly badly polluted areas of the world are presented as case studies for the formation of nitrate aerosol: Los Angeles and Beijing. These areas are by no means representative of the atmosphere or even of polluted urban regions. Rather, they represent the upper levels of NO_x pollution and hence nitrate aerosol concentrations to be found around the world. Many other massive cities have comparable levels of pollution.

Sea salt aerosol formed off the coast of California is blown inland by the prevailing onshore (westerly) breeze. As it passes over the urban sprawl of Los Angeles it mixes with anthropogenic pollutants. Nitrogen dioxide and nitric acid are adsorbed on the surface of the particle. They are likely to react in the aqueous surface layer of the particle, forming nitrate via several reaction pathways.

The Los Angeles basin suffers from air pollution not only because it has a high population density but also because of the natural geography. The combination of the Santa Ana

[3]The residence time is the average length of time the particles remain suspended in the atmosphere.

and San Bernadino mountains to the east, the onshore breeze from the west and the temperature inversion layer that frequently forms, traps the pollutants in the boundary layer below about 1000 m. It is not Los Angeles itself as much as the inland counties in the basin that suffer from the worst pollution, in particular Riverside and San Bernadino.

Typically the temperature of the troposphere decreases with increasing height. Certain weather conditions, however, can produce a temperature inversion layer where a parcel of warm air sits above a mass of cold air. Because the cold air is denser than the warm air, it cannot rise and is trapped beneath the warmer air. Any pollutants, gaseous or particulate, in this trapped cold air will also remain where they are. If the inversion conditions persist for some days, as is common in California, the intensity of pollution steadily increases.

Sea salt aerosol reacts with nitric acid to form nitrate and hydrochloric acid in an acid-ion exchange reaction:

$$\mathrm{NaCl} + \mathrm{HNO_3} \longrightarrow \mathrm{NaNO_3} + \mathrm{HCl}. \tag{1.6}$$

This is not the only reaction involving sea salt and nitrogen compounds. Other reactions taking place are [30, 31]:

$$\mathrm{NaCl} + 2\mathrm{NO_2} \longrightarrow \mathrm{NaNO_3} + \mathrm{ClNO}, \tag{1.7}$$

$$\mathrm{NaCl} + \mathrm{N_2O_5} \longrightarrow \mathrm{NaNO_3} + \mathrm{ClNO_2}, \tag{1.8}$$

$$\mathrm{NaCl} + \mathrm{NO_3} \longrightarrow \mathrm{NaNO_3} + \mathrm{Cl}. \tag{1.9}$$

Common characteristics of these reactions are that the mechanisms are not obvious, but are thought to involve some form of radical intermediate (for example $[\mathrm{Cl} \ldots \mathrm{NO_2}]^-$) and that they have some heterogeneous character.

Fine mode ammonium nitrate aerosol is also formed in polluted urban regions like L.A. with high NO_x levels and relatively low sulfur dioxide levels. Anthropogenic ammonia typically originates from agricultural sources. Natural sources, like vegetation and the ocean, contribute more ammonia to the global budget than anthropogenic sources. Above continents, ammonia levels as high as 10 parts per billion (ppb) have been observed.

Beijing is subject to aerosol pollution of an entirely different nature to that seen in L.A., although the pollution is also a result of the physical and human geography of the

surrounding area. Storms in the deserts of central Asia transport desert dust throughout east Asia. Beijing, in north eastern China, is particularly subject to these dust storms. Beijing also has a high population density and high and rapidly increasing levels of traffic. This combination leads to very high levels of pollution, including both nitrate and sulfate aerosols.

Nitric acid adsorbed on carbonate particles reacts with the carbonate, replacing it with nitrate:

$$2\mathrm{HNO_3} + \mathrm{CaCO_3} \longrightarrow \mathrm{Ca(NO_3)_2} + \mathrm{CO_2} + \mathrm{H_2O}. \tag{1.10}$$

So, both sea salt particles and mineral dust particles can adsorb nitrogen dioxide and nitric acid, which can then react in an adsorbed aqueous layer to form the nitrate anion and nitrous acid. While nitric acid is adsorbed by dry particles, the presence of an aqueous layer enables a significantly greater uptake of nitric acid and hence a correspondingly greater proportion of nitrate in the processed aerosol [32]. As the nitrate forms, the particle deliquesces, enabling more calcium carbonate to react with nitric acid. The formation of nitrate is also enhanced by UV light [27].

When alkaline calcium carbonate particles are transported through areas high in sulfur dioxide and nitric acid the uptake of nitrate and sulfate will be enhanced due to the high pH of the particles. The initially hydrophilic particles become hydrophobic [33]. Studies of $PM_{2.5}$ composition in Shanghai show that the nitrate and sulfate levels are much higher during winter, consistent with the levels of anthropogenic nitrogen dioxide and sulfur dioxide being higher due to greater use of coal heating in the winter [34].

1.2.4 Aerosol concentration, particle size and composition

The properties of aerosols are determined by their source, so concentration, particle size and particle composition are inextricably linked. Studies of ambient aerosol rely on compositional clues to elucidate the sources. Given the number of sources and variety of aerosols, the large amount of data generated by single-particle analyses requires factor analysis methods to arrive at useful conclusions [29].

Particle mass distributions measured at Long Beach and Riverside (coastal and inland urban regions, respectively) in California showed a peak in the number-weighted particle size distribution (see Section 2.8) at around $0.6\,\mu$m. Aerosol sampled near the sea

Source	January	April	July	October
dust	8.90	50.89	16.69	11.52
secondary nitrate	4.98	14.97	5.45	17.82
secondary sulfate	8.32	16.34	28.22	14.88
other	38.7	57.3	48.64	61.38
total	60.9	139.5	99.0	105.6

Table 1.2: Concentration, in $\mu g\,m^{-3}$, of some components of $PM_{2.5}$ aerosol, averaged from five sampling sites in Beijing [36].

contained a higher percentage of sulfate than inland aerosol, while aerosol sampled inland had a much higher percentage of nitrate than the marine aerosol. Inland samples were also significantly higher in overall particle concentration [35]. A study inland from Los Angeles (not far from Riverside) attributed 6.7% of mass of the aerosol to aged sea salt [29]. A further 38% was found to be secondary nitrate.

Several studies of particulate pollution in Beijing have been conducted. On average, secondary nitrate contributed 10% ($\pm$ 4%) of the mass of $PM_{2.5}$ aerosols. This level was seen to vary seasonally. Data from one recent study is presented in Table 1.2.

Atmospheric aerosol size distributions and chemical compositions can vary dramatically over time scales of hours. The composition of the aerosol depends not only on the source but also the route taken. Aerosol particles that have travelled through industrialised areas will have been processed by anthropogenic pollutants. Hence, local meteorological conditions, particularly the prevailing wind and amount of precipitation, determine to a large extent the concentration and composition of aerosol present [37].

In the atmosphere, the aqueous component of a particle is determined by the relative humidity (RH) and the nature of the other chemical components in the particle. For example, compounds of Mg^{2+} deliquesce at lower relative humidities than Na^{+}. The aqueous content is determined not just by the current relative humidity, but also the previous relative humidity. An ammonium sulfate particle will deliquesce once the RH reaches 80% but will not effloresce when the RH drops below 80% (Figure 1.2). The RH must be 37% before the particle effloresces. This is an extreme example of such hysteresis; in most cases the efflorescence point is 20 to 30% below the deliquescence point [15]. These effects affect not only the chemical composition of the particle, but also the manner in which the particle absorbs and scatters light, which may in turn have

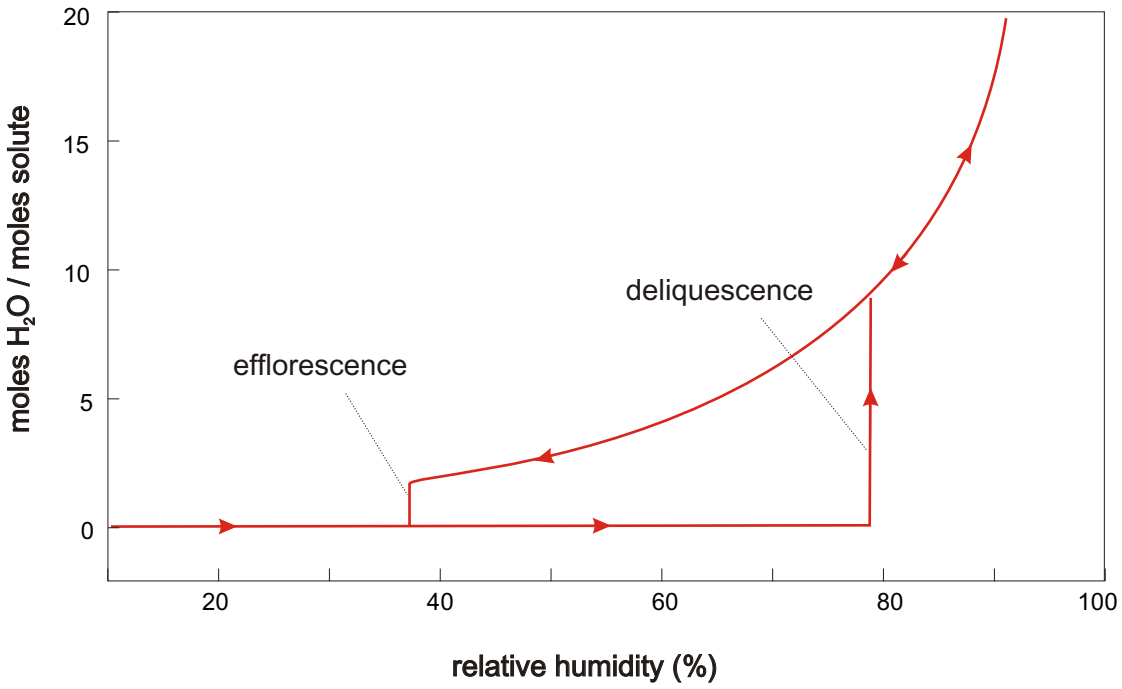

Figure 1.2: Hysteresis of particle efflorescence for ammonium sulfate particles. Adapted from [38].

consequences for its subsequent composition.

Aerosol is present in hugely varying concentrations, size distributions and compositions. Nitrate aerosol is common in the coarse mode in regions where anthropogenic NO_x has reacted with naturally formed sea salt aerosols and carbonate dusts. Los Angeles is a well studied example where sea salt was the origin of the aerosol, while Beijing exhibits severe pollution which includes NO_x processed desert dust. The percentage of water in a particle depends on the relative humidity of the area and the other chemical species present in a particle.

1.3 Motivations for the present study

The nitrate aerosol found in polluted urban regions typically consists of particles of highly concentrated aqueous nitrate solution, perhaps with a solid core. Older particles are likely to have a hydrophobic outer layer derived from VOC. When this aerosol is irradiated with ultraviolet light, photolysis of the nitrate occurs, generating hydroxyl radical. It seemed possible that the yield of hydroxyl radical in the aerosol droplets is

enhanced due to light intensity enhancements within the droplets and due to the escape of hydroxyl radical into the gas phase being facilitated by the absence of a complete solvent cage at the surface of the droplet.

1.3.1 Enhancement of light intensity in aerosols

The distribution of light within the droplets of an aerosol will not be homogeneous. Small particles with diameters approaching the wavelengths of visible and ultraviolet light scatter the majority of the incident light by reflection, diffraction and refraction (including the evanescent wave). Internal refraction of the light within the particles also occurs. This is significant since the wavelengths found in natural (actinic) light are those at which electronic transitions occur. The intensity of the light has been calculated to be higher just beneath the surface of the droplet than in the bulk, and is focussed at certain points near the surface [39]. However, when the intensity enhancements for broadband solar radiation are averaged over the volume of the droplet and the range of wavelengths, the overall enhancement is around 75% [3].

Unexpected chemical reactions have been seen in aerosol droplets illuminated by laser light in previous experiments at the University of Canterbury. When sulfuric acid was irradiated by an unfocussed 193 nm laser, dissolved carbon monoxide was oxidised to carbon dioxide and sulfur dioxide was formed [40]. However, pure sulfuric acid should not absorb light at 193 nm, as confirmed by *ab initio* electronic structure calculations on sulfuric acid [41]. These calculations suggested that it was necessary to consider multiphoton absorption. The focussing of laser light within the droplets generated sufficient intensity for multiphoton absorption to occur. It should be noted, though, that this process would not occur without laser radiation, so is very unlikely to be significant in the atmosphere.

Multiphoton absorption in aerosol droplets also has potential industrial applications. This provided the inspiration for a study on the potential of aqueous aerosol for catalysing the hydrogenation of alkenes, an important industrial process. In his thesis *The Photochemistry of Liquid Aerosols* [42] Knox investigated the relative enhancement of yields for such reactions as the hydrogenation of irradiated decene aerosols in the presence of catalysts like molybdenum hexacarbonyl, compared with the yields for the irradiated bulk liquid. He found evidence of significantly enhanced photolysis of molybdenum

hexacarbonyl in the aerosol phase, but no conclusive evidence of enhanced hydrogenation yields.

For his thesis, Knox also calculated the enhancement in radiant intensity within the aerosol droplets using Gustav Mie's approach to the solution of Maxwell's equations for electromagnetic radiation incident on a sphere. Mie theory, as it is called, has long been used to calculate the scattering of light from droplets. It also applies to the light refracted within a droplet [43].

Mie theory predicts that at certain wavelengths, light entering micrometre sized droplets will undergo enhancement due to resonance effects [44]. These can be thought of in terms of various modes of standing waves. Although this phenomenon is not strictly analogous to that seen in a 'whispering gallery' such as at Saint Paul's Cathedral in London, it is related. Thus the Mie resonances are also known as "Whispering Gallery Modes"[45]. The location and intensity of the modes are heavily dependent on the wavelength of the light in relation to the size of the particle. Thus, they can be expected to average out to lower enhancements when illuminated with broadband light. However, the effect of the evanescent wave, which penetrates below the droplet surface to produce additional photolysis via a significant focussing of radiation, is only slightly dependent on the wavelength of the light. Knox calculated the intensity enhancements for droplets of decene and predicted significant enhancements in the droplets, most noticeably at the front and back of the droplet (relative to the incoming light). It must be emphasised that these results hold for collimated, monochromatic light only. This is not going to be the case for the actinic spectrum, or the light produced by the xenon arc lamp which Knox used to irradiate his system.

Nissenson repeated and extended Knox's calculations [3]. His results indicated much lower overall enhancements when the contributions of modes from over the entire droplet were averaged over all wavelengths (see Figure 1.3). Knox had concentrated on the enhancements occurring along a plane at the centre of the droplet parallel to the incoming monochromatic light.

The enhancement of radiant intensity in a droplet has two components: the geometric effect, namely refraction, and the morphology-dependent resonances (MDR), as calculated by Mie theory. Without the MDR, the enhancement in intensity would be about 25% of that seen for a bulk liquid slab. With the MDR included, the enhancements can

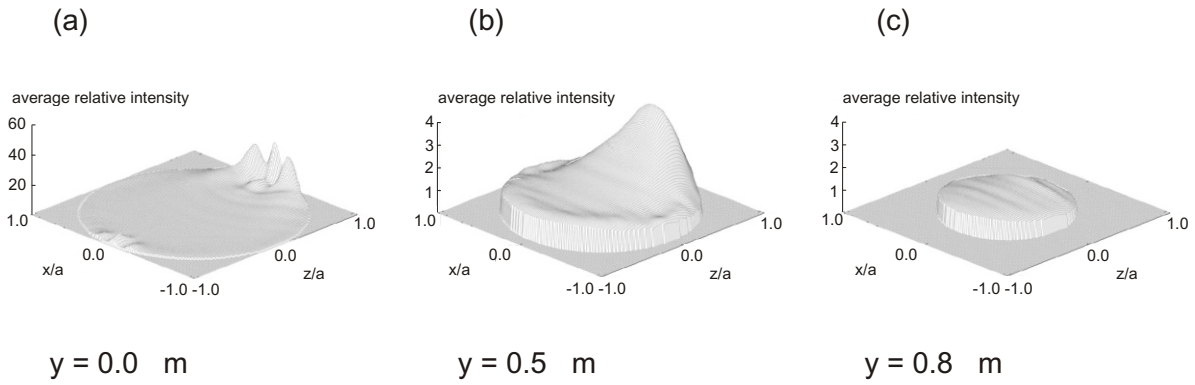

Figure 1.3: Relative intensity enhancements over three different cross sections of a water droplet 2 μm in diameter irradiated by actinic light ($\lambda = 290$ to 600 nm). The average enhancements are 2.24, 1.51 and 0.91 for (a), (b) and (c) respectively. From [3], with permission.

be up to 100% of those seen for the bulk liquid [2, 3].

Several recent studies have extended these Mie calculations to the aerosols and clouds present in the atmosphere [46, 47, 48]. Aerosol particles are at the lower end of the range of diameters expected to exhibit enhancement of radiant intensity, while cloud droplets, with diameters typically of 100 nm, are at the upper end of the range. Resonance effects are more pronounced in particles of weakly absorbing solutions. Concentrated, highly absorbing particles have refractive indices with a significant imaginary component which tends to dampen the resonances.

Computational power has been the major limiting factor in the accuracy of calculations into resonances. Mayer and Madronich [2] showed that enhancements could be over- or underestimated if the spacial resolution was too low.

Most experimental investigations of enhancements of radiant intensity within droplets have been single droplet studies with lasers as the source of the light. Symes *et al.* used the distortion of the Raman water band at 642 nm to calibrate the radiant flux of internally circulating light for sodium nitrate droplets 31 μm in diameter by varying the laser intensity. They then measured this distortion of the water band to investigate the radiant intensity of internally circulating light in droplets of aqueous nitrate of varying diameters [39].

Kitagawa and Kitamura conducted an experiment where oil droplets in an aqueous

solution were irradiated by a high pressure mercury lamp. They measured an increased quantum yield for the photocyanation of perylene. This appears to have been the first experimental demonstration of increased quantum yield due to droplet size effects [49].

The main conclusion to be drawn from these studies is that the enhancement effects are small (less than a factor of 2) when averaged over wavelength, particle size, the total volume of the droplet and plane of incidence.

1.3.2 Diffusion and mass transport across interfaces

The atmosphere is full of examples of solid-gas, liquid-gas and solid-liquid interfaces. The potential for liquid aerosols to affect the gas phase chemistry of the atmosphere is high; for example, it has been proposed as a major factor in the long term stability of the 96% CO_2 atmosphere of Venus [50]. Clearly, there is also potential for the gas phase chemistry to affect the aqueous phase chemistry of aerosols and clouds. Clouds are not often classified as aerosols, although the definition[4] technically should include them and cloud droplets interact similarly with the gas phase. Much effort has gone into trying to measure the gas uptake into cloud droplets [51]. The change in cloud pH that eventually results in acid rain is due mainly to the uptake and oxidation of sulfur dioxide.

Cloud droplets are typically on the scale of 20 to 100 μm, a size significantly larger than most tropospheric aerosol droplets, but many of the gas uptake measurements apply to both cloud waters and aerosol proper. The potential for interfacial reactions in atmospheric aerosol is comparable to that in cloud droplets, but the surface area to volume ratio of an aerosol droplet is much higher than that of a cloud droplet.

The gas-liquid interface is the boundary region between the two phases, generally considered to be on the order of a few nanometres thick [52]. For small droplets, this layer constitutes a larger percentage of the droplets' volumes than for large droplets. Aerosols fall in a grey area between gas and liquid, and can exhibit rapid mass transfer between the two phases. While nitrate photolysis is a homogeneous process, if photolysis occurs near the interface, a reduced solvent cage effect could increase the likelihood of diffusion of products such as OH into the gas phase.

[4] Aerosol: a suspension of solid or liquid particles in a gas.

Although recent molecular dynamics calculations on solutions of pure sodium nitrate have indicated that the nitrate anion is not present at the very surface of the interface [53], it is thought to be present at enhanced concentrations about 0.3 nm below the surface. Moreover, very recent physical experiments and computer simulations have suggested that in droplets of mixed solutions of sodium nitrate and sodium chloride the nitrate may indeed be found at the surface [54]. The promotion of the nitrate anion to the surface has also been suggested to occur when soluble organic compounds like benzene are present [55].

Solvent cage effect

The tendency of photolysis fragments in solution to recombine with neighbouring fragments is termed the solvent cage effect, or the Franck-Rabinowitsch effect. In bulk liquid, the solvent around the fragments holds them in place, so they are much more likely to react with each other than with other molecules. Excess energy from the photolysis will be dissipated in collisions with the solvent. The cage effect depends on the viscosity of the solvent: in solvents of high viscosity the product fragments are not able to diffuse away from each other [56, 57].

At the interface, the solvent cage around any photolysis fragments formed is less dense and the probability of the fragments escaping into the gas phase is considerably higher. This is illustrated in Figure 1.4. Because aerosol droplets have a high surface area to volume ratio, the reduction of the solvent cage effect at the surface will play a larger role in aerosol droplets than it does in bulk liquids [3].

1.4 Aim

The aim of the experiments reported in this thesis was to measure the hydroxyl radical yield from the photolysis of nitrate *in situ* in aqueous aerosol, both in the bulk solution of the droplets and the gas phase.

If the photochemical reactions described in Section 1.1.2 take place to any significant extent within aqueous atmospheric aerosol droplets, the hydroxyl and nitrite radicals[5]

[5]That is, nitrogen dioxide, NO_2.

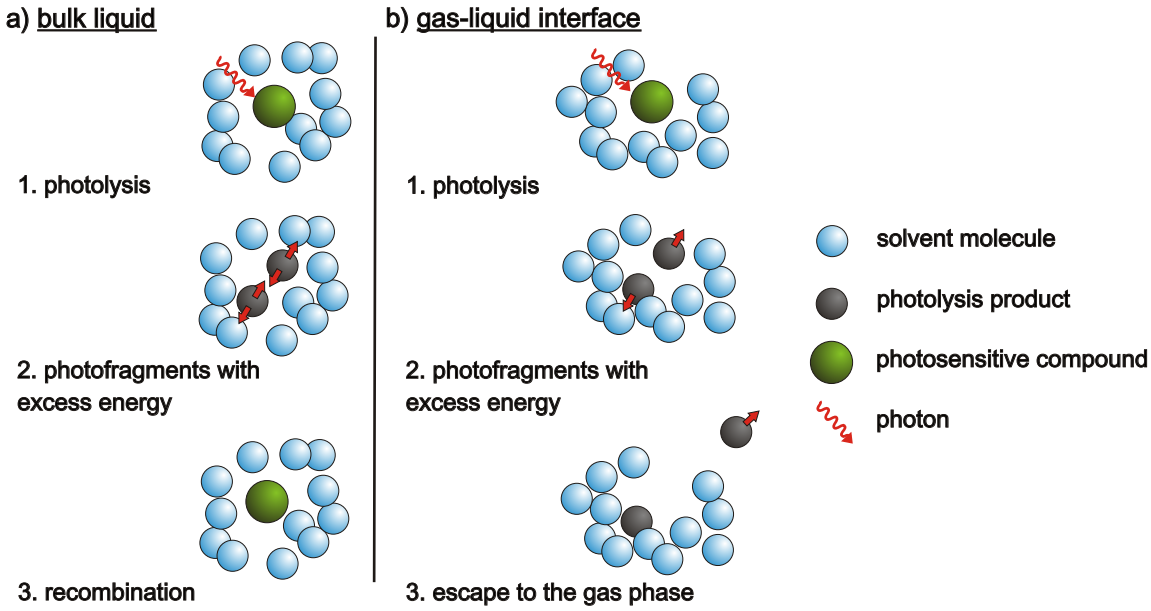

Figure 1.4: The solvent cage effect. Photolysis products in the bulk liquid (a) are less likely to diffuse to the gas phase than products at the interface (b).

produced can react further with organic components within and on the surface of the droplets.

For accurate models of atmospheric chemistry, it is necessary to know whether the tropospheric aerosols are a source or a sink of gas phase hydroxyl radical. To this end, measuring the gas phase yield of hydroxyl radical from pure nitrate aerosol would demonstrate whether the hydroxyl radical could escape the solvent cage and leave the droplet.

Hydroxyl radical produced within the droplet can react with any organic compounds present. If NO_2 or related nitrogen containing species are present, the end result could be nitrated aromatic compounds. These reactions are already known to take place in the gas phase; however, in an aerosol droplet, the proximity of the reactants to each other is much increased. In addition, unusual heterogeneous chemistry at the droplet interface could also contribute to the multitude of reactions. Measurement of the hydroxyl radical yield was via the radical scavengers carbon monoxide, for the gas phase, and benzoic acid, for the bulk solution. Carbon monoxide is not very soluble in water, so the gas

phase yield of carbon dioxide should correspond to hydroxyl radicals that have overcome the cage effect and left the surface of the droplet. The yield of products from the reaction of benzoic acid with hydroxyl radical, on the other hand, will correspond to the hydroxyl radical yields in the aqueous phase. Any enhancement in hydroxyl radical yields from sodium nitrate aerosol due solely to enhancements in light intensity within the droplets would also manifest itself in the presence of the aqueous scavenger.

1.5 Light intensity in an aerosol chamber

1.5.1 The Beer-Lambert law for a one-phase system

The standard spectrophotometric system involves a transparent cell of path length l. Light of intensity I_0 is shone into the cell, emerging with an intensity I after some fraction of light has been absorbed. The amount of light absorbed is related to the concentration of the chemical in the cell by

$$-dI = I\alpha c\, dx, \tag{1.11}$$

where I is intensity (*i.e.*, radiant flux, with units of quanta s^{-1}), $\alpha = 2.303\epsilon^*$, c is the concentration of chemical per unit volume and x is the distance travelled through the cell. For a chamber of length L,

$$-\int_{I_0}^{I_L} \frac{dI}{I} = \int_0^L \alpha c\, dx, \tag{1.12}$$

$$\begin{aligned} ln\frac{I_0}{I_L} &= \alpha cL, \\ I_L &= I_0 e^{-\alpha cL}. \end{aligned}$$

The absorbed intensity is given by

$$I_{abs} = I_0 - I_L = I_0 - I_0 e^{-\alpha cL},$$

resulting in

$$I_{abs} = I_0(1 - e^{-\alpha cL}), \tag{1.13}$$

which is the Beer-Lambert law.

*ϵ is the decadic (base 10) molar absorption coefficient, the quantity normally measured. To keep the calculations in base e, the absorption coefficient in base e, α, must be used.

Since the quantum yield of product B (Φ_B) is the yield of B per photon absorbed, the total yield n_B of molecules of B is given by

$$n_B = \Phi_B I_{abs} t,$$

where t is the time of irradiation and hence

$$I_0 = \frac{n_B}{\Phi_B\, t\,(1 - e^{-\alpha c L})},$$

or, equivalently, with a decadic absorption coefficient (ϵ) [58]:

$$I_0 = \frac{n_B}{\Phi_B\, t\,(1 - 10^{-\epsilon c L})}. \tag{1.14}$$

1.5.2 Extinction and absorption in ensembles of particles

The interaction of light with aerosols results in the attenuation of the light when the photons are absorbed or scattered. The relevant quantity in this case is the aerosol extinction coefficient, the fraction of light absorbed per unit length travelled through the aerosol. The extinction coefficient is the sum of the scattering coefficient and the absorption coefficient. Most of the efforts at calculating extinction coefficients for aerosols have focussed on the scattering of infrared light by atmospheric aerosols, in order to calculate radiative forcing for climate change models. Ultraviolet and visible wavelengths have received much less attention. The same principles apply, however, and it is possible to calculate an absorption coefficient b_{abs} for a volume of aerosol as a function of the optical properties of the aerosol particles, the particle size distribution and the particle concentration. Mie theory, mentioned in Section 1.3.1, applies when the particle diameters are approaching the wavelength of the light. From Maxwell's equations of electromagnetism, Mie's equations calculate the changes in electromagnetic radiation as it passes through and around a small spherical object. Some of the light is scattered, some is absorbed and some is unaffected. The extinction, scattering and absorption cross sections can be calculated by Mie's method [13].

The extinction cross section is the sum of the scattering and absorption cross sections:

$$C_{ext} = C_{abs} + C_{scatter}. \tag{1.15}$$

It is the effective optical size of, in this case, the particle. The particle can affect light outside its surface, so the extinction cross section can be larger than the projected area

of the actual particle. This apparent paradox is possible because for a light beam that is scattered, photochemistry is still possible even if the light beam does not actually intersect the droplet since the evanescent wave penetrates below the surface. The extinction cross section can be normalised to a dimensionless extinction efficiency, Q, *i.e.*:

$$Q_{ext} = \frac{C_{ext}}{A}, \tag{1.16}$$

where A is the physical cross sectional area of the particle. Also, it is convenient to describe a size parameter, x, a dimensionless quantity which relates the diameter of the particle and the wavelength of the light [13, 43]:

$$x = \frac{\pi d_p}{\lambda}. \tag{1.17}$$

The other parameter of interest is the complex index of refraction, m. $m = n + ik$, where n is the real part of the index of refraction and k is the imaginary part, corresponding to the absorption, or dampening, of the electromagnetic wave:

$$k = \frac{\alpha\lambda c}{4\pi} = \frac{2.303\epsilon\lambda}{4\pi}. \tag{1.18}$$

At UV wavelengths, for transparent media, k is very small. $k = 8.3\times10^{-5}$ for a $5\,\mathrm{mol\,L^{-1}}$ solution of sodium nitrate, with $\epsilon = 7.3$ at 305 nm. Only metallic substances have k higher than 10^{-3} [43]. However, many recent studies have reported high values of k for aerosols: values ranging from 0.001 to 0.05 for visible wavelengths [59, 60, 61]. At wavelengths of 300 nm, measured values for k are at the upper end of this range [60]. Since these values have been obtained from diffuse reflectance experiments with dry aerosol particle samples, the absorption within a liquid droplet is better represented by values of k that have been calculated from Equation (1.18).

Via Mie's method, expressions for the scattering efficiencies can be obtained:

$$Q_{scat}(m,x) = \frac{2}{x^2}\sum_{k=1}^{\infty}(2k+1)\left[|a_k|^2 + |b_k|^2\right], \tag{1.19}$$

$$Q_{ext}(m,x) = \frac{2}{x^2}\sum_{k=1}^{\infty}(2k+1)\,Re\left[{a_k}^2 + {b_k}^2\right], \tag{1.20}$$

where

$$a_k = \frac{x\psi_k'(y)\psi_k(x) - y\psi_k'(x)\psi_k(y)}{x\psi_k'(y)\zeta_k(x) - y\zeta_k'(x)\psi_k(y)}, \tag{1.21}$$
$$b_k = \frac{y\psi_k'(y)\psi_k(x) - x\psi_k'(x)\psi_k(y)}{y\psi_k'(y)\zeta_k(x) - x\zeta_k'(x)\psi_k(y)},$$

solution	concentration ($\mathrm{mol\,L^{-1}}$)	α ($\mathrm{L\,mol^{-1}\,cm^{-1}}$)	absorption efficiency Q_{abs}
potassium ferrioxalate	0.05	5.5×10^{3}	2.7×10^{-2}
sodium nitrate	0.1	17	2.0×10^{-4}
sodium nitrate	2.0	17	4.1×10^{-3}

Table 1.3: Calculated absorption efficiencies for droplets 1 μm in diameter of typical solutions, for light of wavelength 305 nm.

with $y = xm$. The functions $\psi_k(x)$ and $\zeta_k(x)$ are the Riccati-Bessel functions and can be generated recursively via several different recipes [43, 44, 62].

Once the extinction and scattering efficiencies have been calculated, they can be used to calculate extinction, scattering and absorption coefficients (b_{abs}) for an aerosol of N particles per unit volume, since

$$Q_{abs} = Q_{ext} - Q_{scat},$$

and

$$b_{abs} = \frac{\pi d_p^2}{4} N Q_{abs}. \tag{1.22}$$

The absorption efficiencies calculated for some typical experimental aerosols are presented in Table 1.3 along with the corresponding molar (base e) absorption coefficients. Figure 1.5 plots the dependence of b_{abs} on particle diameter for a model aerosol. The spikes in absorption coefficient are from the Mie resonances while the overall shape of the plot is determined by the particle size distribution of the aerosol.

The radiant flux I in the aerosol[6] will be absorbed in accordance with the Beer-Lambert law:

$$dI = -I\, b_{abs} dx, \tag{1.23}$$

(c.f. Equation (1.15)) where x is the distance travelled through the aerosol [13].

For a chamber of length L

$$-\int_{I_0}^{I_L} \frac{dI}{I} = \int_0^L b_{abs}\, dx, \tag{1.24}$$

[6]Radiant flux is a more specific term than "light intensity". The radiant flux is the amount of radiation emitted, transferred or received in one direction. As mentioned in Section 1.1.2, the relevant measure of light intensity for atmospheric photochemistry is the actinic flux. This is the solar flux incident on a point inside the Earth's atmosphere, spherically integrated over all angles of incidence.

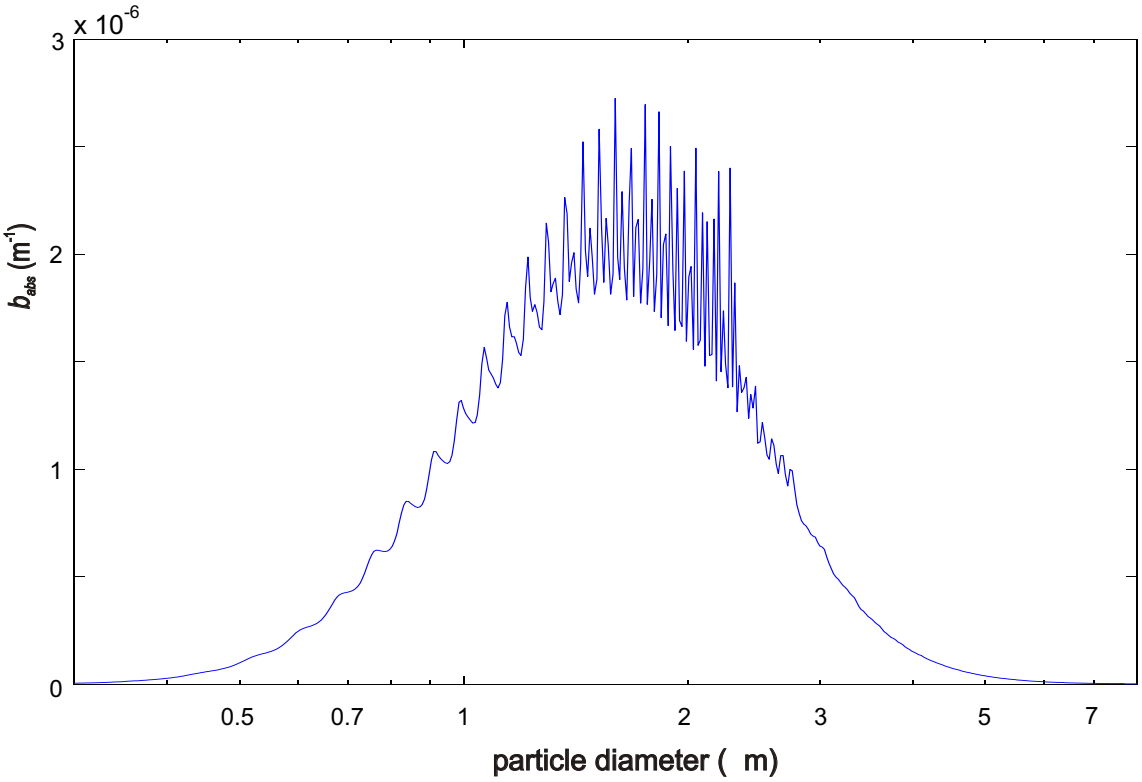

Figure 1.5: A plot of the number-weighted aerosol absorption coefficient, b_{abs}, as a function of particle diameter calculated for a model aerosol ($2\,\mathrm{mol\,L^{-1}}$ sodium nitrate). Note the logarithmic scale on the x-axis.

$$\begin{aligned} ln\frac{I_0}{I_L} &= b_{abs}L, \\ I_L &= I_0 e^{-b_{abs}L}, \\ &= I_0\left(1 - b_{abs}L\right), \end{aligned}$$

if b_{abs} is much less than 1[7]. In terms of the radiant flux absorbed:

$$I_{abs} = I_0 - I_L = I_0\, b_{abs} L. \tag{1.25}$$

Introducing irradiance, E, as the radiant flux per unit area, with units of quanta $\mathrm{s}^{-1}\,\mathrm{m}^{-2}$, and evaluating Equation (1.25) over the course of the experiment, the total yield (in terms of molecules) is

$$n_B = \Phi_B E_0\, b_{abs} L\, A\, t, \tag{1.26}$$

where Φ_B is the quantum yield, A is the cross sectional area of the chamber and t is the irradiation time. The irradiance, then, is given by

$$E_0 = \frac{n_B}{\Phi_B\, b_{abs} L\, A\, t}. \tag{1.27}$$

Note that b_{abs} includes both the particle concentration, N, and the absorbance of the liquid phase.

1.6 Diffusion and mass transport in droplets

1.6.1 Gas uptake

A high surface to volume ratio allows the rapid saturation of droplets by gases. At low concentrations, the vapour pressure of a dissolved solute at equilibrium is described by Henry's law:

$$c_B = H_B p_B, \tag{1.28}$$

where p_B is the vapour pressure of component B, c_B is the concentration in $\mathrm{mol\,L}^{-1}$ of B and H_B is the Henry's law constant. For example, the Henry's law constant for carbon dioxide in water at 298 K is $3.4 \times 10^{-2}\,\mathrm{mol\,L}^{-1}\,\mathrm{atm}^{-1}$, so at partial pressures of 5×10^{-4} atm of carbon dioxide (equivalent to 500 ppm) the concentration of carbon dioxide in the aqueous phase is $1.7 \times 10^{-5}\,\mathrm{mol\,L}^{-1}$ [13].

[7]While b_{abs} is much less than 1, $b_{scatter}$ is not, but since the majority of light is scattered forwards for micrometre sized particles [15], the attenuation of the light due to scattering can be omitted in the calculations here.

Gas uptake by droplets has been modelled in several different ways [13, 28, 63]. Typically the various steps are decoupled and the characteristic time for each step is investigated. Gas uptake involves several steps: diffusion to the droplet, adsorption on the surface, transport into the droplet, diffusion within the droplet, and possibly reaction within the droplet or at the interface.

1.6.2 Gas phase diffusion

In the continuum regime, with a Knudsen number[8] much less than one, the diffusion equation can be solved to obtain a characteristic time for diffusion to the droplet [13, 64, 65]. By parameterising the original differential equation so that all the dimensions are unitless, an estimate of the characteristic time for diffusion to the surface (τ_{dg}) can be obtained [13]:

$$\tau_{dg} = \frac{d_p^2}{4D_g}, \tag{1.29}$$

for a gas with a diffusion coefficient of D_g diffusing towards a droplet of diameter d_p. This equation also holds for outgassing from the droplet.

For carbon monoxide, with a diffusion constant in nitrogen of $0.15\,\mathrm{cm^2\,s^{-1}}$, and with droplets $1\,\mu$m in diameter, the characteristic time is $1.7 \times 10^{-8}\,\mathrm{s}$.

1.6.3 Transport across the interface and diffusion within the droplet

Similar treatments generate characteristic times for the transport of molecules across the interface and diffusion within the droplet. The case of transport across the interface is complicated since there are three processes happening at once: molecules leaving the surface (evaporation), molecules arriving at the surface (condensation) and molecules entering the bulk liquid phase (solvation). However, the diffusion equation can be solved analytically for this case too, and although the resulting series solutions are complicated, they converge rapidly and the characteristic timescale can be approximated by [13]:

$$\tau_p = \frac{d_p H_A \sqrt{2\pi M_A RT}}{3\alpha}, \tag{1.30}$$

for very soluble gases and

$$\tau_p = \frac{d_p^2}{\pi^2 D_{aq}}, \tag{1.31}$$

[8]The Knudsen number describes whether the particles should be treated in the continuum regime or on a molecular basis. See Section 2.2.2 for more detail.

for gases with low solubility, where M_A is the molar mass of gas A, R is the ideal gas constant, T is temperature, α is the mass accommodation coefficient (the probability that a molecule will stick to the surface of the droplet when it hits it) and D_{aq} is the diffusion coefficient for the gas in water. Gases of low solubility include carbon dioxide, carbon monoxide and the hydroxyl radical. In these cases, the Henry's law coefficient (H_A) is small and the characteristic time depends on the aqueous diffusion coefficient. Solving the diffusion equation for aqueous diffusion within the droplet results in the same solution (in this case the solution applies to both soluble and insoluble gases).

The diffusion coefficient for hydroxyl radical in water is $2.2 \times 10^{-5}\,\mathrm{cm^2\,s^{-1}}$ [16], which gives a characteristic time of $4.6 \times 10^{-5}\,\mathrm{s}$ for droplets $1\,\mu\mathrm{m}$ in diameter. This is a long time compared to the lifetime of OH in natural waters; calculations by Arakaki [20] give the lifetimes of OH in cloud droplets as 2.4 to $10.6 \times 10^{-6}\,\mathrm{s}$.

1.7 Comparison with previous experiments

1.7.1 Smog chambers and aerosol flow tubes

Experimental techniques for studying heterogeneous chemistry have historically tended to focus on gas uptakes at solid and liquid surfaces, investigations for which Knudsen cells and wetted-wall flow chambers are well suited. Investigations into the heterogeneous chemistry peculiar to aerosols, with their large surface area to volume ratio, typically use aerosol chambers (smog chambers) or aerosol flow tubes.

Smog chambers allow aerosol to be studied *in situ* at realistic pressures. They have been used for the majority of investigations into the kinetics of gas phase NO_x-O_3-VOC reactions [66]. The chambers vary in size from 1 to $200\,\mathrm{m^3}$, the inside surface being typically a Teflon bag.

Teflon is inert, inexpensive and transmits light of wavelengths greater than 300 nm. However, Teflon smog chambers have several major limitations. One limitation of smog chambers is the loss of aerosol particles to the chamber walls by diffusion and gravitational settling. Coagulation is another limitation: the number concentration and size distribution of the aerosol changes over time as particles combine. Also, Teflon can be statically charged, so the walls attract the charged aerosol particles. Electrostatic attraction is the major deposition route for particles smaller than $1\,\mu\mathrm{m}$ in diameter. For

particles larger than this, gravitational sedimentation becomes the major loss mechanism [67]. These wall losses can be minimised by having larger chambers, hence reducing the surface to volume ratio. Another limitation of Teflon is that it readily dissolves gases such as NO_2, so Teflon smog chambers are likely to exhibit 'memory' effects.

Due to Teflon's transparency to light of wavelengths longer than 300 nm, Teflon smog chambers are easily illuminated from all directions; it is also therefore more difficult to exclude light than for an opaque chamber. Smog chambers are typically irradiated either by natural sunlight or xenon arc lamps. Xenon arc lamps are a reasonable approximation of actinic light, which in any case is restricted to wavelengths above 290 nm by the ozone layer.

Smog chamber reactions have been followed with a wide spectrum of techniques. Examples are Aerosol Time Of Flight Mass Spectrometry (ATOFMS) [66], aerosol impaction followed by laser desorption ((MA)LDI MS) [68], gas chromatography (GC-MS) [69] and long path IR spectroscopy [70].

While the pressures and actinic fluxes used may be close to those of the natural atmosphere, smog chambers frequently have elevated concentrations of the trace gases of interest. For example, a study by Mentel *et al.* of night-time nitric oxide oxidation required NO_x concentrations on the order of 1 ppm. This is far higher (by a factor of 10 to 100) than their atmospheric concentrations, but such a high concentration was necessary in order to be able to detect the products (N_2O_5 and HNO_3) [71]. The relevance of such studies depends on whether the results can be extrapolated to the atmospheric situation, with considerably lower concentrations of reactants.

The basis of a flow tube study is the use of mixed flows of reacting gases. An aerosol generated via a jet nebuliser is already in a flow of gas; it is difficult to study aerosols in smog chambers since the pressure must increase as the aerosol is introduced (although this can be avoided by using a collapsible Teflon bag) [72]. A flow tube also allows collection of aerosol by impaction. Again, while this is possible in a smog chamber, the decrease in pressure must be compensated for. The aqueous aerosol can be collected as a solution and then analysed by High Performance Liquid Chromatography (HPLC) or UV-visible spectrometry [73]. Solid, impacted particles are often investigated with scanning electron microscopy (SEM) or laser desorption followed by time-of-flight mass spectrometry. More commonly, however, the gas phase products and the particulate

matter are analysed in a gas stream. Single particle time-of-flight mass spectrometry has been used to qualitatively determine the composition of secondary aerosol, for both organic and inorganic components [68]. The work reported in this thesis used a small stainless steel aerosol flow chamber in combination with a Residual Gas Analyser mass spectrometer to measure gas phase products. Liquid aerosol was also collected on an impactor and analysed with HPLC.

1.7.2 Investigations of nitrate photochemistry

Experiments investigating the photochemistry of aqueous nitrate aerosol have tended to use collected ambient atmospheric samples which are then irradiated as a bulk liquid in the presence of aqueous radical scavengers [20, 74]. While these studies are useful indicators of the relative importance of various components of the aerosol as OH sources (Fe^{3+}, NO_3^-, HONO, H_2O_2), they would not register any enhancements in yields resulting specifically from the optical and spacial properties of aerosols.

Anastasio and Newberg investigated the photochemistry of bulk liquid samples of sea salt aerosol [74]. They collected aerosol over several days at coastal sites and onboard ships along the California coast. The collected samples were transported back to a laboratory, where a radical scavenger (benzoic acid) was added and the bulk samples were irradiated with "simulated sunlight" from a xenon arc lamp. A chemical actinometer, 2-nitrobenzaldehyde, was used to measure the radiant flux in their system so the experimental yields could be converted to those expected under specific sunlight conditions. The results indicated that 59% of the hydroxyl radical produced was from nitrate photolysis. The total rate of OH production was reported as $3.4\times10^{-4}\,\mathrm{mol\,L^{-1}\,hr^{-1}}$, which is sufficiently fast to have a significant impact on the droplet chemistry, if not on the gas phase chemistry.

1.7.3 Radical scavengers

Because the hydroxyl radical is highly reactive, almost any organic chemical can be used as a scavenger as well as many inorganic ones like iodide and ferricyanide. Ideally, though, the scavenger will have a fast and well known rate of reaction with hydroxyl radical and will form products that do not interfere with the reaction and are easy to detect. The thiocyanate anion (SCN^-) is a popular radical scavenger. It requires real-

time detection with ultraviolet-visible spectroscopy [75]. Benzoic acid has been used in many studies of the photochemistry of aqueous nitrate. It reacts with hydroxyl radical to form stable, highly chromophoric products which are analysable by HPLC. In the gas phase, alkanes like cyclopentane and cyclohexane have been used as radical scavengers; they can be analysed with mass spectrometry.

Frequently, radical scavengers are also used to 'mop up' radicals. This prevents the radicals from reacting further with other products. This has allowed comparisons between radical initiated processes and other processes taking place simultaneously [76]. The presence of a radical scavenger can significantly affect the rates and mechanisms of any chemical reactions taking place, most notably in NO_x-O_3-VOC reactions.

Chapter 2

Experimental: Flow chamber and particle size distribution

2.1 History of the experimental set-up

The basic set-up used for this experiment had been designed by Chris Knox [42] and built in-house by the mechanical workshop. Many minor and several major modifications later, the experiments reported in this thesis used the same chamber with the same aims: generation and characterisation of an aerosol, irradiation of the aerosol, followed by collection of the liquid component of the aerosol and/or sampling of the gas phase.

Knox needed a light-proof reaction chamber. This was not only to eliminate ambient light interfering with the reactions, but to prevent light scattered by the aerosol being lost out of the sides of the chamber. The chamber and its components had to be inert to the liquid and gaseous chemicals used. In his case, this included alkenes (dec-1-ene) and acetylene. Stainless steel (304 grade) was chosen for its relative inertness and relative ease of working; 316 grade stainless steel is considerably more inert but also more difficult to machine.

The high-pressure xenon arc lamp (Osram-Sylvania XBO W 450 W lamp, with the housing and the power supply built in-house) was mounted directly above the chamber, which was supported above the bench by a metal frame. A manifold of valves and flow meters allowed specific mixtures of gases to be admitted into the chamber via an aerosol nebuliser. Gas was sampled via a 2 m long 1/16" stainless steel tube with Swagelok connections that led to the mass spectrometer inlet manifold. Otherwise, liquid samples were impacted and collected in a trap at the bottom of the chamber.

Knox designed the chamber to cause as little disturbance to the aerosol as was practical.

The nebuliser was connected to the chamber itself by a wide tube with a slow 90° bend. Provided that the radius of the bend was larger than the radius of the tube, the losses due to the bend were small [42]. The aerosol sampling ports were set at shallow angles to the gas stream before curving away to end up horizontal. Knox used Baron's *Aerosol Calculator* program to calculate the effect of any additions or modifications to the system [42, 77].

Possibly the most important development that Knox introduced was the stainless steel aerosol nebuliser. The construction of this nebuliser was an engineering feat in itself. Having found the available nebulisers unsatisfactory, producing droplet size distributions with mean particle diameters that were too large, Knox settled on a commercially available asthma inhaler that did produce an appropriate range of particle sizes. When the chamber was finally upgraded to stainless steel, the mechanical workshop reproduced the asthma inhaler in stainless steel.

2.1.1 Modifications to Knox's set-up

Over the course of the research presented here, it was necessary to adapt and improve the original set-up in several ways. Some of the more practical improvements included construction of a polythene tent around the bench (see Section 2.5.4) and the addition of a solution reservoir to the nebuliser (see Section 2.2.6). The light-proof tent enabled experiments to be conducted without the necessity of blacking out the entire lab. The reservoir allowed the chamber to be purged before the aerosol was added.

Several other improvements were responses to experimental problems. A bubbler was added to humidify the carrier gas because water was evaporating from the droplets during the passage of the aerosol through the chamber. Aluminium components of the chamber were replaced with Teflon and stainless steel when it became clear that the aluminium was reducing the potassium ferrioxalate.

In an attempt to improve the yield of the gas phase reactions in particular, the lamp, lamp housing and its power supply were replaced (Section 2.5.1). This involved making a new connection to direct the light into the chamber via a dielectric mirror, with provision for inserting various optical flats and neutral density filters when required (Section 2.5.2).

2.2 Aerosol flow chamber

An aerosol of nitrate solution was made to flow through the reaction chamber whilst being irradiated with UV light. The aerosol was produced by a jet nebuliser which was connected by a wide, curved tube to the top of the reaction chamber. The chamber was illuminated from above by a 1000 W mercury-xenon arc lamp. The chamber narrowed to a nozzle followed by an impactor. The chamber, nebuliser and impactor were all made from 304 grade stainless steel.

Above the nebuliser, a baffle removed the largest droplets from the aerosol. Having flowed through the baffle, the aerosol then entered the chamber via a connecting tube, where it was irradiated by the arc lamp. At a typical flow rate of $4.5\,\mathrm{L\,min^{-1}}$ the aerosol was in the chamber for around 40 s. It was then funnelled towards the (downstream) impactor. Ports into the chamber allowed sampling of aerosol by an Aerodynamic Particle Sizer (APS).

The chamber was pumped by a KNF diaphragm pump at such a rate as to keep the pressure of the chamber at around 10 Torr below atmospheric pressure. The entire chamber was mounted on a frame above a bench.

2.2.1 Chamber specifications

The chamber consisted of a vertical hollow cylinder of stainless steel, with a flat stainless steel plate at the top and an inverted stainless steel cone at the bottom (Figure 2.1). The cylinder had flanges to enable the top plate and the bottom cone to be bolted on. The flat plate had a circular window in the centre, over which a circular optical flat was fastened. At the bottom of the cone was a hole, which narrowed to the attachment for the impactor nozzle.

The cylinder was 400 mm in length and 95 mm in diameter. These dimensions, plus the internal volume of the cone, gave the chamber an internal volume of $0.00296\,\mathrm{m^3}$ (2.96 L). In comparison with other aerosol flow chambers, this is very small. A large smog chamber would be $260\,\mathrm{m^3}$ [78]. At typical flow rates of $4.5\,\mathrm{L\,min^{-1}}$, a parcel of aerosol took 40 seconds to flow through the chamber. Thus, each aerosol droplet was irradiated for 40 seconds.

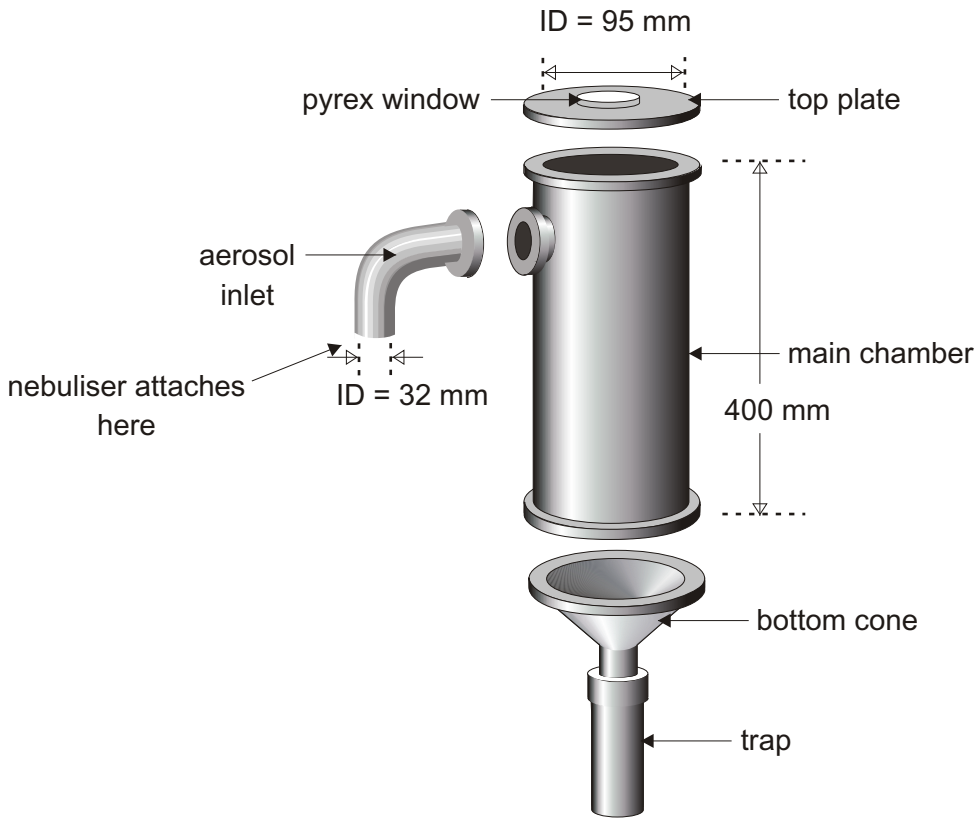

Figure 2.1: A pulled-apart view of the stainless steel chamber.

An advantage of having the chamber constructed of stainless steel was that electrostatic deposition of aerosol particles was minimised. Electrostatic charges are usually accumulated by aerosols as they are generated. A system built out of conductive material like stainless steel will have no electric fields within it so charged particles will not be attracted to the walls [79]. The small size of the chamber was also an advantage in terms of its ease of cleaning. The entire chamber could be unbolted from the frame that held it and transported to the sink for rinsing; it was light enough to be carried in one hand.

A small chamber is in general a disadvantage for aerosol studies. A larger chamber would mean that the aerosol was present in the chamber for longer than 40 seconds so higher yields of photolysis products would result. It could also potentially generate a larger volume of sample, although this could also have been achieved by having a larger solution reservoir attached to the nebuliser.

2.2.2 Aerosol behaviour during transport

In general, any sudden change in the aerosol flow path can affect the particle size distribution. Relevant examples include an abrupt constriction of the tube's diameter, or a bend in the tube. The size of the droplets will also be affected by the relative humidity. Water vapour will condense on the droplet if the relative humidity is high or will evaporate from the droplet if the relative humidity is low.

Knudsen number

The behaviour of aerosol particles in a gas stream depends on their diameter. Because aerosols range in size from tens of nanometres through to hundreds of micrometres, one physical description of their behaviour cannot be applied to all. For very small aerosol particles ($d_p < 0.1\,\mu$m), the particle is small enough that the gas flow can no longer be treated as a continuum, and the particle's motion is affected by collisions with individual gas molecules. The Knudsen number relates the molecular mean free path to the diameter of the particle [13, 79]:

$$Kn = \frac{2\lambda}{d_p}, \tag{2.1}$$

where λ is the molecular mean free path.

A Knudsen number much less than 1 indicates a continuum flow, while Knudsen numbers much greater than 1 indicate that the particle will behave like a (large) molecule. The treatment of the particles varies greatly for large ($d_p > 0.1\,\mu$m) and very small ($d_p < 0.1\,\mu$m) particles. In the present work, the majority of the aerosol droplets were large, that is, in the continuum flow regime.

Reynolds number

The Reynolds number describes the flow pattern of the gas, that is, whether it is turbulent or smooth (laminar). This is determined by the ratio of the inertial forces to the friction forces of the gas:

$$Re = \frac{\rho_g U d}{\eta}, \tag{2.2}$$

where U is the velocity of the gas, η is the dynamic gas viscosity, ρ_g is the density of the gas and d is a characteristic dimension of the object (such as the diameter of an

	Main section	Nebuliser outlet
Gas velocity ($\mathrm{m\,s^{-1}}$)	0.011	0.060
Tube diameter (m)	0.095	0.04
Reynolds number	67	159
Fraction lost	< 0.001	< 0.001

Table 2.1: Aerosol losses due to turbulence within the chamber for particles 0.7 μm in diameter, at 20° C and 1 atmosphere [77].

aerosol particle) [79]. The Reynolds number is specific to the geometry of the system in question. In a cylinder, for example, where the diameter is the characteristic dimension, turbulence occurs with Reynolds numbers above 4 000. The Reynolds number associated with a particle, however, indicates laminar flow if the value is less than 0.1. The Reynolds number calculated for the chamber was 67; the flow through the chamber was clearly laminar (see Table 2.1).

Stokes number, stopping distance and impactors

An impactor is a surface that perturbs the aerosol flow in such a way that the particles are deposited on the surface. Impaction is a common technique for measuring mass-weighted aerosol size distributions. For the experiments reported here, impactors were used to remove all or some of the aerosol particles from the gas stream.

A conventional impactor involves entrainment of the aerosol through a nozzle. At the end of the nozzle is an impactor plate which forces the jet of aerosol from the nozzle to change direction. The particles in this gas flow have inertia, and continue on towards the impactor for some distance. Lighter particles have lower inertia and tend to be swept along with the gas flow, while heavier particles will hit the impactor. The stopping distance (S) is a measure of the inertia of a particle. It depends on the size (d_p), density (ρ_p) and initial velocity U of the particle, and the viscosity (η) of the gas, where U is also the velocity of the gas through the nozzle:

$$S = \frac{U \rho_p d_p^2 C_c}{18\eta}. \tag{2.3}$$

Here C_c is the Cunningham slip correction factor, an empirical correction to account for a particle in the slip flow regime (that is, when the Knudsen number is around 1 and

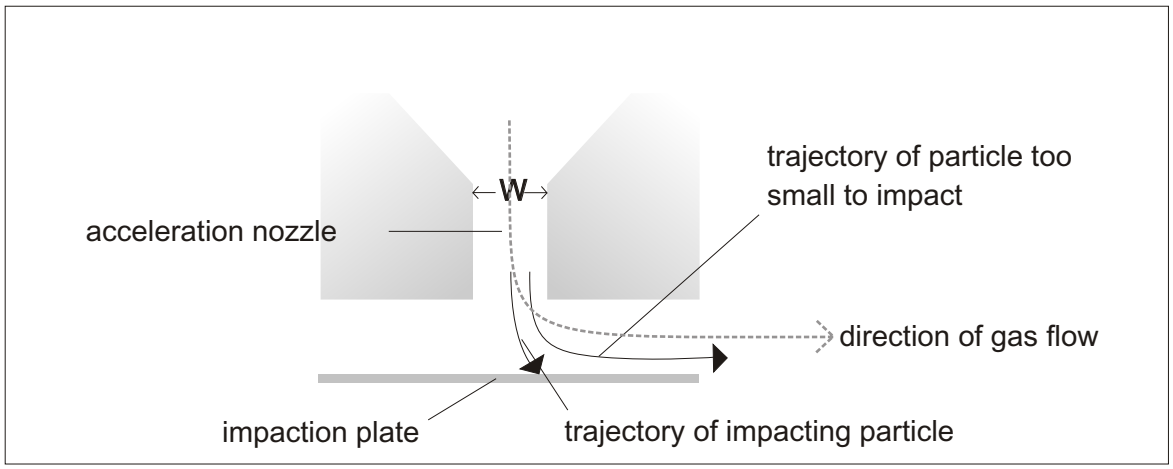

Figure 2.2: A conventional impactor.

the behaviour of the particle is beginning to deviate from the behaviour of a particle in a continuum regime). $C_c = 1.15$ for $1\,\mu$m particles [79].

The Stokes number (Stk) is a ratio of the stopping distance to the characteristic dimension of an obstruction, and is a measure of the likelihood of a particle being impacted by the obstruction. In the case of a conventional impactor, the characteristic dimension is the diameter of the nozzle, d_j, in which case

$$Stk = \frac{S}{d} = \frac{\rho_p d_p^2 U C_c}{18\eta d_j}. \tag{2.4}$$

In a conventional impactor, the diameter of the nozzle is critical to the penetration efficiency of the impactor, *i.e.* the percentage of particles of a particular size that remain in the gas stream after the impactor. The diameter dictates the tightness of the bend as well as the velocity of the jet. The distance between the end of the nozzle and the impactor plate is not so critical.

Nozzle velocity

The gas velocity in an impactor nozzle can be estimated if the pressures upstream and downstream of the nozzle are known, via the Bernoulli equation for compressible flow:

$$U = \left(\frac{2RT}{M} ln \left(\frac{P}{P - \Delta P} \right) \right)^{\frac{1}{2}}, \tag{2.5}$$

where M is the gas molecular weight, P is the upstream pressure and ΔP is the pressure difference [79].

Gravitational settling

From a consideration of the mass balance and momentum balance equations, it is possible to calculate the drag force on a particle. For aerosol particles of diameter less than 50 μm the drag force is given by:

$$F_{drag} = 3\pi\eta d_p U_\infty \tag{2.6}$$

where U_∞ is the velocity of the fluid, relative to the particle, measured at a large distance from the particle, and η is the viscosity of the fluid [13]. At particle sizes greater than 50 μm, inertial terms that were neglected in the derivation of Equation (2.6) begin to dominate and a drag coefficient must be included. The equation also breaks down for very small particles.

A particle being acted on by the force of gravity will accelerate until the gravitational force is balanced with the drag force. Its terminal velocity (settling velocity) is found to be:

$$v_t = \frac{1}{18}\frac{d_p^2 \rho_p g C_c}{\eta}. \tag{2.7}$$

This equation is valid for particles less than 50 μm in diameter. Fine particles, that is $PM_{2.5}$, have low settling velocities and are likely to remain suspended in the atmosphere for days or weeks.

Table 2.1 is included to illustrate that under the conditions of the experiment, the aerosol losses due to turbulence were minimal, both in the chamber and in the tube from the nebuliser to the chamber. These calculations do not take into account the turbulence that was likely to have been present at the connection between the tube and the chamber. Because there was an abrupt change in diameter where the tube met the chamber, eddies would have formed at this point [79]. It is very hard to calculate the losses for this type of disturbance to the flow. Overall, though, the chamber dimensions are large enough that aerosol losses due to transport are not a major concern.

2.2.3 The aerosol nebuliser

A variety of methods are available for generating aerosols. Commonly used ones are particle nucleation, jet nebulisation and sonic oscillator generation. The method chosen will depend on the required aerosol characteristics: specifically, concentration and size distribution. An aerosol in which all of the particles have the same diameter is described as 'monodisperse'. Aerosols with a distribution of particle sizes are 'polydisperse'. All natural aerosols and many laboratory generated aerosols are polydisperse aerosols.

A jet nebuliser, also known as a Collison nebuliser[1], generates an aerosol based on the Bernoulli principle (see Figure 2.3). A fast moving fluid is at a lower pressure than a stationary one, and the static fluid will start to flow towards and into the moving fluid. In this way, gas moving through the nebuliser pulls liquid up through a capillary. As the liquid enters the jet stream it is nebulised into droplets. The nebuliser used in the present system was a stainless steel version of a Medic-Aid Sidestream nebuliser. This nebuliser generated a polydisperse aerosol of high droplet concentration.

Vibrating Orifice Aerosol Generator (VOAG)

The Vibrating Orifice Aerosol Generator (TSI, model 3450) is an example of a sonic oscillator: a jet of solution is forced through an orifice connected to a vibrating piezo-electric crystal, in such a way that one droplet is released per cycle of vibration. The initial droplet diameter depends on the diameter of the orifice. An orifice 10 mL in diameter produces droplets 25 μm in diameter. If the frequency of the crystal is tuned to match the rate at which liquid is supplied to the orifice, a steady stream of droplets ensues. The solution consists of a volatile phase (often isopropanol) and a non-volatile phase, either a liquid like oleic acid or a solid like sodium nitrate. The resulting aerosol is monodisperse and of low concentration, compared to a jet nebuliser.

The concentrations of the aerosols produced are typically around 3.0 particles cm^{-3}. The final size of the aerosol particles is dictated by the diameter of the orifice and the ratio of the volatile phase to the non-volatile phase. The initial droplets formed in the jet are

[1]Nebulisers are also often called atomisers. An example is the TSI 3076 atomiser which operates by the same principle as the jet nebuliser described here and generates a similar particle size distribution. This thesis follows the lead of Knox, who used the word 'nebuliser' to describe any aerosol generating device to avoid confusion with Atomic Absorption Spectroscopy and similar techniques which involve the generation of free atoms.

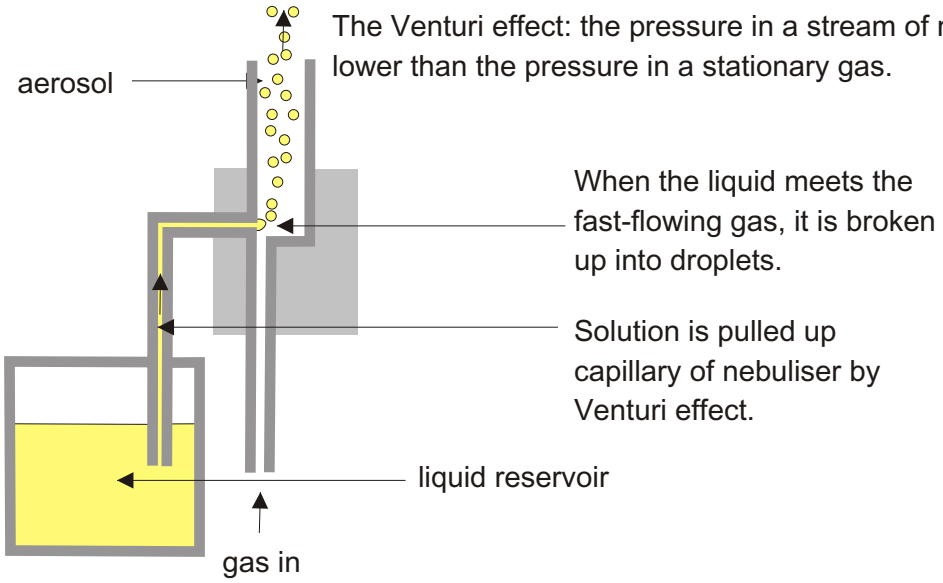

Figure 2.3: A schematic of a basic Collison nebuliser.

all the same diameter (d_d), so once the volatile phase has evaporated, the diameter of the resultant particle (d_p) will depend on the amount of non-volatile compound in the solution:

$$d_p = C^{\frac{1}{3}} d_d, \tag{2.8}$$

where C is the volumetric concentration of non-volatile compound. The initial droplet diameter was 25 μm (from a 10 μm orifice). Thus, a solution with a oleic acid:isopropyl alcohol ratio of 1:500 generated droplets with a final diameter of 1.9 μm. In the present work the VOAG was used to test the Aerodynamic Particle Sizer and its dilution system.

2.2.4 Downstream impactor

The downstream impactor fulfilled two roles: it protected the pump and the downstream flow meter from the aerosol and it collected the aerosol particles for later analysis.

Figure 2.4 shows the different versions of the downstream impactor used throughout the experiments. Version (a) was inherited from Knox as part of his original chamber. A desire to modify the size distribution of the particles collected led to an impactor with a wider nozzle (3 mm as opposed to 2.5 mm) being made, with an adjustable impaction plate: version (b). To ensure that every particle was collected, an insert for version (b)

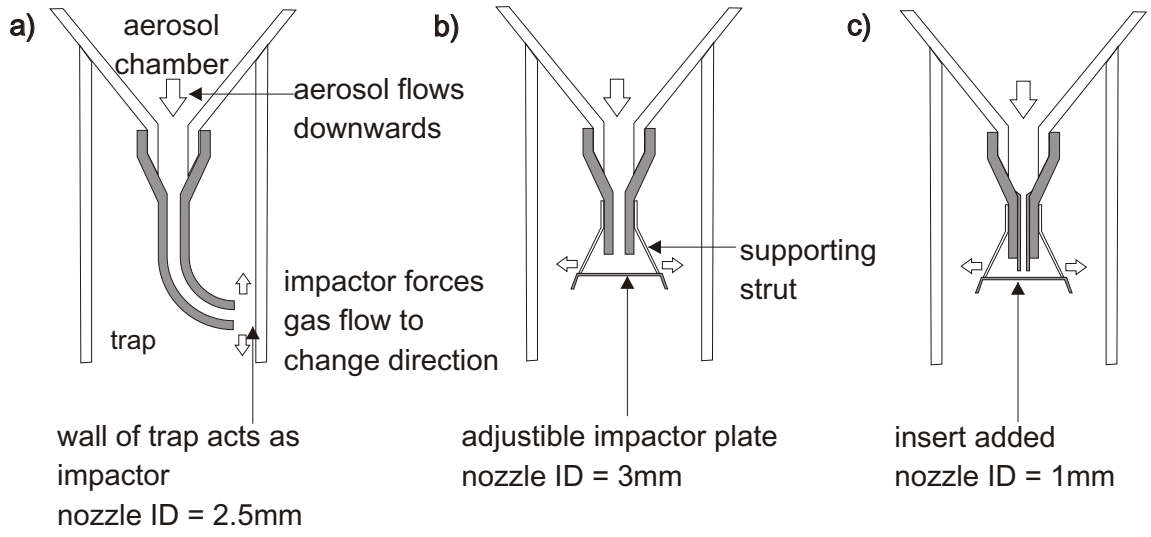

Figure 2.4: The three versions of the impactor used.

turned it into version (c), with a 1 mm nozzle. The insert could be removed when it was necessary to revert to version (b).

Calculations to determine which sizes of particle would be collected by the impactor were performed with the help of Baron's Excel spreadsheet [77]. The nozzle diameter and the gas velocity through the nozzle are the key parameters. Gas velocities were calculated for each nozzle from the known flow rates via Equation (2.5). For a 1 mm nozzle, the gas velocity would be 95.5 m s^{-1} while for a 3 mm nozzle the gas velocity would be 10.6 m s^{-1}. The square root of the Stokes number (Stk, the ratio of the stopping distance to the nozzle diameter, see Section 2.2.2) corresponds to a dimensionless particle size. $\sqrt{Stk_{50}}$ is the value of $\sqrt{Stk}$ corresponding to d_{50}, the diameter at which 50% of the particles are impacted [79]. For a conventional impactor, $\sqrt{Stk_{50}} = 0.47$. From this value, the d_{50} was calculated to be 0.54 μm for a 1 mm nozzle and 3.1 μm for a 3 mm nozzle (Table 2.2).

The 1 mm ID nozzle resulted in a pressure difference of around 40 Torr between the chamber and downstream of the nozzle. The Reynolds number for the 1 mm nozzle is 6 400. While the range of recommended Reynolds numbers is between 500 and 3 000, it is only at low Reynolds numbers that the impactor efficiency drops markedly. However,

Nozzle diameter (mm)	1	3	4	5
Gas velocity ($m\,s^{-1}$)	95.5	10.6	6.0	3.8
Stokes number	0.22	0.22	0.22	0.22
d_{50} (μm)	0.54	3.1	4.8	6.7
Pressure difference (Torr)	40.2	0.51	0.16	0.07
Reynolds number	6 400	2 100	1 600	1 300

Table 2.2: Various parameters calculated for the relevant nozzle diameters [77].

re-entrainment of particles may occur at high Reynolds numbers, that is, in turbulent conditions [79].

Measurements of the particle size distribution with the APS were carried out with the APS inlet sampling from the trap downstream of the impactor, in order to measure impaction efficiencies experimentally. The 3 mm nozzle let sufficient aerosol through to overload the APS, so quantitative measurements were possible only for the 1 mm nozzle. These measurements could not be run under identical conditions to those of a typical experiment. The pressure difference between the chamber and the trap was around 40 Torr. Since the APS is set up to sample at atmospheric pressure (around 760 Torr) the sampling flow rate varies significantly if the pressure is much different from the atmospheric pressure. For sampling from the chamber, this was not a problem since the chamber pressure was maintained at just under atmospheric pressure, but for sampling downstream from the impactor, the pressures were necessarily much lower than in the chamber. Unless the chamber pressure was maintained at 800 Torr, so that the trap was at 760 Torr, the APS struggled to maintain a flow rate of $4\,L\,min^{-1}$ for the sheath flow. A pressure of 800 Torr in the chamber may have affected the size distribution and particle concentration of the aerosol. In spite of these limitations, it was clear that the ID = 1 mm impactor collected 98 to 99% of the aerosol droplets.

2.2.5 Upstream impactor

Due to the possibility of large droplets distorting the particle size distribution (see Section 2.9.5), a glass impactor was included after the nebuliser, upstream of the chamber, to remove any droplets larger than 5 μm. This upstream impactor consisted of a smooth constriction of glass narrowing to an internal diameter of 4 mm followed by a 90 ° bend

to direct the aerosol against the wall of the chamber (Figure 2.5).

Because it was thought that the 4 mm nozzle upstream impactor might be removing too high a percentage of the droplets, an alternative upstream impactor with a 5 mm internal diameter was built to be used for dilute solutions. The impactors were attached to the top of the baffle section of the nebuliser with Selley RTV silicone sealant. This gave a relatively tight seal but allowed easy removal so that the glass impactors could be switched. The calculated pressure difference over a 4 mm ID upstream impactor is much less than 1 Torr (Table 2.2).

2.2.6 Solution reservoir

A glass reservoir with a volume of 10 mL was attached to the nebuliser via two ports, one to admit the solution and the other to equalise the pressure (Figure 2.6). A tap on the bottom of the reservoir admitted the solution into the nebuliser. A Teflon tube attached the top of the reservoir to the second port. This port also proved useful as the inlet for the scavenger gases, allowing them to mix well with the aerosol upstream of the chamber.

2.3 Flow meters

The original flow meters were three Airco H-10K, B-200-10000 mass flow meters. By measuring the transfer of heat from a wire to the flow of the gas, the rate of flow can be determined. The resistance of the wire depends on its temperature. The faster the flow of gas, the more heat is conducted away from the wire. Typically, two temperature sensing wires are wound symmetrically around a sensor tube. The difference in temperature between the upstream and downstream thermometer indicates the heat transfer to the gas, which depends on the rate of flow of the gas and the heat capacity of the gas.

Because the heat capacity will be different for different gases, or mixtures of gases, a conversion factor must be used if the gas is not nitrogen. Since the flow meters are calibrated at temperatures of 0 °C, a temperature correction must also be applied to the conversion factor if the flow meters are to be used at a higher temperature.

The Airco flow meters, when operational, gave consistent flow measurements. Their main limitation is the display; the resolution was 100 sccm. Their range was nominally 0

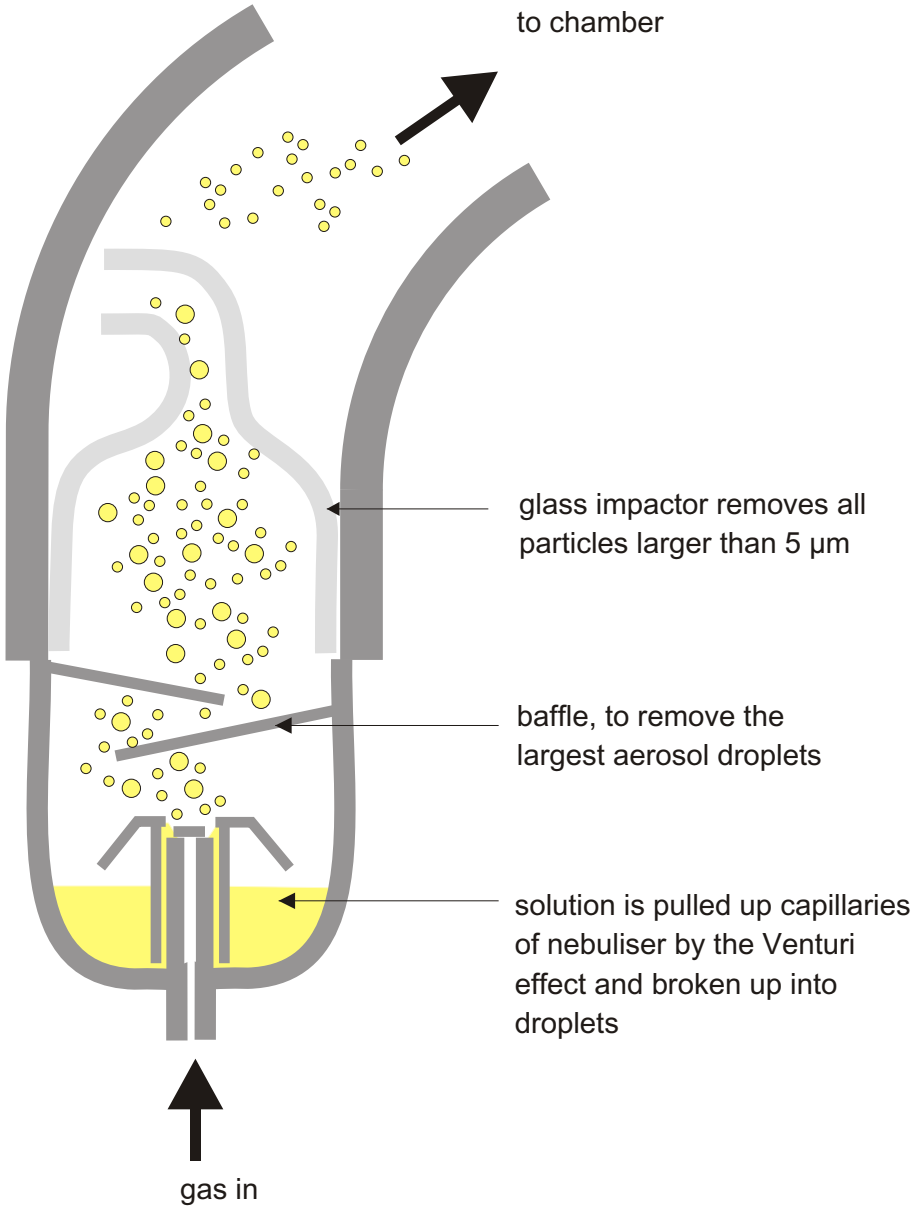

Figure 2.5: The nebuliser and glass impactor, upstream of the chamber.

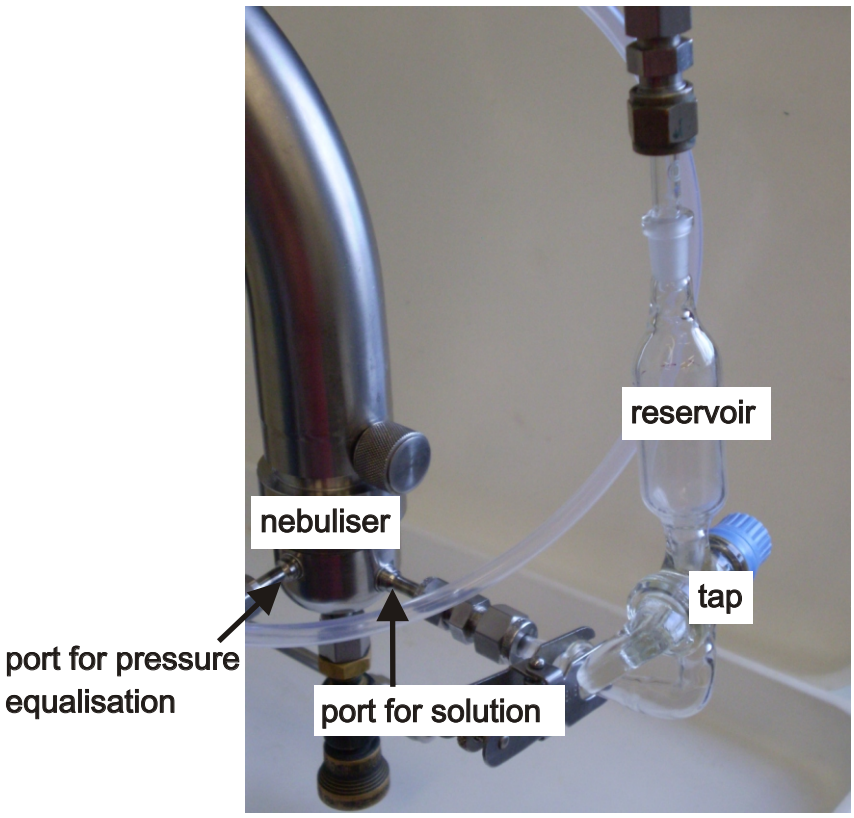

Figure 2.6: The reservoir, attached to the nebuliser.

to 5 000 sccm, although one had apparently been adjusted to measure up to 10 000 sccm. The flow meters were calibrated by bubble meter[2] and then by the new MKS flow meters. 'sccm' stands for standard cubic centimetres per minute, that is, cubic centimetres per minute of nitrogen flow at 273.15 K and 760 Torr.

Tylan mass flow meters (FM-360) were also used, for smaller flow rates: 10 sccm and 100 sccm. They operate on the same principle as the Airco flow meters. These too were calibrated by bubble meter.

2.3.1 MKS flow meters

Two MKS flow meters (M10MB Mass-Flo Meter) and two flow controllers (M100B Mass-Flo Controller) were bought at the end of 2004, and by August 2006 up to eight new MKS flow meters were in use, replacing the older Airco flow meters. The flow into the nebuliser determines the concentration and to a more limited degree the size distribution of the aerosol, so it is a distinct advantage to have the flow into the nebuliser controlled automatically. Like the Airco flow meters, the MKS meters are mass flow meters, measuring the transfer of heat from a wire to the flowing gas.

The MKS mass flow meters are made of 316 grade stainless steel, along with nickel and "Elgelloy". The seals are Viton. The flow sensor is a wire wrapped symmetrically around a sensor tube which samples a small portion of the gas flow. The rest of the gas flows through a "packed disk" bypass assembly, with laminar flow maintained at all stages. The transfer of heat to the gas depends on the specific heat, C_p, of the gas [80].

The flow meters used have maximum flow rates of 100, 1 000, 10 000 and 20 000 sccm. The meters have a 1% accuracy with respect to the maximum range of the individual instrument and are insensitive to changes in temperature between 0 and 50 °C.

Four of these eight flow meters were mass flow controllers. A solid state valve maintained the gas flow through the controllers at a constant rate. The controllers were connected to one of two MKS Type 247D Four-Channel Readout units. These displayed the flow rate through the selected meter. They also controlled the gas flow through up to four

[2] A bubble meter consists of a graduated cylinder (*i.e.* from a burette) with a reservoir of detergent solution at its base and with nitrogen flowing up the cylinder. Bubbles of detergent can be introduced into cylinder and travel up it at the same rate as the gas. The flow rate of the gas can be calculated by measuring the time taken for the bubble to sweep through a particular volume.

controllers. The flows were set manually via a potentiometer. The default flow was zero flow. A second potentiometer for each channel was used to adjust the readout via the appropriate gas correction factor.

2.4 Aerodynamic Particle Sizer

The particle size distribution of the nitrate aerosols was measured by a model 3320 TSI Aerodynamic Particle Sizer (APS). The APS can reliably measure the size distribution of an aerosol at low to moderate concentrations of particles. However, above concentrations of about 3 000 particles per cubic centimetre, the APS suffers from coincidence errors. It is still possible to get a particle size distribution, but the apparent particle concentration measured is much lower than the actual one. Hence the gas stream going to the APS had to be diluted to a known extent before it entered the APS, in such a way as to disturb the aerosol as little as possible. Also, the chamber pressure had to be constant for the APS to work accurately. While the aerosol sampling flow was supposed to be $5\,\mathrm{L\,min^{-1}}$, maintained by an internal pump of the APS, this was not the case if the pressure varied.

2.4.1 Principles of operation

The APS samples aerosol at $5\,\mathrm{L\,min^{-1}}$ which it divides into an aerosol sample flow and a sheath flow [81]. The sheath flow is maintained at $4\,\mathrm{L\,min^{-1}}$. It is filtered and then recombined with the aerosol flow at the 'accelerating orifice nozzle'. The aerosol flow is confined to the centre of the air stream and accelerated by the filtered sheath flow. The acceleration of the particles due to this sheath flow will depend on their size, with larger particles experiencing less viscous drag relative to their mass and hence being accelerated to a lesser extent (described by Equation (2.6)).

In the optics chamber, each particle passes through two laser beams. The beams are generated by a 28 mW, 675 nm laser diode. As the particle passes through each beam, the light is scattered. Scattered light is collected by an elliptical mirror and focussed onto a solid state avalanche photodiode detector. This detector converts the light pulses into electrical pulses.

Each particle will generate two pulses, one from each beam. The time between these

pulses gives us the velocity of the particle, since the distance between the beams is known. Since the smaller particles are moving faster, the velocity correlates inversely with size. The two pulses together make up a 'double crested signal'. This signal is analysed by a gate circuit and a differential circuit, to give one of four possible events, depending on the height of each crest and the time between them:

Event 1: Only one of the crests is high enough to be detected.

Event 2: Both of the crests are high enough, and the particle is sized.

Event 3: Two or more particles coincide, giving more than two crests to the signal.

Event 4: The particle is travelling very slowly, and the distance between the peaks is over range.

Particle coincidence gives a multi-crested signal (Event 3). The processor does not attempt to size these signals and they are not included in the size distribution. They are still counted, however, and used to correct the total concentration.

Each particle resulting in 'Event 2' is classified according to time-of-flight into one of 1 023 bins. The raw data in these time-of-flight bins is then converted into a particle size distribution via a factory generated calibration curve.

The APS can be controlled remotely via an RS 232 connection to a Pentium PC. The software permits various sampling schedules. For all the data reported here, the samples were taken for 20 s at intervals of 120 s.

2.4.2 Aerosol Instrument Manager

The software supplied with the APS by TSI is in the form of a program called Aerosol Instrument Manager. As well as controlling the APS and collecting data from it, this program can display the data in a variety of forms and calculate statistics such as the geometric mean and geometric standard deviation. The equations used to calculate these latter two parameters can be found in Section 2.8.

The program relies on a number of assumptions to calculate the particle size distributions. It assumes that the particles are spherical and via a user-provided density

of the solution (the default is $1.00\,\mathrm{g\,cm^{-3}}$) calculates the mass-weighted particle size distributions. The APS software also assumes that the flow rate into the particle sizer is $5\,\mathrm{L\,min^{-1}}$. In fact the flow rate depended on the pressure at the inlet of the APS.

The particle size distributions are presented as frequency histograms (see Figure 2.11 on page 60 for an example). The range of particle sizes is from 0.5 to 20 μm in diameter. Additionally, particles between 0.3 and 0.5 μm are displayed in a separate bar. The concentration of particles between 0.3 and 0.5 μm never corresponded well to the data for particles above 0.5 μm in diameter. This data was measured by a different method to the rest of the data, from light scattering patterns as opposed to time-of-flight measurements, and was not used in any subsequent analysis.

2.4.3 Dilution of flow

An aerosol diluter was built in order to dilute the aerosol particle concentration to a level measurable by the APS. The diluter (Figure 2.7) consisted of an inner metal tube and an outer glass tube. The undiluted aerosol entered from the chamber via the metal tube. A controlled amount of dilution gas (N_2) entered the glass tube. The extent of dilution was controlled by the ratio of the internal cross sectional areas of the two tubes. Thus

$$\frac{F_{dilution}}{F_{sample}} = \frac{r_{dilution}^2 - r_{sample}^2}{r_{sample}^2}, \tag{2.9}$$

where $\frac{F_{dilution}}{F_{sample}}$ is the extent of dilution and $r_{dilution}$ and r_{sample} are the radii of the respective tubes. The walls of the metal tube were thinned near the end so that the internal diameter equalled the outer diameter.

The pumping speed of the APS, and hence total aerosol sampling flow rate, depended heavily on the pressure at the APS inlet, which depended in turn on the pressure in the chamber, as measured by the Baratron pressure transducer. Ideally, the diluter would be used with a dilution flow such that the velocity of the gases at the end of the inner metal tube were equal, thus minimising turbulence. For gas with velocity v,

$$v = \frac{Flow}{Area},$$

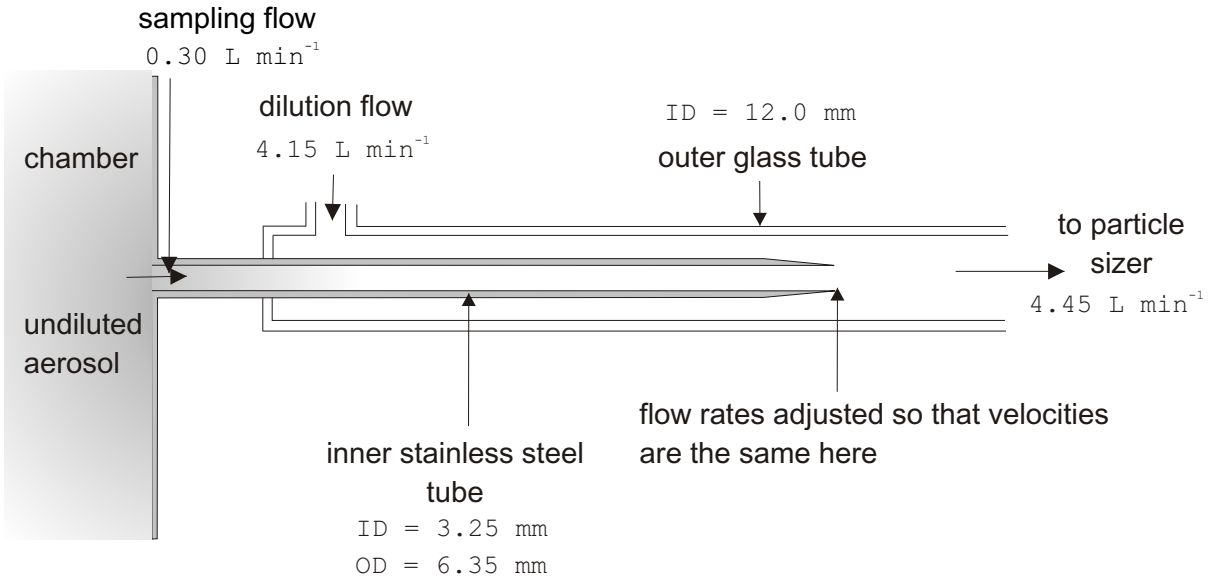

Figure 2.7: The aerosol diluter.

and if the velocities of the sampling gas and the dilution gas are equal,

$$\begin{aligned} \frac{F_{sample}}{r^2_{sample}} &= \frac{F_{total}}{r^2_{total}}, \\ F_{sample} &= \frac{F_{total} r^2_{sample}}{r^2_{total}}. \end{aligned} \tag{2.10}$$

The dimensions used for the diluter were dictated by the dimensions of the chamber and the APS, namely the 3.25 mm inner diameter of the sample port and the 12.0 mm inner diameter of the APS inlet tube. With these dimensions and if the APS is sampling at 4.45 L min^{-1}, to have the velocities of the sampling and dilution flows equal at the end of the inner metal tube the sampling flow must be 0.30 L min^{-1} and the dilution flow must be 4.15 L min^{-1}. However, due to the high concentrations of particles in the aerosol, it was often necessary to dilute the sample to a greater extent, as discussed in Section 2.9.6. The sampling tube itself is 225 mm long. Two curved sections of stainless steel tube connect the sampling tube to the chamber. The first has a curve of around 25 mm in radius and extends horizontally from the chamber for 55 mm before joining the second section which has a simple 90° curve and a radius of 25 mm. The horizontal distance the gas must travel through the entire sampling system is therefore 300 mm.

2.4.4 Tests of the APS with the VOAG

The Vibrating Orifice Aerosol Generator was used to test the APS and the dilution system. The top plate of the chamber was removed and the VOAG liquid orifice assembly was placed above the chamber, with the jet directed downwards. Aerosols of oleic acid and sodium chloride were generated. The measured particle size distributions matched the theoretical distributions, that is, the aerosol was monodisperse and the diameter of the particles corresponded to the diameter as calculated via Equation (2.8).

2.5 Optics

2.5.1 Lamp

A second hand lamp and associated lamp housing (Oriel # 66021) and power supply (Oriel Universal Power Supply, # 68820) had been bought in mid 2005 to replace the original 450 W lamp. The power supply delivered power from 300 W to 1200 W. A 1000 W mercury-xenon arc lamp bulb (Hanovia, #977B0010) was sourced within the department and replaced the second hand lamp bulb that came with the housing.

The mercury-xenon lamp was superior to the original, since it emitted more intense light at specific useful wavelengths (that is, 313 nm. See Figure 2.8). It was also more powerful in general. However, while it was found to work well at power consumptions of around 800 W, at 900 W it would overheat and cut out. At 815 W it drew 28 A at 30 V. During the course of an experimental run, the lamp warmed up and the power consumption dropped somewhat. It was assumed that the radiant flux of the lamp dropped proportionally. Correcting the measured yields for this drop made only a slight difference to the final values.

2.5.2 Optical path

The Oriel lamp housing dictated that the lamp bulb was mounted vertically, so that the light was emitted horizontally, via an adjustable focus (Figure 2.9). The original lamp had been oriented such that the bulb was horizontal and directly above the chamber. The new lamp was positioned off to one side, with a mirror at 45 ° to direct the light down into the chamber. The mirror was a dielectric mirror, 50.8 cm in diameter with

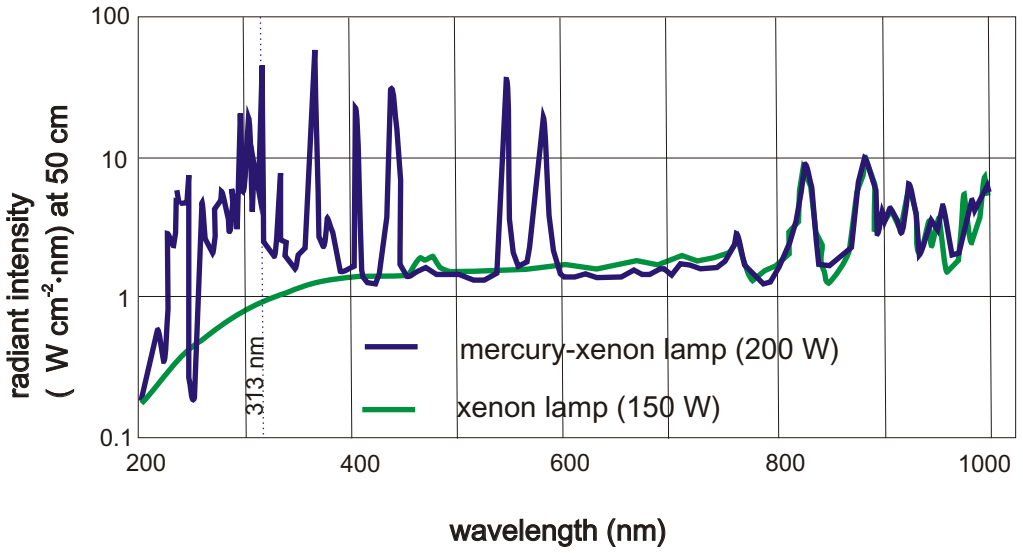

Figure 2.8: A comparison of spectra of mercury-xenon lamps and xenon arc lamps.

maximum reflectivity between 281 and 308 nm, #024-0360 from Optosigma. The lamp was focussed so that the maximum amount of light was reflected off the mirror. This resulted in a slightly converging beam. The light entered the chamber via a window, an optical flat made from either quartz glass or Pyrex glass. The quartz optical flat was transparent to all wavelengths between 200 and 800 nm while the transmittance of the Pyrex glass decreased sharply below 300 nm (Figure 2.10).

The UV light was contained in an L-shaped aluminium tube, with the dielectric mirror at the bend of the L. The tube was made from separate sections of aluminium inserted firmly together (push-fit). The mirror was mounted on an aluminium heat sink. A spring held it to the end of a worm screw that could be turned to adjust the angle of the mirror. A space for further optical flats was included between the dielectric mirror and the window of the chamber. This was used to house neutral density filters and a dielectric filter. The bottom section of the tube was two pieces that screwed together. At the beginning of 2007, a shutter was added in the bottom section of the tube, just above the optical flat holder. The shutter enabled the lamp to warm up while the bulk liquid solution was in the chamber and enabled on/off control of the light during the gas phase scavenger experiments.

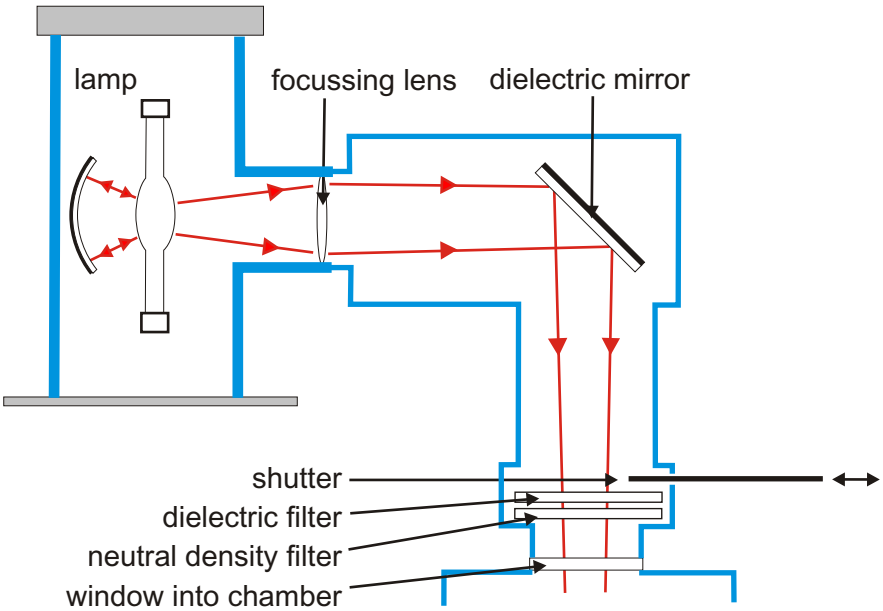

Figure 2.9: The lamp and optics.

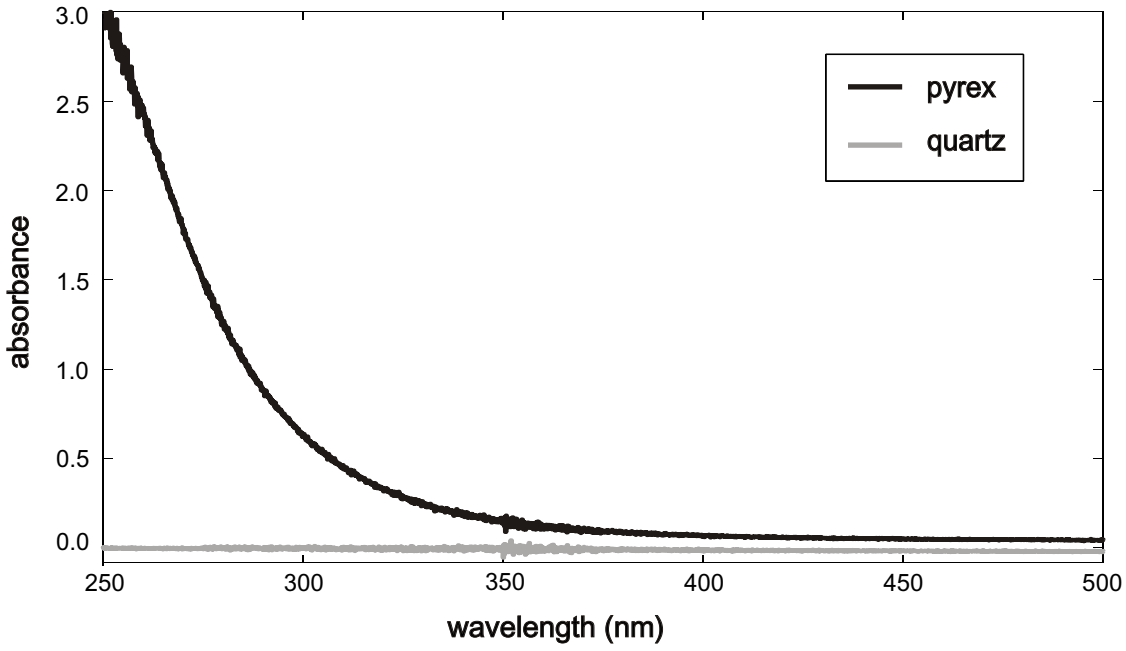

Figure 2.10: Absorption spectra for the quartz and pyrex optical flats.

2.5.3 Filters

The narrow band filter (Andover, #313FS25-25) limited the wavelengths of light emitted by the lamp to between 295 nm and 330 nm. At 23°C it had a maximum transmission of 23% at 310.4 nm. The bandwidth, at 50% of the maximum intensity, was 27.6 nm. The neutral density filter (Newport, #QD-20-S) was made of a metallic layer fused on silica. It had an absorbance of 2.0 at 300 nm.

2.5.4 Light exclusion

Potassium ferrioxalate is extremely sensitive to light, hence its usefulness as an actinometer. However, this meant that all extra light, including laboratory lighting and natural light, had to be excluded from the experiment for every process involving potassium ferrioxalate.

To this end, the bench, the frame above the bench and some surrounding floor space were covered in a black polythene tent. The polythene was opaque to visible and ultraviolet light. The only source of light inside the tent was an incandescent bulb behind a yellow filter (Kodak Wratten Series, OB). This emitted a dim yellow light which did not affect the ferrioxalate to a measurable extent. Black duct tape also proved to be opaque, and was used to cover any gaps in the polythene. The pressure transducer and the flow meter controllers emit a dim red light from their displays, and the Vaisala humidity meter has a green diode (LED) to signify when it is on. None of these sources of light proved significant.

The preparation of ferrioxalate crystals, the preparation of ferrioxalate solution, admission of the solution into the reservoir, collection of the resultant sample and analysis of the sample were all carried out under these 'black out' conditions. The reservoir had to be covered in a black, light proof cloth during the experiment, because some light would escape from the lamp housing. Preparation of the iron-phenanthroline solutions for the analysis was performed in the dark, as was the absorbance measurement with the UV-visible spectrometer. This necessitated that the computer screen was turned off, which complicated the operation of the program running the spectrometer. The tent was just large enough to accommodate the entire spectrometer and trolley, with some space for the operator.

Similar precautions were carried out for sodium nitrate, although they were less strictly adhered to. Nitrate solutions are not nearly as light-sensitive as potassium ferrioxalate.

Black polythene would not be the first choice of material for such a tent, because it is shiny and reflects some light. It is also hard to attach to itself with tape. A better choice would have been thick black cloth such as was used around the reservoir. However, polythene was available at the time the tent was constructed and proved sufficient.

2.6 Other instruments

2.6.1 Vaisala humidity meter

The Vaisala relative humidity (RH) meter consists of a probe and a transmitter. The model used (HMT331) is one of the more basic instruments available in the Vaisala range. The probe has a sintered stainless steel filter to protect the sensor, which consists of two plates forming a capacitor. The capacitance between these two plates depends on the absolute humidity. The probe also includes a temperature sensor, necessary for calculating the relative humidity.

The temperature sensor can measure temperatures from -40 to 60 °C, with an accuracy of ± 0.2 °C at 20 °C. The relative humidity meter has an accuracy of 1% at relative humidities of between 0 and 90% and at temperatures of 15 to 25 °C.

2.6.2 Baratron manometer

Pressure inside the chamber was measured with an MKS Baratron pressure transducer, model 722A, which can measure pressures from 0 to 1 000 Torr. This proved sufficiently consistent and responsive, although the actual readings can probably only be used as a relative measure. This transducer was at one stage exposed to a much higher pressure than it is able to read. After this the readings were consistently too high, by about 40 Torr, so it was replaced by a similar transducer, MKS model 627A.

2.6.3 Carbon monoxide detector

During experiments involving carbon monoxide, a carbon monoxide analyser was used to check that no leaks of carbon monoxide had occurred. The instrument was a Kane-

May SGA70. Its range is 0 to 1 999 ppm, with an accuracy of 10%. The sensor is an electrochemical cell, which had a response time of 30 to 40 s.

2.7 Materials

Where possible, the chemicals used were of analytical grade. Potassium ferrioxalate was prepared from reagent grade potassium oxalate and ferric chloride. The gases used were the standard purities from their respective suppliers, with the exception of carbon monoxide. This was Ultra High Purity grade and further purified with a potassium hydroxide gas scrubber. The materials used for this project are listed in Table 2.3.

Milli-Q water from a Millipore Gradient system was used for all analyses. Water from this system had a Total Organic Carbon concentration less than 5 ppb.

2.8 Statistical descriptions of particle size distributions

The surface area to volume ratio, light intensity enhancement and physical behaviour of the aerosol are all dependent on the droplet diameter. The amount of liquid solution suspended in the chamber as droplets and the total surface area of the liquid phase depend on the particle concentration. These properties need to be measured as accurately as possible.

The particle size distribution was measured with the Aerodynamic Particle Sizer (APS) for particles of diameters ranging from 0.5 μm to 20 μm. The particle size distributions for the experimental aerosols proved to be at the lower end of this range. This meant that all distributions were truncated to some extent, necessitating the fitting of model log-normal distributions to estimate the parameters of the experimental size distribution.

2.8.1 Displaying particle size distributions with frequency histograms

A frequency histogram consists of a bar plot of frequencies of detection of particles (particle counts), classified according to diameter. A number-weighted distribution displays the count, or the number, of particles in each size bin. Collectively the bins encompass the entire range of data. They are not necessarily the same size; the range of

Substance	Purity	Supplier
Sodium nitrate	AR	AnalaR
Lithium nitrate	AR	Sigma Aldrich
Benzoic acid	AR	AnalaR
Sodium bicarbonate	AR	AnalaR
m-hydroxybenzoic acid	CP	Sigma Aldrich
p-hydroxybenzoic acid	CP	BDH
Potassium oxalate	CP	Baker
Ferric chloride (60%)	CP	AnalaR
Sulfuric acid (95%)	AR	R. P. Normapur
Phenanthroline	AR	Serva
Sodium acetate	AR	AnalaR
Ferrous ammonium sulfate	AR	AnalaR
Potassium permanganate	AR	AnalaR
Sodium chloride	AR	Fisher
Potassium hydroxide	AR	AnalaR
Acetonitrile	HPLC	Scharlau
Trifluoroacetic acid	CP	Scharlau
Propan-2-ol	AR	Scharlau
Cyclohexane	CP	Unilab
Cyclohexanol	CP	Unilab
Cyclohexanone	CP	Unilab
Benzene	AR	Riedel-de Haen AG
Phenol	CP	May & Baker
m-nitrophenol	CP	BDH
p-nitrophenol	CP	BDH
o-nitrophenol	AR	Riedel-de Haen AG
Nitrobenzene	AR	AnalaR
Carbon monoxide (g)	Ultra High Purity	BOC
Carbon dioxide (g)	Food grade	BOC
Nitrogen (g)		Southern Gas
Oxygen (g)		Southern Gas
Argon (g)		Southern Gas

Table 2.3: Sources and purities of chemicals used.

diameters collected in each bin will again depend on the nature of the aerosol. Frequency histograms will be used throughout this thesis to display particle size distribution data.

Figure 2.11 shows a frequency histogram. The bins, corresponding to specific ranges of particle diameter, are plotted on the x-axis. The frequencies or, in this case, particle counts, are indicated by the heights of the bars. Because diameter is a continuous (not discrete) property, the ranges of the bins follow on from each other and there is no gap between bars. The mode of the data is readily seen and the overall shape of the distribution is clear. In the limit, as the bin size shrinks to zero, the histogram becomes the continuous function $\frac{dN}{d\,d_p}$. $\frac{dN}{d\,d_p}$, where d_p is the diameter of the particle, is used to denote a differential number-weighted particle size distribution. It is properly thought of as a number density rather than a number concentration. More generally, $\frac{dW}{d\,d_p}$ is used to represent a general distribution without specifying the weighting as number, surface or mass[3].

In aerosol science, the particle diameter is frequently not the only dimension of interest. Both the surface area and the mass of the aerosol are often important. So, in addition to number-weighted particle size distributions, as in Figure 2.11, surface area-weighted particle size distributions and mass-weighted size distributions can be calculated. Examples of a number-weighted distribution and the corresponding surface area- and mass-weighted distributions are shown in Figure 2.12. These distributions are easily calculated (assuming one knows the density of the particles in the latter case) but can have strikingly different frequency distributions. Because of the cubic dependence on radius in a mass-weighted particle size distribution, a small number of particles with large diameters can have a huge effect on the distribution. In general this thesis will deal with number-weighted size distributions, and care will be taken to clarify the data or discussion if this is not the case.

2.8.2 Log-normal particle size distributions

An ideal experimental aerosol generator would generate a monodisperse distribution of particles. Realistically, however, the actual distribution achieved will be polydisperse. In a laboratory situation a geometric standard deviation of about 1.1 is generally con-

[3]The notations $\frac{dS}{d\,d_p}$ and $\frac{dM}{d\,d_p}$ are used to denote differential surface- and mass-weighted size distributions respectively, while $\frac{dW}{d\,d_p}$ is used to represent a general distribution without specifying the particular weighting.

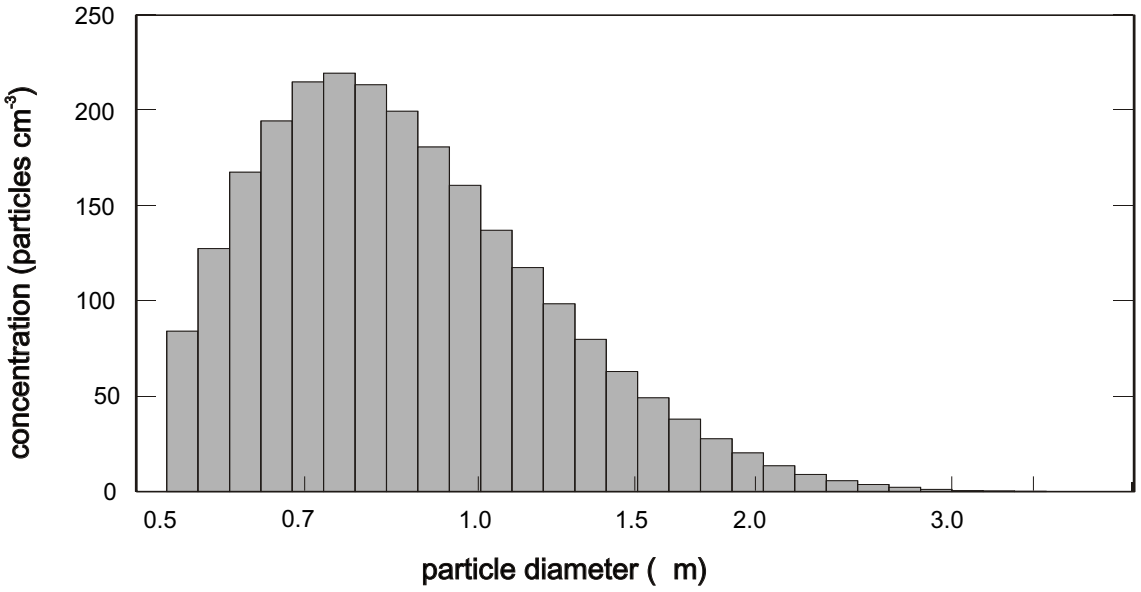

Figure 2.11: A typical log-normal size distribution from data collected by the Aerosol Particle Sizer (APS, see Section 2.4). The x-axis has a logarithmic scale so the log-normal distribution is transformed to a normal distribution.

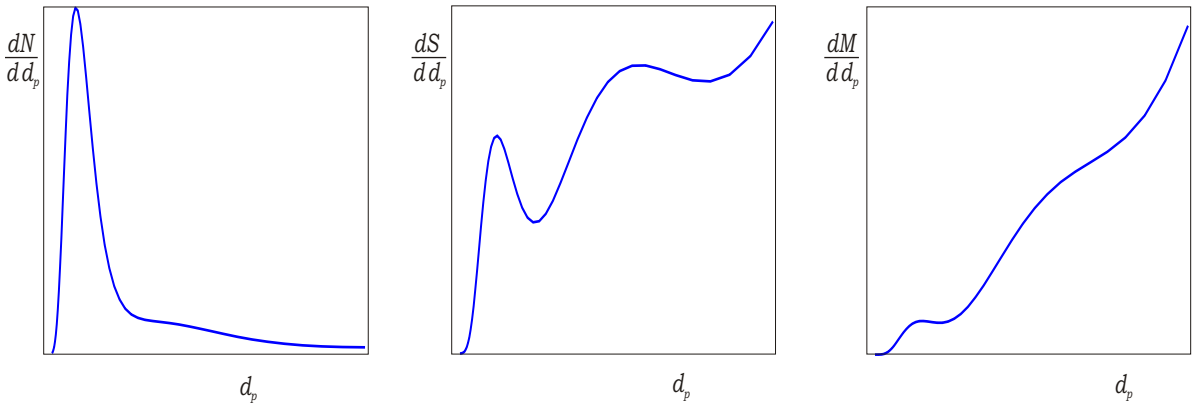

Figure 2.12: A comparison of number-, surface- and mass-weighted particle size distributions of the same aerosol.

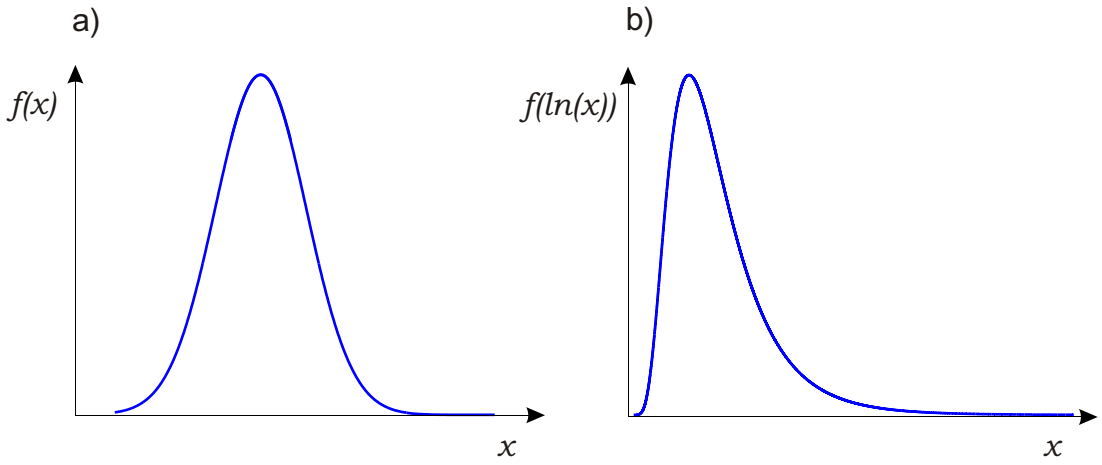

Figure 2.13: (a) A normal distribution (Gaussian). (b) A log-normal distribution.

sidered monodisperse, although the definition of monodispersity will depend upon the application [79].

Aerosols generated mechanically, whether from sea spray or in a laboratory nebuliser, tend to exhibit a log-normal size distribution. This is because the probability of generation of a certain size of droplet frequently depends on a multiplicative factor. For log-normal distributions, the descriptive parameters are the geometric mean (defined as the median for the log-normal distribution) and the geometric standard deviation, the ratio of the 50^{th} percentile diameter to the 16^{th} percentile diameter. As displayed in Figure 2.13, a log-normal distribution is a distorted normal distribution. Like the normal distribution, the log-normal distribution can be described by standard mathematical functions [82].

An experimental log-normal particle size distribution can be transformed to a normal distribution. A typical treatment is to divide the range of sizes up logarithmically, that is, in a logarithmic sequence, and plot the counts in each bin as a frequency histogram (Figure 2.11). A log-normal distribution plotted like this will have the standard Gaussian curve of a normal distribution. The normal distribution is described by the Gaussian curve of the form:

$$f(x;\mu,\sigma) = \frac{1}{\sqrt{2\pi}\sigma} e^{\frac{-(x-\mu)^2}{2\sigma^2}}, \tag{2.11}$$

where μ is the mean and σ is the standard deviation. The geometric mean and geometric standard deviation are then given by e^{μ} and e^{σ} respectively.

Alternatively, the geometric mean and geometric standard deviation can be computed directly from the data via:

$$\mu_g = exp\left(\frac{\sum_{channels} dW(channel) log(D_{mid}(channel))}{\sum_{channels} dW_{total}}\right),$$
$$\sigma_g = exp\left(\sqrt{\frac{\sum_{channels} \left(log\left(D_{mid}(channel)\right) log\left(\mu_g\right)\right)^2}{\sum_{channels} dW_{total}}}\right),$$

which are the equations used by the software controlling the APS [83]. The disadvantage of calculating the geometric mean and standard deviation directly from the data is that if the data is truncated the estimates will be biased. For this reason, in the research presented in this thesis, an estimate of the geometric mean and geometric standard deviation was calculated via a fitted log-normal distribution.

2.9 Particle size distribution characterisation

2.9.1 Experimental set-up for measurement of particle size distributions with the APS

A schematic of the set-up for particle size distribution measurement is shown in Figure 2.14. The set-up was the same as that used for the actinometric experiments (Chapter 3) and the benzoic acid experiments (Chapter 5), but the APS was not connected unless it was actually in use. The humidifier on the dilution gas line ensured that the gas (nitrogen) was humidified to a similar level as the aerosol sample. The flow meter downstream of the APS, F5, measures the exhaust flow from the APS, which is assumed to correspond to the total inlet flow sampled by the APS. The APS sampled from either of two ports, at the top or bottom of the chamber.

The 3 mm ID downstream impactor was used for all experiments with the APS; the 1 mm ID downstream impactor was used otherwise. The 1 mm impactor was better in general, because it removed a greater percentage of fine aerosol particles from the gas stream than the 3 mm one, but the 3 mm impactor was necessary because the pump could not maintain a chamber pressure below atmospheric pressure with the narrower impactor nozzle in place when extra gas was flowing into the system for aerosol dilution.

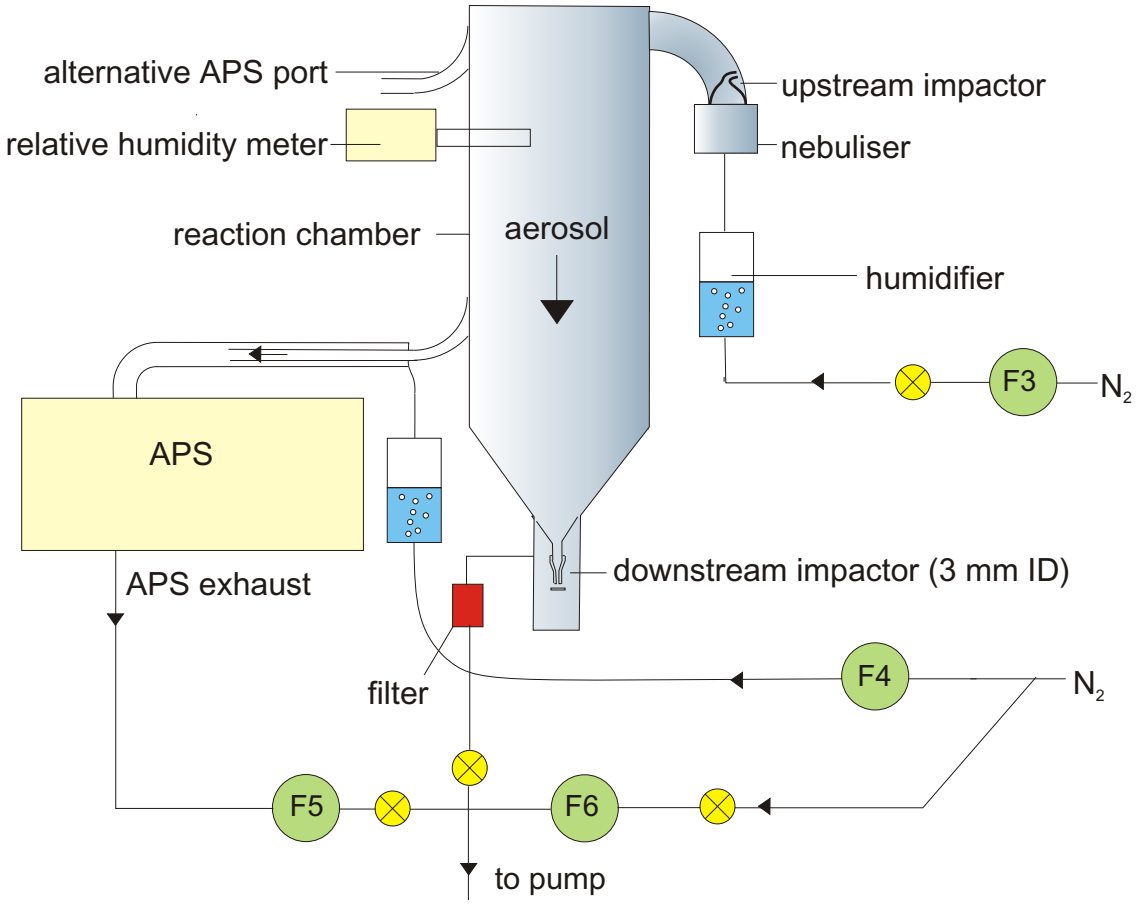

Figure 2.14: Schematic of the system for measuring particle size distributions with the APS.

Initially, a reference aerosol of $0.1\,\mathrm{mol\,L^{-1}}$ sodium nitrate was used to compare the efficiencies of the various impactors, and the difference in particle size distribution between irradiated and non irradiated aerosol.

The APS was not run simultaneously with the RGA mass spectrometer, partly because it proved difficult to run the software concurrently on the one computer that controlled both instruments and partly because the system leaked considerably more with the APS and diluter attached, which increased the chance of carbon monoxide leaks. While neither of these constraints prevented the APS being used to measure particle size distributions during the actinometric experiments and the aqueous phase radical scavenger experiments, the pump proved to be a limiting factor. The pumping speed of the KNF diaphragm pump was not fast enough to cope with the increased flows used when the APS was running combined with the pressure difference over the 1 mm nozzle used downstream of the chamber. The system worked well with the 3 mm nozzle downstream instead, but the volume of aerosol impacted, and hence the amount of product collected, was considerably less.

2.9.2 Operational issues

In 2005 the internal APS flow meter which controlled the bypass pump was found to be giving an incorrect reading, resulting in high sample flows and distorted distributions. The APS was returned to TSI for repair and calibration.

The ratio of the sample flow to the sheath flow inside the APS is supposed to be maintained at a constant ratio of 1:4. However, even after the calibration, the total flow at the APS inlet was only $4.5\,\mathrm{L\,min^{-1}}$ instead of the stated $5\,\mathrm{L\,min^{-1}}$. This appeared to be due to limitations in the accuracy of the APS flow meters when the pressure at the APS inlet was lower than 1 atmosphere (pressures of around 985 to 990 mbar were typical). The ratio of the flows was checked when the APS was offline and was found to be reasonably close to 1:4 at atmospheric pressure, 1013 mbar.

Earlier, it had been noticed that measurements of diluted aerosol were giving narrower distributions with a smaller geometric mean diameter than the similar but undiluted aerosols measured previously. It is suspected that for the undiluted aerosol the high concentrations resulted in droplets coalescing between the chamber and the APS, producing larger droplets of more widely varying diameters than in the actual aerosol.

This effect was seen again later, even with the diluter, when the aerosol was generated from more concentrated solutions of electrolyte. A $5\,\mathrm{mol\,L^{-1}}$ solution of lithium nitrate generated an aerosol with particle concentrations later calculated to be of the order of 300 000 particles per cubic centimetre. This is far higher than the APS can measure, even with the sampled aerosol being diluted by a factor of 13.6. In these instances, the particle concentration was estimated by increasing the dilution gas and extrapolating from reliable data in a plot of sampling flow versus particle concentration (see Section 2.9.6).

The maximum particle concentration the APS can measure is around 3 000 particles $\mathrm{cm^{-3}}$. Above this concentration, the APS can still measure particle distributions, but will measure many more instances of 'Event 3' due to multiply crested signals (see Section 2.4.1). The measured particle size distributions did not change markedly with dilution, which inspires confidence in the particle sizing abilities of the APS.

It should be noted that since the APS classified the particles based on their diameter, mass-weighted size distributions calculated from number-weighted size distributions were likely to have biases. This applied regardless of whether the calculations were performed with the APS instrument manager software or whether they were performed with the raw data with external software. To get a truly accurate mass-weighted size distribution it would be necessary to use a technique like multistage impaction, which measures the mass of aerosol on the filters at each stage [84].

2.9.3 Median particle diameter

The median[4] particle diameter was seen to decrease very slightly as the aerosol was diluted to a greater extent (Figures 2.15 and 2.16).

The range of sampling flows over which the particle size distribution was measurable was much smaller for concentrated nitrate solutions than dilute ones, consistent with the total particle number concentration being about three times higher for the very concentrated nitrate solutions. Over this small range, the range of median particle

[4]Since the particle size distribution is expected to be log-normal, the median diameter and the geometric mean should correspond, as explained in Section 2.8. The term 'median' used here applies to the experimental data with the truncation taken into account, *i.e.* it is the mid-point of the bin with the highest concentration. 'geometric mean' is used to describe the equivalent parameter of fitted log-normal distributions.

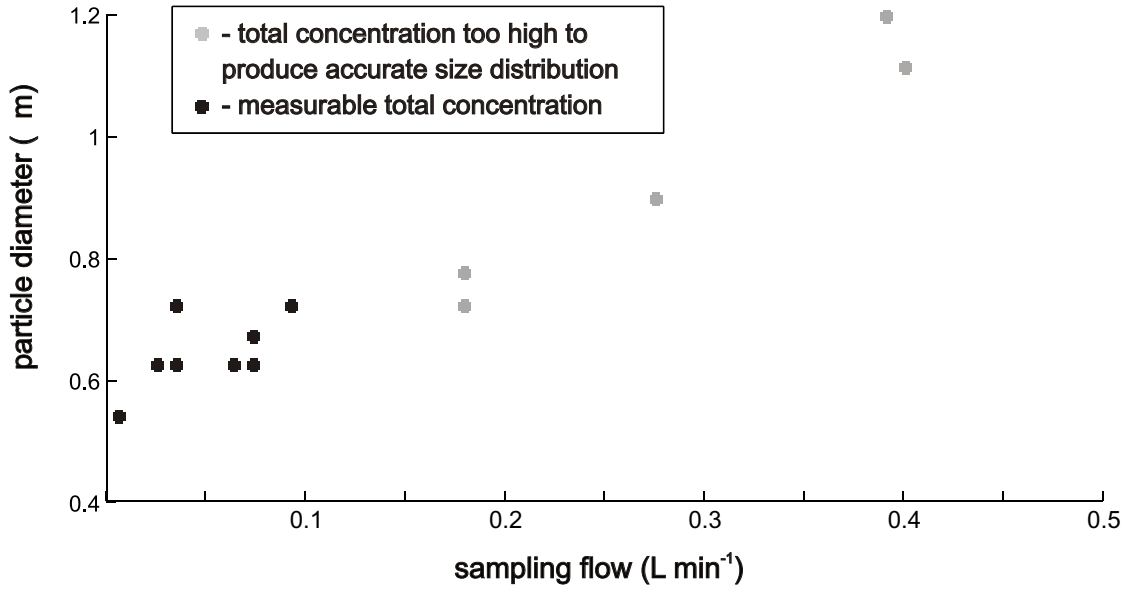

Figure 2.15: Sampling flow versus aerosol particle median diameter for concentrated ($2\,\mathrm{mol\,L^{-1}}$) sodium nitrate.

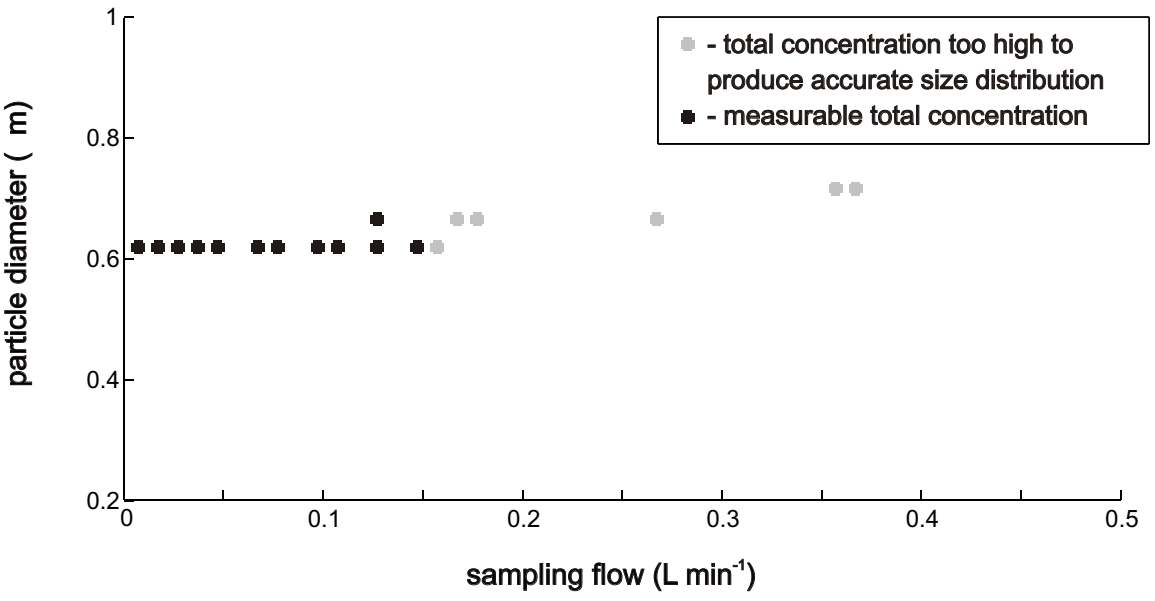

Figure 2.16: Sampling flow versus aerosol particle median diameter for dilute ($0.1\,\mathrm{mol\,L^{-1}}$) sodium nitrate.

diameters was very similar to the range for the dilute nitrate solutions.

The slight shift in measured diameter could be due to several causes. It is likely that the sampling was biased towards smaller particles due to the dilution process, such as larger particles being lost from the sample due to turbulence or due to gravitational settling. Also, particles may have been removed via conglomeration due to the high particle concentration in the APS inlet or the sampling tube.

The sampling flow is calculated to be the difference between the dilution flow and the APS exhaust flow, since the difference in flows must be made up by a flow from the chamber. It is not possible to measure the sampling flow directly since doing so would both damage the flow meter and remove the aerosol from the gas stream. Because this calculation is a small difference between two relatively large flows, its uncertainty is high.

Turbulence within the inlet

Turbulence should be at a minimum when the velocities of the sampling flow and the dilution flow are equal, as explained in Section 2.4.3. At the velocities typical for the sampling flow of the diluter, the penetration efficiency of all diameters of particles within the APS's measurement range (that is, 0.5 to 20 μm) will be greater than 97%. At flows of only 0.01 L min^{-1} (the limit of resolution for a 10 ksccm flow meter) the gas velocity in the sampling tube is 0.002 m s^{-1}. Larger particles are less likely to be affected by turbulence, so have a higher penetration efficiency: 99% of 2 μm particles would be carried through the sampling tube [77]. Thus, turbulence is not expected to have a significant effect on the measured particle size distributions.

Gravitational losses within the inlet

The gas travels a horizontal distance of 300 mm through the sampling tube before it is diluted. This is the narrowest part of the system and therefore the place where the greatest aerosol losses are expected. The inner radius of the sampling tube is 1.625 mm for the majority of its length. A particle in the tube would have on average about 1 mm of vertical distance to fall before it hit a surface. So any particles with settling velocities greater than 1×10^{-5} m s^{-1} are likely to be lost to the walls of the sampling

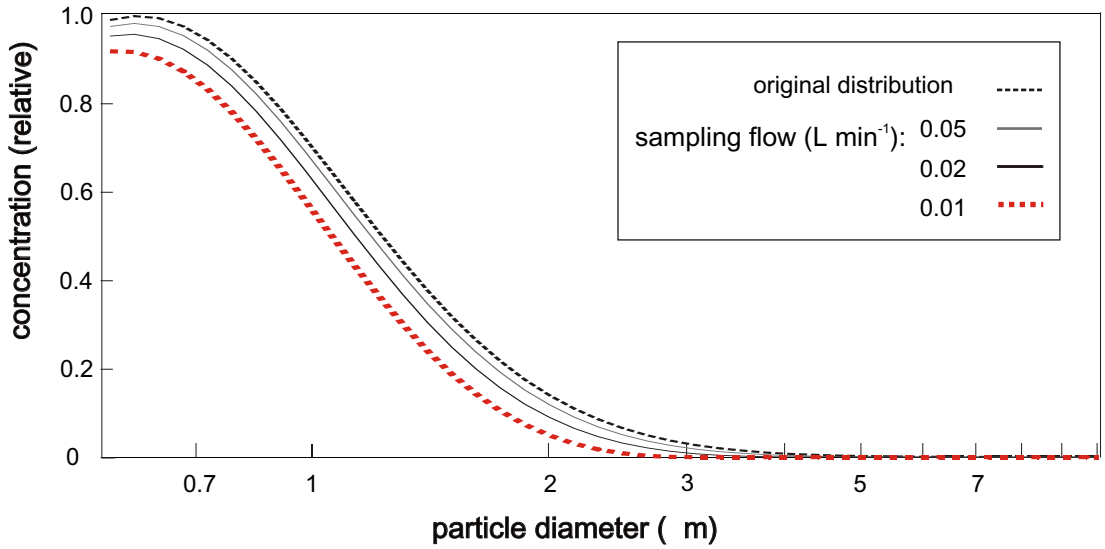

Figure 2.17: Particle size distribution: effect of gravitational losses as sampling flow decreases.

system. Baron's *Aerosol Calculator* Excel spreadsheet [77] has equations to calculate the penetration efficiency of inlets in terms of aerosol particle losses through gravitational settling, assuming a circular cross section and a parabolic flow distribution (a feature of laminar flows) [79]. For a given settling velocity, the geometries of the sampling tube and the aerosol flow distribution dictate the penetration efficiency. The *Aerosol Calculator* spreadsheet was once again used to estimate these efficiencies. When these calculated efficiencies were applied to a model log-normal distributions, the shape and the geometric mean of the distributions changed, particularly for model distributions with geometric mean diameters greater than 1 μm. For more typical geometric mean diameters of 0.6 μm, the only major effect on the model distributions was the decrease in total concentration.

Figure 2.17 depicts the change in a model log-normal number-weighted particle size distribution, with geometric mean 0.59 μm and standard deviation 1.85 μm, as the sampling flow was decreased. The geometric mean and the standard deviation of the distribution decreased very slightly relative to the original distribution. The total concentration was significantly lower and the shape of the distribution was no longer exactly log-normal. With a very low sampling flow (0.01 L min^{-1}) the geometric mean decreased to 0.58 μm and the standard deviation decreased to 1.71 μm. The APS data showed similar effects

as the sampling flow rate changed.

2.9.4 Particle size distribution changes over time

In general, the geometric mean diameter increased slightly during the course of an experiment. This was consistent with some evaporation having occurred in the nebuliser and the solution that remained in the nebuliser having become subsequently more concentrated. The median diameter of aerosol sampled from the upper port of the chamber was very similar to the median diameter of samples from the lower port of the chamber.

The effect of the lamp on the particle size distribution was smaller than the variation between repeated experiments. The Vaisala relative humidity/temperature probe measured a rise in the temperature inside the chamber when the lamp was on, which corresponded to a drop in relative humidity. The rate of evaporation from the aerosol should be such that the relative humidity corresponds to the activity of water in the aerosol droplets. Since the temperature was also seen to rise, it was likely that the actual vapour pressure of water in the chamber is constant and it was only the *relative* humidity that changed. The Vaisala probe was positioned so as not to be directly in the light path.

The increase in external temperature near the top of the chamber, as measured by an alcohol thermometer, agreed fairly well with the rise in internal temperature measured by the Vaisala probe. A typical rise in temperature for an irradiated experiment would be 4 °C. Most of this rise would take place in the first twenty minutes of the experiment, after which time the temperature would reach a steady state, the heat from the lamp being offset by the flow of air from the air-conditioned laboratory, the laboratory temperature being maintained at 20 °C.

In early experiments, the initial concentration of the solution had a marked effect on both the geometric mean and the standard deviation. In addition, the distributions observed were often bimodal. This bimodal character was largely eliminated by the inclusion of an upstream impactor in the flow system, as discussed below.

2.9.5 Mass-weighted particle distribution

In addition to the well defined distribution centred on a geometric mean of around $0.7\,\mu$m, the data calculated by the APS showed a large peak at larger particle sizes when the mass-weighted particle size distribution was plotted. It was initially unclear whether this was an artefact or not, which prompted the addition of the upstream glass impactor. The importance of the mass-weighted particle size distribution arises because the relative size of the two peaks indicated what diameter of particles constituted the greater mass of liquid aerosol particles. Since the dependence of mass on diameter is cubic, small numbers of larger particles can constitute sizeable proportions of the total mass.

If the APS data had proven not to be an artefact, the size of the peak at larger diameters in the mass-weighted concentration plots would have been of major concern. In order to measure any sort of reaction in an aerosol, it is vital to know the diameter of the aerosol particles in question, especially since both optical and surface effects will depend greatly on particle size. Analysing the raw data directly using the calibration data provided with the APS reproduced the particle size distribution at larger diameters. Therefore, the calculations carried out by the APS software were not the problem. However, Mitchell [84] warns against transforming data from a number-weighted distribution (such as the APS produces) to a mass-weighted distribution, since small variations in the former can lead to large variations in the latter.

While the presence of an upstream impactor was seen to have a significant effect on the number- and mass-weighted particle size distributions, the peak at large particle sizes in the mass-weighted distribution was observed to be present with and without this impactor. This confirmed it was an artefact resulting from compounded errors of slow particle detection by the APS.

However, number-weighted distributions of highly concentrated aerosol also showed a small peak at large particle sizes which disappeared as the dilution of the sampled aerosol was increased. Since this was a number-weighted distribution, it was a real, physical phenomenon. Given that this peak was only observed for highly concentrated aerosol, it is likely that it was a sampling artefact, possibly due to the coagulation of smaller particles between the chamber and the APS. This artefact was also observed with either upstream impactor installed.

Regardless of which of the two upstream impactors was used with which solution, liquid collected at the base of the impactor: the liquid which had been impacted then dripped downwards. Since this collected liquid was seen for even dilute solutions with the 5 mm ID nozzle impactor, it suggested that very large droplets, which were too large for the APS to measure, were being removed. In the absence of an upstream impactor, liquid was seen to collect on the horizontal surfaces on the tube connecting the nebuliser and the chamber.

From analysis of the APS data, it was apparent that the 5 mm ID impactor had little effect on the distribution for dilute solutions but did remove larger particles for concentrated solutions. The 4 mm ID impactor removed most particles larger than about $d_p = 1.5\,\mu$m. For dilute solutions, this corresponds to almost all of the aerosol being removed upstream of the chamber. In the case of concentrated solutions, the greater part of the aerosol was also removed, but the concentration of the remainder was still far in excess of what the APS could measure, even with the dilution system (as described in Section 2.4.3). For these reasons, the 5 mm impactor was used for dilute solutions (less than $1\,\mathrm{mol\,L^{-1}}$) and the 4 mm impactor was used for the more concentrated solutions.

2.9.6 Total particle concentration

The accuracy of the APS with respect to total particle concentrations has previously been measured with non-volatile liquid aerosol to be 10% at levels of 500 particles per cm^{-3} [85]. Solid particles can be counted with higher precision; they will tend to bounce off the walls of the sampling inlet, for example, to be re-entrained in the flow. That is, for every 500 particles sampled, 50 will not contribute to the reported total concentration. It must be emphasised, however, that these measurements were comparing the number particle size distribution as measured by the APS to the total mass concentration as collected on an impactor. Furthermore, this uncertainty is far smaller than that estimated for the particle number concentrations reported here. The necessity of diluting the aerosol to a large extent resulted in high uncertainties when extrapolating the dilute particle concentration measurements. In addition, the truncated distributions meant that the genuine total concentration had to be estimated from fitted log-normal distributions.

Figure 2.18 illustrates the extrapolation necessary in order to be able to obtain the

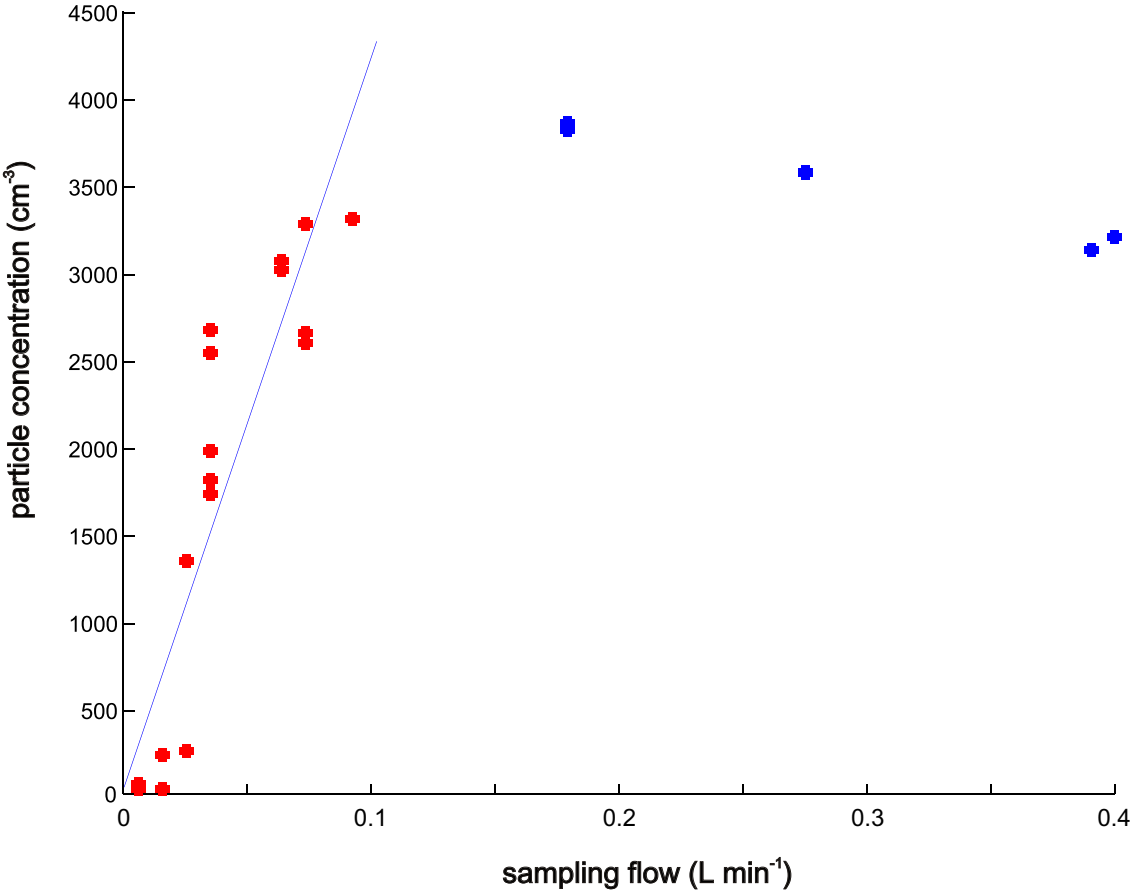

Figure 2.18: The sampling flow versus the total particle concentration for concentrated ($2\,\mathrm{mol\,L^{-1}}$) sodium nitrate. A least-squares fit to the total particle concentration data at measurable particle concentration levels was extrapolated to obtain the total undiluted concentration.

particle number concentration of the undiluted aerosol in the chamber. Above flows of about $0.1\,\mathrm{L\,min^{-1}}$ the concentration was too high for the APS to measure. An obvious 'knee' was seen at this point, as the detector became overloaded, but it was possible to obtain a line of best fit to the data to the left of the knee. The gradient of this valid data was reproducible in other experiments using the same solution. The value for the undiluted concentration depended entirely on this gradient, since the measured concentration is assumed to be zero at zero sampling flow. Extrapolating such a long way from the usable data increases the already high degree of uncertainty for this value.

The calculation of the sampling flow required a calculation of the difference between two measured flows. Because this difference is small, the relative uncertainties are high. It is not possible to measure the sampling flow rate directly without affecting the aerosol. The limitations imposed by the dimensions of the sampling system dictate the dimensions of the aerosol diluter and hence the applicability of any concentration measurements. The APS is a very sensitive instrument, under suitable conditions. Outside of these conditions, particle concentration measurements have to be considered as 'best guesses'.

2.9.7 Calculations of geometric mean and standard deviation

For each particle size distribution, the geometric mean and geometric standard deviation was calculated for a log-normal curve fitted to the data. As mentioned in Section 2.8, the geometric mean diameter of particles fell near the lower limit of the APS, so particles with diameters smaller than $0.5\,\mu$m were not counted. The resulting distribution was therefore a truncated log-normal curve. Matlab [86] was used to fit a log-normal curve to the truncated data to find the geometric mean and geometric standard deviation.

A Chi-squared test [87, 88] was applied to the synthesised log-normal curve, with respect to the APS data as a test of 'goodness of fit':

$$\chi^2_{c-1} = \sum_{i=1}^{c} \frac{(O_i - E_i)^2}{E_i}, \tag{2.12}$$

where the subscript on the χ denotes the degrees of freedom. O_i is the observed value while E_i is the expected value, and the sum is over c pairs of values. In this case $c = 27$, with the pairs of values being taken from the 4^{th} to the 30^{th} bin of the raw data, which encompassed all the bins with significant particle concentrations. While the synthesised curve appeared a reasonable fit to the data for many of the measured size distributions,

the high number of counts required that the experimental data matched the synthesised curve extremely closely for the fit to pass the Chi-squared test. From the standard Chi-squared test, none of the particle size distributions can be said to be precisely log-normal.

In most cases however, fitting a log-normal curve to the data still gave a better estimate of the geometric mean and geometric standard deviation than the APS could calculate from the truncated raw data. Log-normal fits were poorest for bimodal distributions and for distributions with median diameters smaller than $0.54\,\mu$m, which is the smallest diameter the APS can measure.

Whitby and Sverdrup used the Chi-squared test to fit log-normal curves to measured aerosol distributions [89]. They encountered similar issues with truncation, in their case for large particle diameters. They used a modified Chi-squared distribution:

$$\chi_n^2 = \frac{1}{T} \sum \frac{2\left(O_i - E_i\right)^2}{\left(O_i + E_i\right)} \tag{2.13}$$

where the 'n' denotes a normalised Chi-squared test (with $c-2$ degrees of freedom) and T is the sum of all the measurements. The denominator has been modified so that it is the average of the expected and observed values, with the rationale being that there is no reason to expect either one of O_i or E_i to be more accurate. This has the effect of dampening the Chi-squared test at the ends of the distribution so that a poor fit at the extremes does not dominate the goodness-of-fit test.

This normalised Chi-squared test was also applied to the APS data. The values for χ were around 0.15 to 0.3, with the highest value being that representing the highly concentrated lithium nitrate solutions ($5\,\mathrm{mol\,L^{-1}}$). In comparison, Whitby and Sverdrup's tri-modal fits achieved values as low as 0.005.

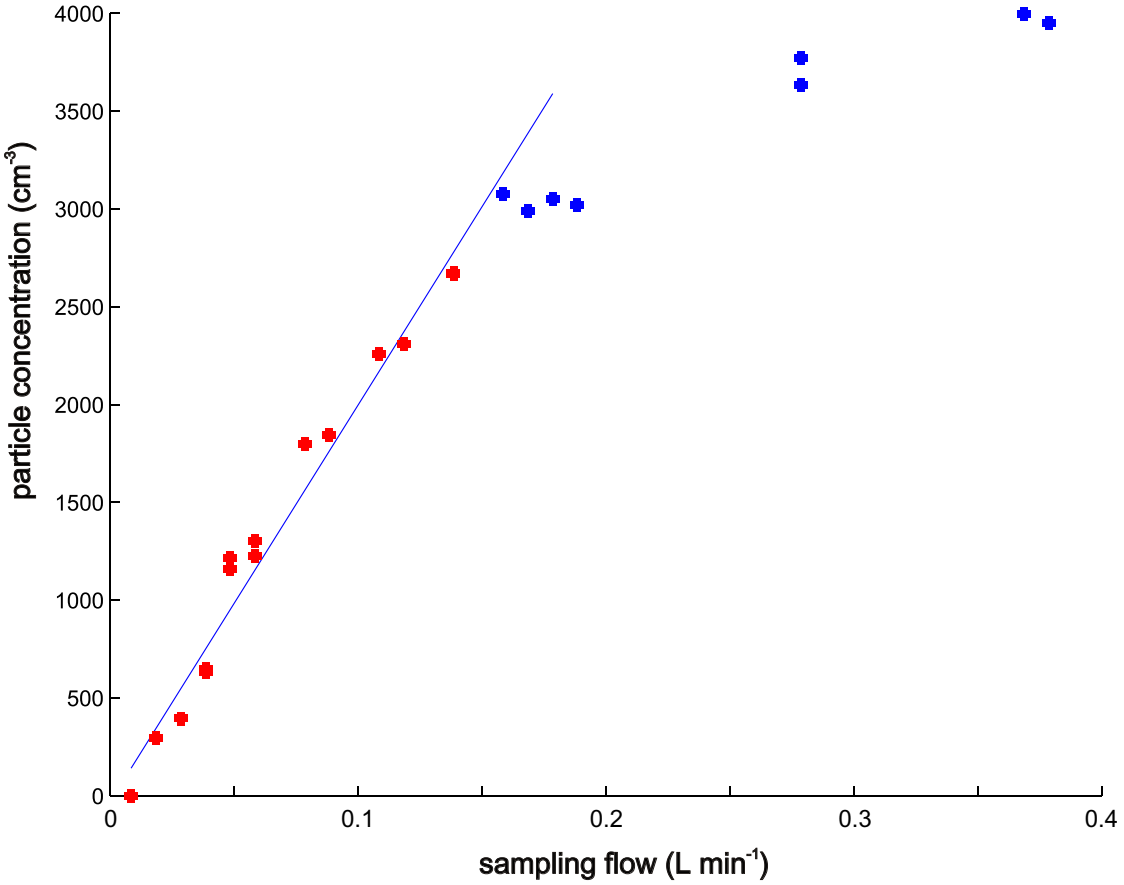

Figure 2.19: The sampling flow versus the total particle concentration for dilute ($0.1\,\mathrm{mol\,L^{-1}}$) sodium nitrate. Also shown is a least-squares fit to the data at measurable concentrations.

Chapter 3

Experimental: Actinometry

The rate of photolysis of nitrate depends directly on the amount of light present in the system. In order to calculate the quantum yields for the nitrate photolysis, it was necessary to calculate the number of photons absorbed by the nitrate solution during the course of the experiment. In addition, the first part of the hypothesis that inspired this work was that the radiant intensity[1] might be enhanced in a liquid aerosol. One way to prove this is to measure the intensity in the droplets directly. A measure of the relative enhancement of the intensity in the droplets was also necessary in order to be able to compare the yield of hydroxyl radical from the droplets with the reported hydroxyl radical quantum yields for bulk liquid solutions. The irradiance measurement, then, can be seen as a calibration of the aerosol system: a necessary reference for any aerosol hydroxyl radical yields.

Actinometry is the measurement of irradiance. While physical methods of measuring irradiance are commonplace (using photodiodes or photomultipliers, for example) they are not always suitable or convenient for specific systems. An alternative is chemical actinometry, which involves measuring the irradiance via the yield from a chemical reaction. It requires a photolysis process with a known quantum yield and easily analysed reaction products. The chemical being photolysed is described as the actinometer. Chemicals can be inserted into places where diodes cannot. Specifically, solutions can be nebulised into aerosols which are then irradiated. Assuming that the actinometer is distributed homogeneously inside the droplets, the extent of reaction of the chemicals in the droplets corresponds to the light intensity within the droplets. The aerosol is then collected by impaction and analysed.

[1] 'Irradiance' is used to describe the amount in light transmitted in one direction, per unit area. Inside a droplet, where resonant modes exist, it makes more sense to use the more vague term 'intensity' since the light is not coming from one direction.

By measuring the number of moles of a product B after irradiation time t, the light intensity at the front window of a photochemical cell can be calculated via the relationship:

$$I_0{}^i = \frac{n_B}{\Phi\, t\, (1 - 10^{-\epsilon[\mathrm{A}]_l})},$$

where $I_0{}^i$ is the light intensity incident just inside the front window of the photochemical cell, Φ is the quantum yield (tabulated) for product B, t is time, [A] is the concentration of the actinometer, ϵ is the molar absorption coefficient, l is the path length and n_B is the number of molecules of B formed [58]. Ideally the quantum yield should be independent of the wavelength of the light. Light intensity is a badly defined quantity that depends very much on the experimental set up. Here it is related to the irradiance E by the cross sectional area A of the photochemical cell:

$$E_0{}^i = \frac{I_0{}^i}{A}. \tag{3.1}$$

The irradiance is the radiant energy across a surface, irrespective of direction. It is often quoted in terms of Watts per square metre; here quanta per second per square metre will be used since the quantum yield is the quantity of interest.

For a liquid aerosol, the absorption coefficient for an ensemble of particles, b_{abs}, can be used (Section 1.5.2):

$$E_0{}^i = \frac{n_B}{\Phi\, t\, b_{abs}}. \tag{3.2}$$

The absorbance of a sample is defined as $A = log_{10}\frac{I_0}{I}$, where I_0 is the incident intensity of light and I is the intensity after the light has passed through the sample. The Beer-Lambert law[2] relates the absorbance to the concentration $[A]$, path length l and the decadic molar absorption coefficient, ϵ [90]:

$$A = log_{10}\frac{I_0}{I} = \epsilon\,[B]\,l. \tag{3.3}$$

3.1 Chemical actinometers

3.1.1 Potassium ferrioxalate

As the 'industry standard' of actinometers, potassium ferrioxalate was the actinometer originally chosen for the research reported here. It is simple to use and sensitive

[2]Equation (1.13), derived in Section 1.5.1.

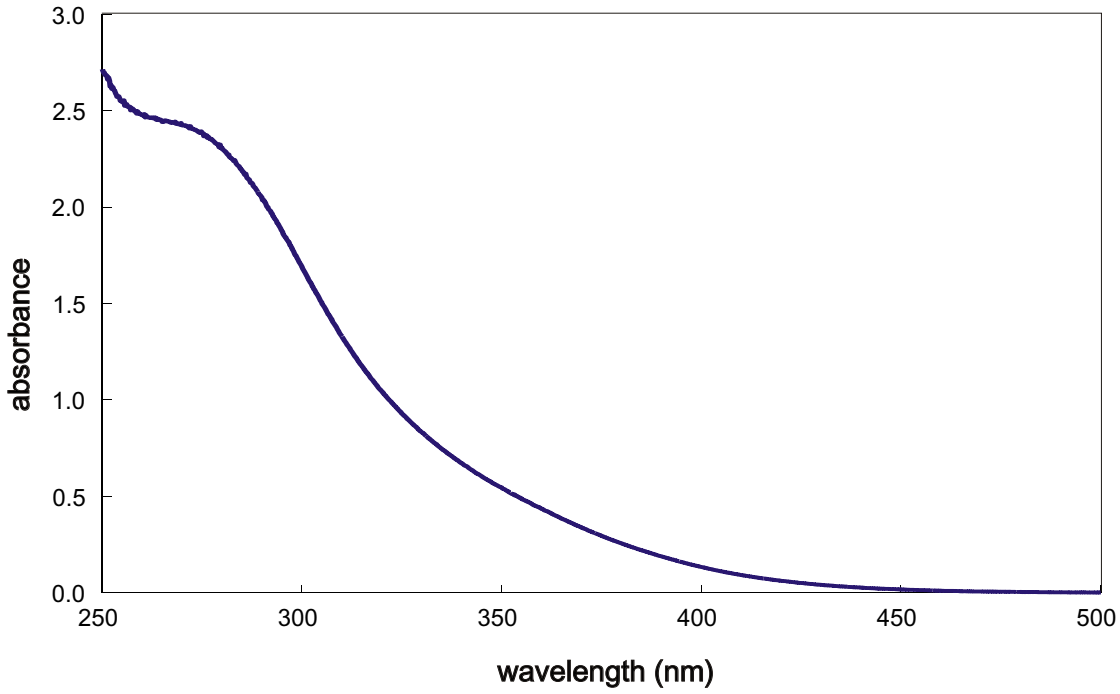

Figure 3.1: UV-visible absorption spectrum of potassium ferrioxalate solution (6×10^{-4} mol L^{-1}, 1 cm path length), measured on a GBC 920 UV-visible diode array spectrometer.

over a wide range of wavelengths, including the regions relevant to the photolysis of nitrate (305 nm). The potassium ferrioxalate actinometer was first developed in 1929 by Allmand and Webb [91] and has since been refined and improved [92]. It is easy to prepare and its use is well described in Calvert and Pitts' *Photochemistry* [58].

Potassium ferrioxalate undergoes photoreduction from $K_3Fe(C_2O_4)_3$ to Fe^{2+}. The complete redox reaction is [93]:

$$\begin{aligned} Fe(C_2O_4)_3{}^{3-} + h\nu &\rightarrow Fe^{2+} + 2C_2O_4{}^{2-} + C_2O_4{}^{\cdot -}, \\ C_2O_4{}^{\cdot -} &\rightarrow CO_2{}^{\cdot -} + CO_2, \\ CO_2{}^{\cdot -} + Fe(C_2O_4)_3{}^{3-} &\rightarrow Fe^{2+} + 3C_2O_4{}^{2-} + CO_2. \end{aligned} \tag{3.4}$$

The decomposition of the $C_2O_4{}^{\cdot -}$ radical is fast. It produces $CO_2{}^{\cdot -}$ which can then reduce another ferrioxalate molecule. This results in a quantum yield for Fe^{3+} greater than 1 ($\Phi = 1.24$ at 313 nm for 0.006 mol L^{-1} ferrioxalate solutions). The quantum yield is wavelength dependent and to some degree concentration dependent. However,

the photodecomposition of ferrioxalate is linear with respect to irradiance and largely independent of temperature [91]. The concentration of the products can be measured by UV-visible spectroscopy.

3.1.2 Alternative actinometers

During experimentation it became clear that potassium ferrioxalate was being reduced by aluminium components in the chamber, in the absence of light:

$$Al + 3Fe^{3+} \rightarrow Al^{3+} + 3Fe^{2+}. \tag{3.5}$$

Therefore, an alternative actinometer was sought.

Actinometers can be either gaseous, solid or liquid phase. Investigating the irradiance inside aerosol droplets obviously called for a liquid phase actinometer. This is by far the largest category of actinometers and includes organic and inorganic chemicals. None of the alternative actinometers appeared as simple to use and as easily analysed as potassium ferrioxalate. Uranyl oxalate looked to be a potential candidate and was trialled briefly but, like potassium ferrioxalate, was also reduced in the presence of aluminium. It is also very toxic and difficult to analyse, requiring titration with oxalic acid. Any analysis involving a redox reaction was best avoided, since this was the cause of the dark reaction of the potassium ferrioxalate. This ruled out most of the inorganic actinometers, like malachite green leucocyanides, vanadium(V)-iron(III) oxalate and monochloroacetic acid, all of which are known to undergo dark reactions. Reinecke's salt ($KCr(NH_3)_2(NCS)_4$) was rejected because of its thermal instablility [58, 94, 95, 96].

This left the organic actinometers. Many otherwise suitable organic actinometers, like butyrophenone or piperylene, would have required analysis via online gas chromatography. Most of the aqueous phase organic actinometers could be analysed by High Performance Liquid Chromatography (HPLC). This instrumentation was available, and importantly, allowed offline processing of the collected samples. There is a vast range of organic actinometers, spanning the entire visible and ultraviolet spectrum [96]. Not all of them are well characterised, however.

Several recent papers describe the use of sodium nitrate, sodium nitrite and hydrogen peroxide as chemical actinometers. All of these compounds generate hydroxyl radical as a photolysis product. Detection of the hydroxyl radical is generally via a radical

scavenger. Recent investigations into nitrate photolysis [4, 97] have used benzene and benzoic acid as radical scavengers for the hydroxyl radicals produced in the photolysis of hydrogen peroxide and sodium nitrate. However, they originally used ferrioxalate actinometry to calibrate the quantum yields for the hydrogen peroxide photolysis.

Jankowski and Mopper [98] studied nitrate and nitrite as ultraviolet actinometers. Although the yields of hydroxyl radical from the photolysis of nitrate are low, the sensitivity is high because the hydroxyl radical is scavenged to form highly chromophoric products. In practice, such aqueous phase radical scavengers are not well characterised as actinometers, so it was still necessary to measure the irradiance independently.

So, the problem of finding a replacement for potassium ferrioxalate was not resolved. The lack of an obvious alternative actinometer meant that reducing the dark reactions occurring with potassium ferrioxalate was the best and simplest option. The aluminium components of the flow chamber were therefore replaced with Teflon and stainless steel, which reduced the extent of the dark reactions to manageable levels. However, the studies mentioned above did have a useful consequence: they suggested that liquid phase radical scavengers could be used as well as the gas phase scavenger carbon monoxide, to investigate the production of hydroxyl radical in sodium nitrate aerosol. This became a major part of the project and is discussed in Chapter 5.

3.2 Experimental procedures

Potassium ferrioxalate was prepared by adding ferric chloride to a hot solution of potassium oxalate. The mixture was cooled to 0 °C to crystallise, then recrystallised three times in warm water. The resultant green crystals were dried in air [99, 58]. Solutions of potassium ferrioxalate were made up with Milli-Q water and sulfuric acid ($0.05\,\mathrm{mol\,L^{-1}}$). The concentrations of ferrioxalate used were around 0.006, 0.05 and $0.15\,\mathrm{mol\,L^{-1}}$. The concentrations of the solutions were verified during the measurement of total iron and were within ±2% of the target concentrations.

An aerosol of potassium ferrioxalate was generated in humidified nitrogen at a flow rate of $4.4\,\mathrm{L\,min^{-1}}$, as in the other aerosol experiments. Experiments were run for 45 minutes. The power dissipation of the lamp and the pressure, the temperature and the relative humidity in the chamber were recorded at intervals of 15 minutes. The upstream glass

impactor of Figure 2.5, with an internal nozzle diameter of 5 mm, was used for the later experiments in this series. The measured yields of Fe^{2+} for the aerosol were similar with this impactor in place, although a smaller amount of liquid was found in the trap.

The aerosol was collected by impaction in the trap at the bottom of the chamber. The irradiated sample was washed from the trap with dilute (0.05 mol L^{-1}) sulfuric acid. The diluted sample was then weighed.

Bulk phase liquid actinometry was initially performed with a quartz cuvette positioned in the middle of the chamber. While these experiments generated reproducible results, the irradiance calculated was higher than expected, relative to the aerosol phase experiments. While the aerosol would fill the chamber, the cuvette was in the middle of the chamber, with an area of about 6 cm^2. The light emitted by the lamp was focussed onto the dielectric mirror to maximise the light reaching the chamber; that is, the light was not collimated. Within the chamber, the beam diverged and was reflected off the walls. It appeared that the irradiance in the centre of the chamber was higher than the average irradiance, so that the cuvette was not measuring a representative irradiance.

To measure the intensity over the entire width of the chamber, a close-fitting Petri dish filled to a depth of 10 mm with actinometer was placed at various heights in the chamber. The Petri dish was supported by sections of PVC pipe. It sat squarely on top of a black piece of cardboard, on top of one or more sections of the pipe. During irradiation of the Petri dish, nitrogen was set to flow at 1 L min^{-1} through the small (0.5 mm) gap between the dish and the chamber wall, to maintain an oxygen-free atmosphere. Because of the high sensitivity of the ferrioxalate actinometer, it was necessary to limit the light with a neutral density filter (O.D. = 2.0) in addition to the narrow band dielectric filter. Both filters were used for all actinometric experiments with potassium ferrioxalate.

3.2.1 Analysis of ferrioxalate actinometer

The procedure to analyse the concentration of Fe^{2+} ions after irradiation is described in Calvert and Pitts' *Photochemistry* [58]. Phenanthroline (phen) was added to the samples to complex with the Fe^{2+}. The Fe^{2+}-phen complex formed had a deep orange colour with an absorption maximum at 510 nm, which can be easily measured via UV-visible spectrometry. A GBC 920 UV-visible diode array spectrometer was used to measure the concentrations of iron-phenanthroline complex as well as absorption spectra of the

aerosol solutions.

An aliquot of irradiated potassium ferrioxalate was placed in a volumetric flask. Calvert and Pitts suggest a 10 mL aliquot in a 25 mL volumetric flask. 1 mL of 0.1% phenanthroline solution and 5 mL acetic acid buffer solution[3] was added to this, and the solution made up to 25 mL with Milli-Q water. For this experiment, sample aliquots were typically 1 mL. 10 mL of dilute sulfuric acid was added to maintain the acidity of the ferrioxalate solution. The aliquot of phenanthroline was increased to 3.5 mL when it became apparent that not all the Fe^{2+} was forming a complex with the phenanthroline.

Although the aerosol collected on the impactor will have changed in concentration due to evaporation, the amount of product B (Fe^{2+}) will be constant. This is the critical quantity for determining light intensities. This was not initially realised, and a large amount of effort was directed at determining the total iron (Fe^{2+} + Fe^{3+}) concentration, in order to calculate the pre-evaporation/dilution concentration of Fe^{2+}. This data was not directly useful, since the volume of product that was collected had not been measured. However, since the volumes involved are similar, they can be retrospectively calculated from the data from later experiments where the total mass of solution was measured, and are presented for comparison.

Following Knox's example [42], the UV-visible analysis initially involved measuring the concentration of the Fe^{2+}-phen complex via the absorbance at 510 nm and measuring the concentration of Fe^{3+}-phen at 396 nm. This would be expected to be straightforward since Fe^{3+}-phen does not absorb at 510 nm and the molar extinction coefficient of both species is the same at 396 nm. However, most of the Fe^{3+} remains bound as the ferrioxalate complex and does not bind preferentially to the phenanthroline. This complicated the calculations and decreased the sensitivity of this method. Therefore, a second method suggested by Knox was applied: the total iron concentration was established by reducing all the Fe^{3+} to Fe^{2+} with ascorbic acid. The Fe^{2+} would then form the complex with phenanthroline and be measurable at 510 nm. As Knox notes, this requires two measurements for each sample. Ascorbic acid was added together with the phenanthroline and buffer solution when measuring total iron concentration.

The experimental samples were typically measured two or three times, with separate measurements made for Fe^{2+} concentration and for total iron concentration. Each of

[3] 360 mL of 0.5 mol L^{-1} H_2SO_4 + 500 mL 2 mol L^{-1} $NaCH_3CO_2^-$.

these analyses involved adding the sample to the phenanthroline/buffer solution, leaving these solutions for at least four hours, then measuring the absorbance of the solution three times.

3.2.2 Calibration of spectrometer

The UV-visible spectrometer was calibrated as recommended by Calvert and Pitts [58]. A standard solution of ferrous ammonium sulfate (FAS, $FeSO_4(NH_4)2SO_46H_2O$) was used to standardise solutions of potassium permanganate ($KMnO_4$). These were in turn used to standardise a fresh solution of ferrous sulfate ($FeSO_4$, $0.1\,\mathrm{mol\,L^{-1}}$). The ferrous sulfate solution was then diluted to $4{\times}10^{-4}\,\mathrm{mol\,L^{-1}}$ and aliquots of the ferrous sulfate solution were added to phenanthroline/buffer solutions as described above. The concentrations of $FeSO_4$ were chosen so that the absorbances of the resulting Fe^{2+}-phen solutions would range from 0 to 1.

Plotting absorbance against concentration resulted in a linear plot with a slope corresponding to the molar absorption coefficient (ϵ) of Fe^{2+}-phenanthroline. The slope was calculated by a least-mean-squared fit to be $(11040 \pm 90)\,\mathrm{L\,mol^{-1}\,cm^{-1}}$ This is in agreement with previously measured values for ϵ ($1.11\times\ 10^4\,\mathrm{L\,mol^{-1}\,cm^{-1}}$ [58]).

3.2.3 Precautions necessary for ferrioxalate actinometry

At the concentrations in use up to November 2005, the amount of Fe^{2+} produced from photoreduction of potassium ferrioxalate was high compared to the amount of Fe^{3+} present (as potassium ferrioxalate). The calculation of light intensity as outlined by Calvert and Pitts [58] relies on the concentration of the product being low (with respect to the actinometer) so that the concentration of the actinometer can be assumed to be constant and the kinetics can be treated as zeroth-order [100]. This was not the case for either the bulk solution in the cuvette or for the nebulised actinometer, with percentage conversions of the actinometer being around 40% and 70% for the bulk and aerosol phases respectively. Using a higher concentration of actinometer in combination with a neutral density filter (OD = 1.0 or higher) solved this problem. In the bulk solution case, having a solution of $0.15\,\mathrm{mol\,L^{-1}}$ potassium ferrioxalate resulted in a percentage conversion of around 1%. This was sufficiently low to enable the irradiance to be calculated. This linear dependence of irradiance on amount of iron(II) produced

(Equation 1.14) holds for irradiance up to 6.5×10^{20} quanta s^{-1} cm^{-2}. The irradiance measured for the chamber is below this limit by several orders of magnitude.

Kirk and Namasivayam [101] investigated the reliability of the ferrioxalate actinometry, particularly with regard to the analysis with phenanthroline as a complexing agent. At the higher concentration (0.15 mol L^{-1}), they found that ferrioxalate actinometry was not reliable unless the solutions were left for several hours after the phen/buffer solution was added. This could be remedied by adding phenanthroline in greater excess. A ratio of 8:1 phen to Fe^{2+} needed 17 hours to come to equilibrium, and even then, competition from the Fe^{3+} ions resulted in the absorbance at 510 nm due to the Fe^{2+}-phen complex being only 70 % of that calculated theoretically. All the ferrioxalate actinometry performed during the experiments reported in this thesis was carried out with a ratio of phen to Fe^{2+} of at least 30:1, and the developing solutions were left for a minimum of three hours before they were analysed via UV-visible spectrometry.

Oxygen has been found to retard the decomposition of ferrioxalate, reoxidising Fe^{2+} to Fe^{3+} [91]. For this reason, all experiments were conducted under nitrogen, although the collection of the samples was carried out in air. Samples were analysed on the same day that they were collected, but they did not change appreciably in Fe^{2+} concentration if left for a longer time.

3.2.4 Effect of ionic strength of solution

The ionic strength of the solution might be expected to influence the particle number size distribution and particle concentration in the aerosol, as was seen for the sodium nitrate aerosol. To investigate whether this factor was significant for aerosols nebulised from the chemical actinometer, a solution 0.05 mol L^{-1} in ferrioxalate and 2 mol L^{-1} in sodium chloride was nebulised. However, non-irradiated aerosols showed considerable dark reactions. The Fe^{2+} concentrations were only around 25% higher for irradiated aerosols than non-irradiated aerosols. The photoreduction of potassium ferrioxalate, corrected for this dark reaction, was of the same order of magnitude as that seen for the 0.05 mol L^{-1} solutions of ferrioxalate with no sodium chloride.

Bulk liquid, non-irradiated mixed solutions of potassium ferrioxalate and sodium chloride placed in the trap for 45 min, with no irradiation, reacted to a similar extent to non-irradiated potassium ferrioxalate aerosol, suggesting that the impacted aerosol had

continued reacting in the trap as a bulk liquid when the sodium chloride was present.

3.2.5 Measurement of total iron deposited on walls of chamber

To ascertain the amount of aerosol being deposited on the walls of the chamber, after several experiments with ferrioxalate aerosol, the inside of the chamber was rinsed with Milli-Q water and the rinsings were collected. By measuring the mass of the solution and the concentration of total iron in the rinsing sample with UV-visible spectrometry, an amount of total Fe^{2+} and Fe^{3+} deposited on the walls could be calculated[4]: an average of 1.6×10^{-6} mol was adsorbed over the inner surface of the chamber.

3.3 Calculations

The set of three absorbance measurements taken for each sample was averaged. The final set of measurements taken during the UV-visible analysis was the absorbance of the blank solution. If the baseline had shifted significantly, it could be corrected for by assuming a linear shift over time, and subtracting this shift from the averages of the sets. If the UV-visible spectrometer was left to warm up for 30 minutes or more before any measurements were carried out, the baseline tended to be stable. After each set of measurements, the absorbance of air in the spectrometer chamber was measured. That is, the cuvette was removed and a scan taken with the chamber empty. This was used as an independent check to see whether the baseline correction was necessary.

The molar absorption coefficient for phenanthroline at 510 nm was measured experimentally as $11040\,\mathrm{L\,mol^{-1}\,cm^{-1}}$ (see Section 3.2.2).

Hence, the concentration of Fe^{2+} complexed with phenanthroline can be calculated. The total amount of Fe^{2+} in the sample is obtained by converting the mass of collected sample into a volume. The density of a solution of 0.05 $\mathrm{mol\,L^{-1}}$ potassium ferrioxalate was $1.013\,\mathrm{g\,mL^{-1}}$.

[4]The density of the rinsings was assumed to be that of water, $1.00\,\mathrm{g\,mL^{-1}}$ at 293.15 K.

Chapter 4

Experimental: Measurement of gas phase hydroxyl radical yields

4.1 Inline gas phase analysis with carbon monoxide as radical scavenger

The major hypothesis of this project was that the flux of hydroxyl radical, from the photolysis of nitrate, out of the aerosol droplets would be enhanced compared to the bulk liquid case. With inline mass spectrometry it proved to be marginally possible to measure this yield of carbon dioxide from the reaction of hydroxyl radical and the radical scavenger carbon monoxide (CO), with carbon monoxide of high purity and using the mass spectrometer's electron multiplier.

As mentioned in Section 1.1.1, carbon monoxide reacts with hydroxyl radical to produce carbon dioxide (CO_2) and a hydrogen atom:

$$CO + OH \rightarrow CO_2 + H \tag{4.1}$$

By measuring the concentration of CO_2 produced, the extent of escape of the hydroxyl radical into the gas phase would be able to be estimated, if carbon monoxide was completely insoluble. This is not the case, so the yield of carbon dioxide corresponded to the combined yields of carbon dioxide formed from the gas phase reaction and from the aqueous phase reaction of CO and OH.

4.1.1 Residual Gas Analyser

Mass spectrometry was used to measure both partial pressures in a flow system and the total pressure of CO_2 collected in a trap. The instrument used was an MKS PPT-C200-M3T Quadrupole Residual Gas Analyser (RGA). PPT stands for Partial Pressure

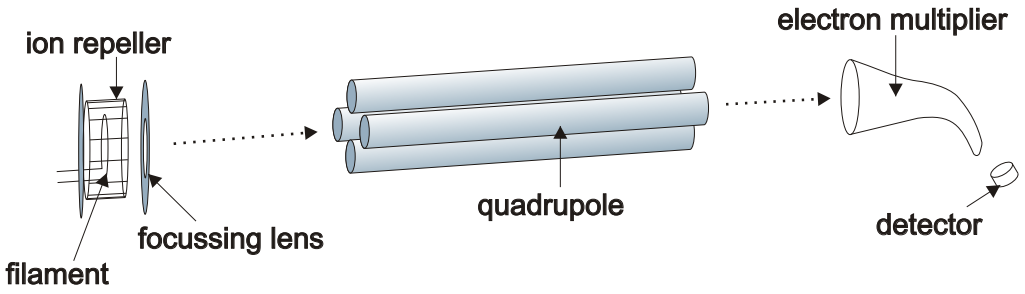

Figure 4.1: A schematic representation of the mass spectrometer. The ion cage, similar to the ion repeller but smaller, sits inside the filament. It is not included in this diagram for simplicity. Adapted from the RGA manual [102].

Transducer. This instrument is able to measure partial pressures of gases at atmospheric inlet pressures, via a pressure reduction manifold.

A mass spectrometer chiefly consists of an ion source, a mass filter and an ion detector. The ion source in this case consists of a thoria-coated iridium filament. Applying a potential to the filament results in electrons being emitted. The electrons have energies of 75 eV, enough to ionise most gases and the standard ionisation energy for mass spectrometry. A positively charged ion cage draws the electrons towards the gas molecules (or atoms) which are ionised and then focussed through a lens (a charged plate with a hole in it) towards the quadrupole mass filter and the detector (see Figure 4.1). Charged plates are used to deflect and channel the ions.

The quadrupole consists of four charged rods that can be tuned to collect ions of one particular mass to charge ratio (m/z)[1] at the detector. The ions are accelerated by superimposed DC and AC radio frequency electric fields. The ratio of the strengths of these fields determines the trajectory of each ion, depending on its m/z ratio. Normally, the quadrupole scans through a range of m/z ratios, dwelling for 10 to 150 ms at each[2]. From the current generated at the detector by ions with a particular m/z ratio, the partial pressure of ions with that m/z ratio can be calculated. Quadrupole systems discriminate in favour of low m/z ions, so a mass sensitivity factor must be included in

[1]The mass to charge ratio is the molecular mass of the ion divided by the electronic charge on the ion. It is measured in atomic mass units (a.m.u.).

[2]These values are defined by the user; the values mentioned are those used for this experiment.

the calculation to ensure the partial pressures for the various m/z ratios are consistent. Electron-impact ionisation cross-sections also vary from molecule to molecule.

For this particular instrument, the ion cage also functions as a total pressure detector. The current required to deflect the ions gives a measure of the total gas pressure at the ion source. If this pressure is too high (greater than 2×10^{-4} Torr) the PPT probe (the unit consisting of the ion source, quadrupole rods and detector) automatically shuts down.

If the ceramic insulators in the PPT probe become contaminated, the metal plates and cages in the ion source are not insulated from each other and do not direct the electrons and ions appropriately, and in the case of the ion cage, will not give an accurate total pressure. When the signal to noise ratio was seen to deteriorate to a point where the partial pressure measurements were off scale, the mass spectrometer was taken apart and found to have very dirty ceramic insulators. It is likely that the build up of carbon on these insulators was destroying their insulating properties. Once these and other accessible parts of the PPT probe were cleaned, the signal to noise ratio of the mass spectrometer was vastly improved. It was still necessary to use longer dwell times (150 ms), however, for the m/z values of greatest interest.

Electron multiplier

The sensitivity of the mass spectrometer can be increased with the use of an electron multiplier. Without the electron multiplier, the RGA can measure from 1×10^{-4} Torr down to 1×10^{-9} Torr in practice. With the electron multiplier, this range changes to from 1×10^{-7} Torr down to 1×10^{-11} Torr. By choosing appropriate isotopes to measure and by turning off the 'over pressure' protection the RGA can be effectively run for the range from 1×10^{-4} Torr down to 1×10^{-11} Torr. When active, the 'over pressure' protection shuts the electron multiplier off if the pressure exceeds 1×10^{-6} Torr.

For instance, the partial pressure of argon in the spectrometer during an experiment was typically around 1×10^{-5} Torr. This is two orders of magnitude higher than can be measured with the electron multiplier, so rather than monitoring the partial pressure of the major isotope of argon at $m/z = 40$, instead the partial pressure at $m/z = 38$, another isotope of argon, is measured. Argon-38 is found at ratios of 1:1470 with argon-40 so a typical partial pressure of $m/z = 38$ would be 7×10^{-9} Torr. A typical partial pressure

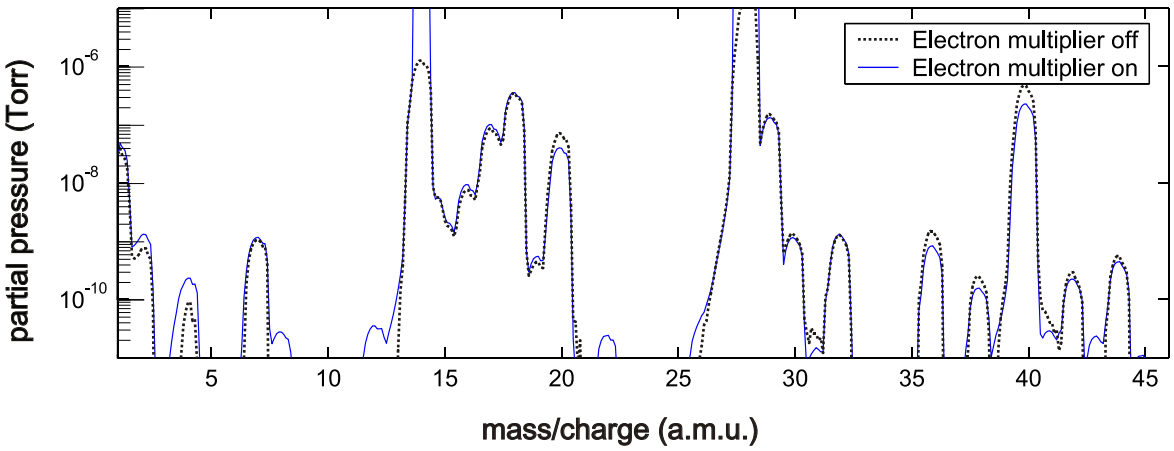

Figure 4.2: Analog scans with and without the electron multiplier. While the electron multiplier cuts out above 1×10^{-6} Torr, the scan using just the ion detector cannot detect pressures lower than 1×10^{-9} Torr.

of m/z = 44, corresponding to the product carbon dioxide, would be 2×10^{-10} Torr.

RGA software

The RGA is controlled by a program in Labview format on a PC running Windows 95. The program has several different modes for gathering and displaying data. The two used most frequently were the analogue mode and the 'PvT' (Pressure versus Time) mode. The analogue mode scans over a specified mass/charge range. The speed of the scan depends on the total range, the resolution and the dwell time. The longer the dwell time, the more accurate the scan. A typical scan would have a resolution of 0.1 a.m.u. and a dwell time of 50 ms. The mass spectrometer is calibrated and tuned to produce smooth peaks, 1 a.m.u. wide at 10% of the peak height and 0.4 a.m.u. wide at 95% of the peak height. The peaks are centred on integer a.m.u. values.

In the PvT mode, the partial pressure transducer scans each selected mass for a user defined dwell time (default 10 ms). The partial pressures for each mass are plotted as a function of time. The time intervals between measurements depend on the number of different m/z ratios being scanned and on the dwell time of each. The shorter the dwell time, the smaller the interval between measurements but the worse the signal to noise ratio. This mode depends on accurate tuning of the RGA since if the peaks are

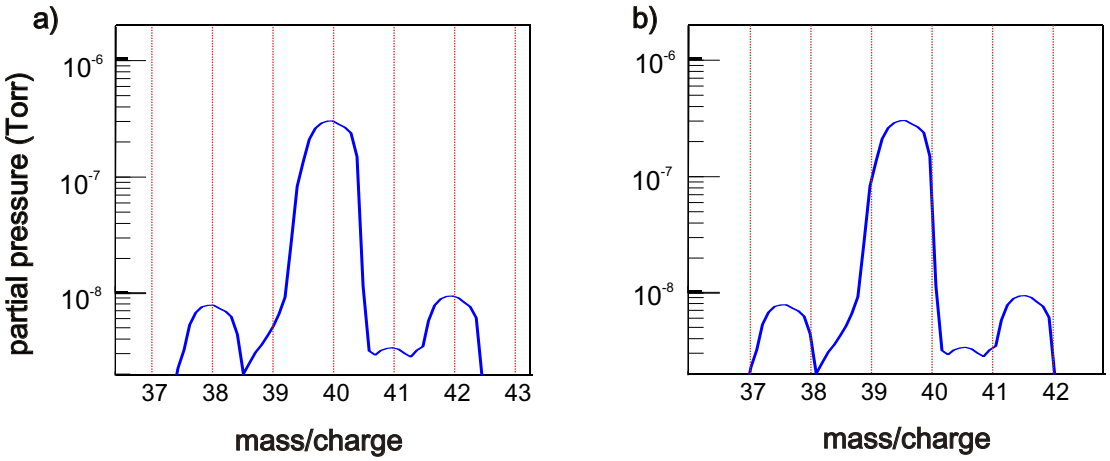

Figure 4.3: (a) Spectrum of a well-tuned RGA. The peaks are centred on integer m/z values. (b) A spectrum from a badly tuned RGA. The peaks are not centred on integer mass to charge values, so the reported partial pressures will be considerably lower than the actual partial pressures.

not centred on the integer m/z values the value displayed and recorded will be on the shoulder of the peak (Figure 4.3). The PvT mode only scans integer m/z ratios. Since the intensity of the peaks drops off sharply, small shifts in the centering of the peaks will result in large fluctuations in the measured partial pressure, generating periodic oscillations in the PvT scan.

It is possible to tune the RGA with gases with known mass spectra. The recommended gases are a combination of helium, nitrogen and krypton. In this case, the RGA was tuned with argon and krypton. The tuning mode is similar to the analogue mode. Extra parameters enable the adjustment of the peak width and the scale factor, both of which control the centering of the peak.

4.1.2 Experimental set-up and procedure

The experimental set-up was similar to that described for the general experiment (Section 2.2), but with an extra gas line to admit CO into the chamber and with the residual gas analyser (RGA, see Section 4.1.1) connected via a copper pipe downstream of the chamber and gas filter. A valve was fitted to control the pressure into the RGA (Figure 4.4). The RGA invariably had high background signals due to CO_2, of the order of 40 parts per million (ppm). These could be minimised by continuously pumping on the

RGA and the inlet tube during the entire period when the RGA was in use, as well as by heating the inlet tube with a heat gun and by degassing the RGA. The RGA has a 'degas' function that increases the electron emission to speed up the ionisation and removal of any gas present in the RGA.

Argon was used as the carrier gas for all inline mass spectrometry experiments. Argon is a commonly available gas with a mass spectrum that does not interfere with the measurement of the gaseous reactants and products of Reaction (4.1) or of the analogous reaction of hydroxyl radical with cyclohexane. Carbon monoxide was admitted to the chamber via a port on the nebuliser.

The dielectric narrow band filter was omitted from the optical path because it reduced the total irradiance to such low levels that no products from the radical scavenger reaction (4.1) were observed. The upstream glass impactor (nozzle diameter 4 mm ID) was present in all experiments unless otherwise noted. This limited the range of aerosol particle diameters and ensured the removal of any oversize particles from the aerosol stream before it entered the chamber. Downstream, the 1 mm ID nozzle was used to prevent any aerosol from entering the mass spectrometer. A Balston particle filter backed up the impactor.

Calibration with carbon dioxide

The RGA mass spectrometer was calibrated with known flows of carbon dioxide to establish the response factor (RF) of the spectrometer. The response factor relates the intensity of a peak at a particular mass to charge ratio to the partial pressure of the corresponding gas. The partial pressures of ions corresponding to mass to charge ratios (m/z) of 28, 32, 36, 40, and 44 were monitored. An m/z ratio of 36 corresponds to an isotope of argon which was present in convenient levels for comparison with m/z = 44, which corresponds to carbon dioxide. The ratio of the partial pressures of these species was plotted against the known flows of carbon dioxide to obtain a calibration curve.

The response factor for carbon dioxide was calculated to be 0.2716 with respect to argon-36, meaning that the fraction of carbon dioxide detected, as ratioed against the argon-36 partial pressure, was 27.16% of the actual relative partial pressure of carbon dioxide.

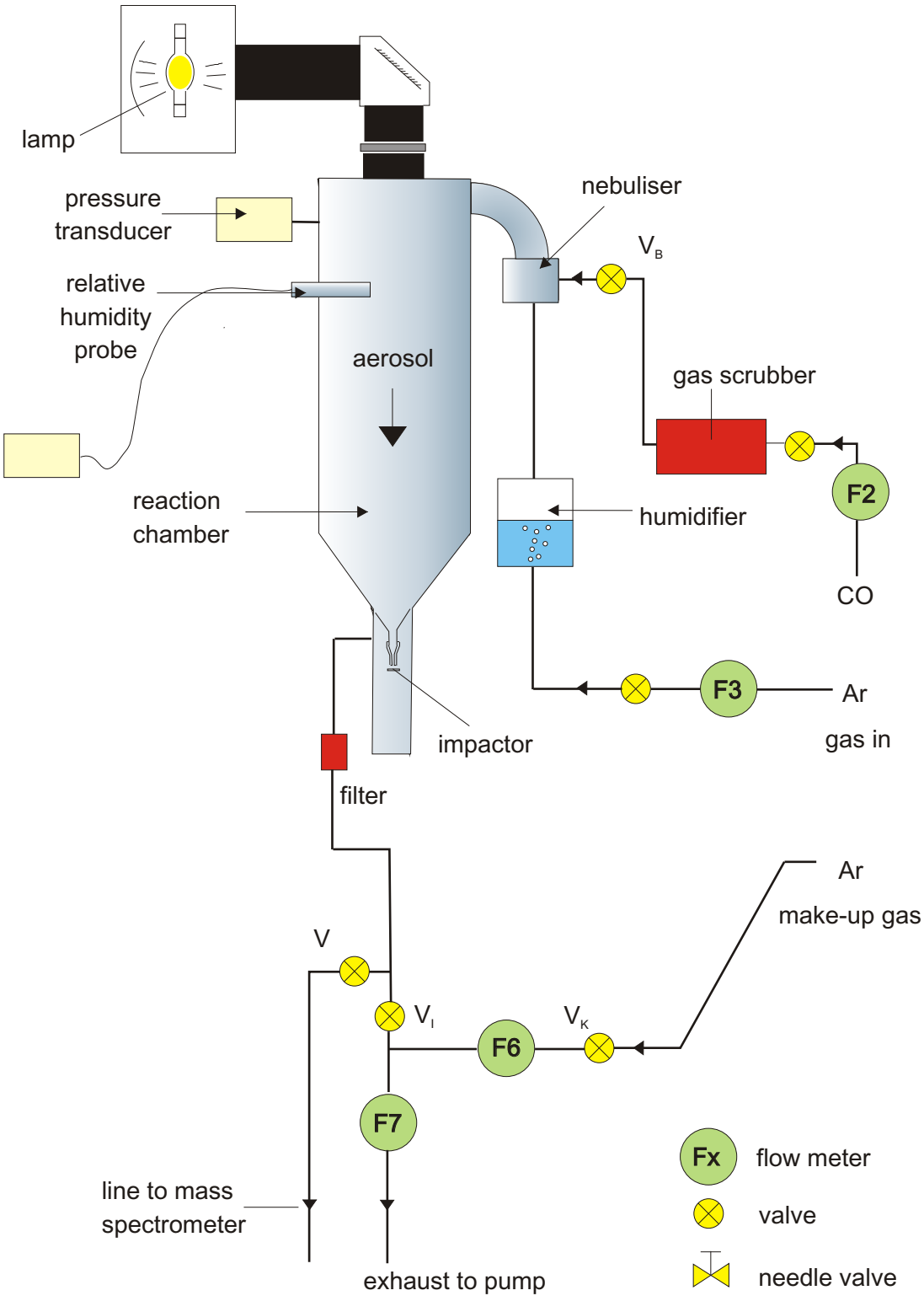

Figure 4.4: Schematic of inline gas phase system

The major isotope of argon is argon-40. The next most common isotopes of argon are argon-36 and argon-38, which occur naturally at percentages of 0.337 and 0.063 respectively, of the total argon . Both isotopes were used to measure the relative partial pressure of argon when the intensity of the peak at m/z = 40 was off scale. Argon-36 was primarily used when cyclohexane was the radical scavenger (Section 4.2) while argon-38 was used with carbon monoxide.

Experimental procedure

For each measurement, the chamber was assembled and tested for leaks. Leak testing was a standard procedure, which involved measuring the time taken for the pressure to rise 1 Torr with valve V_I closed at a pressure of around 600 Torr. The reservoir was then filled with solution and the argon flow turned on, along with the pump. The pressure was adjusted via a make-up flow of argon, controlled manually at V_K. The chamber pressure, as measured by the MKS pressure transducer, was kept at about 10 Torr below atmospheric pressure. Figures 4.4 and 4.5 display the chamber set-up and the connection to the RGA respectively.

Initially, V_M, on the inlet to the RGA, was turned until it was only just open. V_γ was then opened until the total pressure in the PPT was around 1.5×10^{-5} Torr. The pressure could be adjusted further by adjusting V_O, the valve between the RGA manifold and the turbo pump, and V_N, the needle valve between the PPT and the manifold. For these experiments, the partial pressures of ions corresponding to mass to charge ratios of 14, 18, 28, 32, 38 and 44 were monitored.

Once the pressures had stabilised, the carbon monoxide flow was turned on, followed by the lamp (with the shutter closed). The lamp required ten minutes to warm up, during which time the flows of carbon monoxide and argon stabilised (as measured by the RGA) and the chamber was purged of air. After these ten minutes of warm up time, provided the pressure was stable and 10 Torr below atmospheric pressure, the lithium nitrate or sodium nitrate solution was admitted into the nebuliser. The pressure often needed adjustment at this point.

Twenty minutes later, the shutter was opened for ten minutes of irradiation. After this time had elapsed, the shutter was closed and the system was left for a further ten minutes. The lamp was then turned off and the carbon monoxide shut off: at the

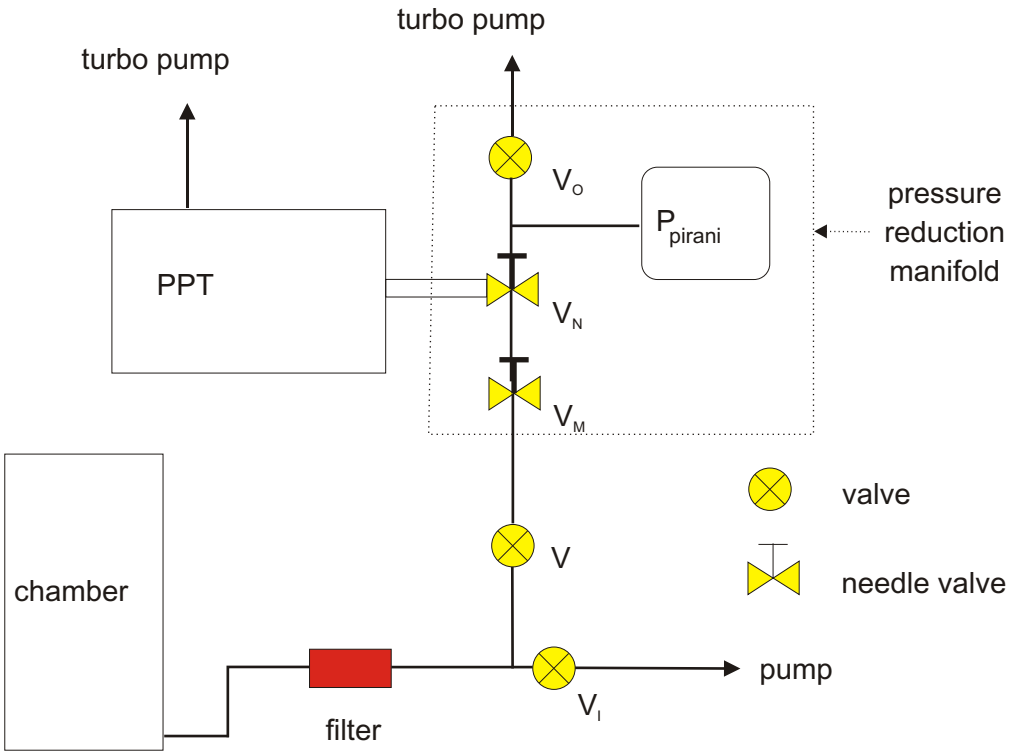

Figure 4.5: Schematic of inline connection between the RGA manifold and the system.

mass flow controller, at the cylinder and at V_B, the valve immediately upstream of the chamber. The chamber was then purged of carbon monoxide; the decrease in carbon monoxide was able to be monitored by the partial pressure of ions corresponding to a mass to charge ratio (m/z) of 28. The ratio m/z = 28 also corresponds to nitrogen but in this case, after a couple of minutes of purging, there should have been none of either nitrogen or carbon monoxide in the chamber. The ratio m/z = 14 was also able to be used as a crude indication of the relative amounts of nitrogen and carbon monoxide. The ratio of N_2^+ to N^+ (or N_2^{2+}) detected was about 10:1, while the ratio of CO^+ to CO^{2+} was about 100:1. Air leaks could be detected by the presence of oxygen, at m/z = 32. The ten minute periods before and after the irradiation period were used to construct a baseline.

Figure 4.6 depicts a typical pressure versus time scan. For most of the scan, the partial pressures of all the m/z ratios of interest are more or less constant. The rise in the partial pressure of m/z = 44 is too small to be resolved at this scale. The partial pressure of oxygen (m/z = 32) drops throughout the experiment, except for a small spike when the nitrate solution is introduced to the nebuliser at 2500 s. The partial pressures corresponding to carbon monoxide, with m/z ratios of 14 and 28, can be seen to drop exponentially after 4800 s when the flow of carbon monoxide was turned off. Also noteworthy is the fact that the partial pressure of argon-38 remains very constant throughout the entire experiment.

Instead of shutting the system down after the second baseline measurement, a second irradiation was often performed. This also lasted for ten minutes and was followed by a further ten minute baseline measurement. Repeat measurements such as this helped conserve carbon monoxide, but suffered from more frequent blockages.

Carbon monoxide purity

During initial inline measurements using carbon monoxide as the radical scavenger, it was noticed that the carbon dioxide levels rose when carbon monoxide was introduced into the chamber. The carbon monoxide was subsequently tested for carbon dioxide contamination and found to be contaminated with levels of carbon dioxide at around 375 ppm. This proved to be far in excess of the amount of carbon dioxide produced in the gas phase reaction of carbon monoxide with hydroxyl radical.

Research grade carbon monoxide, certified to have carbon dioxide levels of 15 ppm, was ordered. However, the supplier could not freight the carbon monoxide to New Zealand, either by plane or by sea. Instead, some ultra high purity (UHP) grade carbon monoxide was ordered from a local supplier. When analysed with the RGA, the carbon dioxide concentration was found to be at a level of 40 ppm. A gas scrubber consisting of potassium hydroxide pellets in a metal cylinder was added to the line to remove carbon dioxide from the carbon monoxide. The scrubbing reaction is:

$$CO_2 + 2KOH \rightarrow K_2CO_3 + H_2O \tag{4.2}$$

With the gas scrubber, carbon dioxide levels of 21 ppm were achieved. Since the carbon monoxide was only a fraction (2%) of the total flow, the contribution of this contamination to the background CO_2 levels was very small.

Earlier experiments used carbon monoxide flow rates of 500 sccm, or 11% of the total flow. Later experiments[3] used flow rates of 100 sccm, 2% of the total flow, in order to conserve carbon monoxide. The contamination of carbon monoxide by carbon dioxide was obvious in the early experiments with the higher flow of carbon monoxide, but at very low relative levels in the later experiments. The background at m/z = 44 appeared to be mainly from within the spectrometer itself, and not due to leaks from the atmosphere. The partial pressure of m/z = 32, corresponding to oxygen, was used to monitor leaks into the system. Oxygen concentrations as detected by the RGA were typically around 16 ppm. At these levels, the contribution of atmospheric carbon dioxide to the background is negligible.

4.1.3 Composition of aerosols studied

Atmospheric nitrate aerosol typically consists of sodium and magnesium nitrate if it is formed from sea salt aerosols, or calcium nitrate if it is formed from mineral dust (see Section 1.2). The experiments described in this work investigated sodium nitrate and lithium nitrate aerosol.

Other solutions investigated were sodium chloride and mixtures of lithium nitrate and sodium chloride. Sodium chloride was used as a control, since it was not expected to generate any hydroxyl radical. Mixtures of the two salts had potential to affect the ratio

[3]This includes all of the experiments that contributed to the data reported later in this thesis.

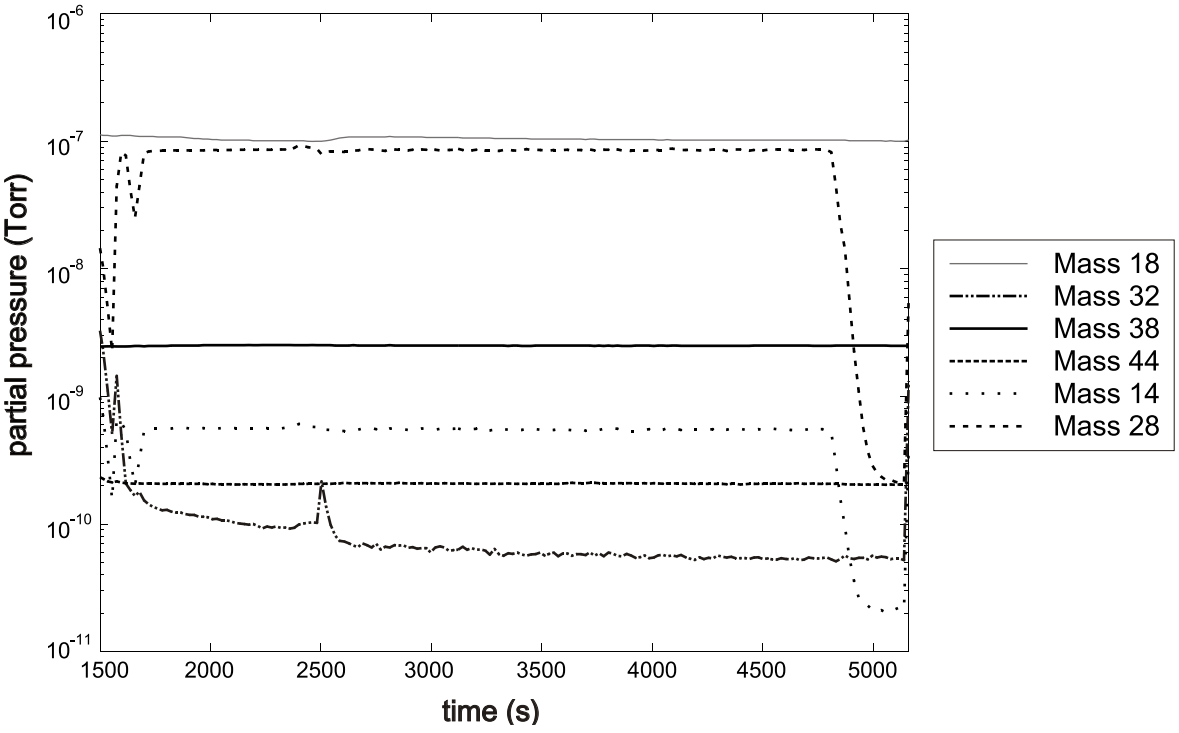

Figure 4.6: Typical pressure versus time scan as measured with the RGA.

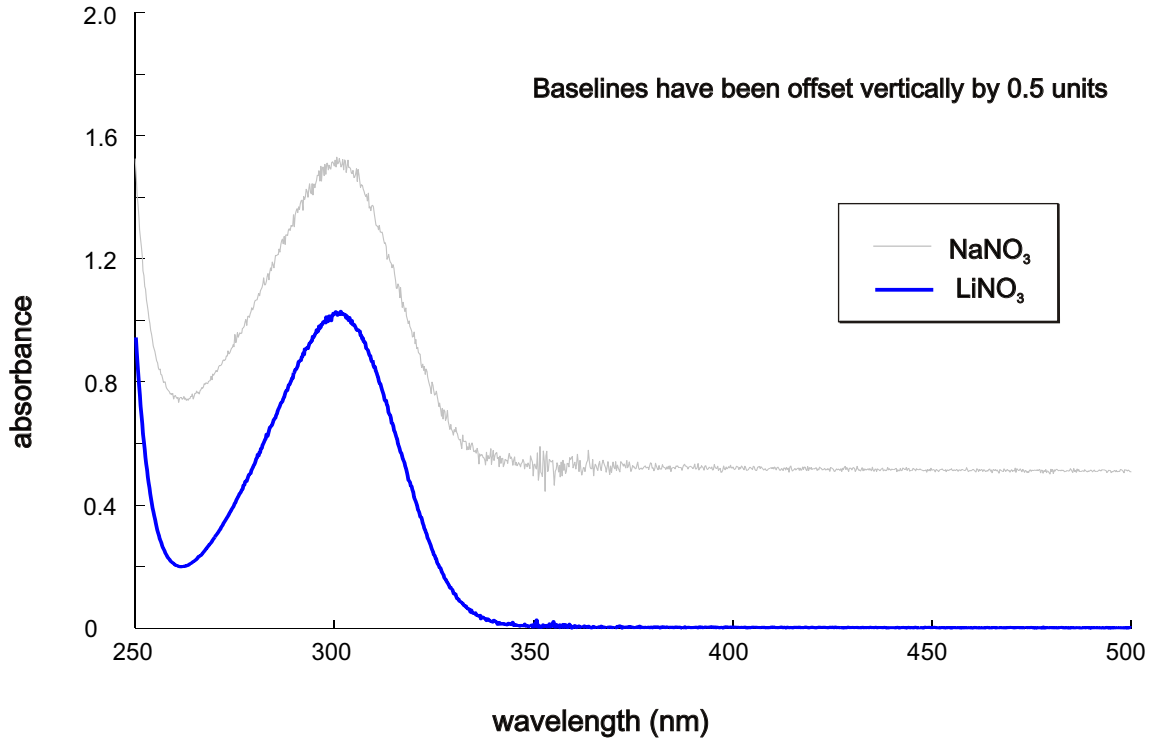

Figure 4.7: A comparison of ultraviolet/visible absorption spectra of lithium nitrate and sodium nitrate, both at concentrations of 0.14 mol L^{-1}.

of bulk to gas phase production of hydroxyl radical, since the distribution of nitrate in the droplet may have been affected.

Lithium nitrate ($LiNO_3$) was used for the majority of the gas phase experiments as it is more soluble than sodium nitrate ($NaNO_3$) and hence aerosols with a higher concentration of nitrate can be nebulised and collected without blockages at the impactor. Given the low yield of hydroxyl radical, it was necessary to have very concentrated solutions of nitrate in order to be able to measure any rise in products. Lithium nitrate and sodium nitrate were found to have virtually identical absorption spectra in the ultraviolet-visible region, at least at low concentrations (see Figure 4.7).

Experiments with sodium chloride aerosol

In order to ensure that the change in partial pressure of carbon dioxide was genuinely caused by hydroxyl radical from the irradiated aerosol, and not simply an artefact

caused by heat from the lamp, for example, the experiment was repeated with sodium chloride (NaCl) replacing the lithium nitrate. While sodium chloride has been shown to produce interesting multiphase chemistry in the presence of hydroxyl radical [103], there is no mechanism for the production of hydroxyl radical in the absence of nitrate ions. The experiment was conducted as for the lithium nitrate gas phase experiments. The concentration of sodium chloride used was $1.9\,\mathrm{mol\,L^{-1}}$, this being the most concentrated solution that would not block the system. No production of carbon dioxide was observed.

Recent Molecular Dynamics (MD) modelling calculations have suggested that the nitrate anion concentration tends to be reduced at the surface of a droplet [53]. This would reduce any potential enhancement in hydroxyl radical diffusion yield in the droplet, since the nitrate anions would be surrounded by a solvent cage. However, the situation is different in the presence of sodium chloride, where the nitrate ion concentration is slightly enhanced at the surface [54]. In order to test whether this effect might increase the measured gas phase yield of hydroxyl radicals, mixed solutions comprising of $2\,\mathrm{mol\,L^{-1}}$ lithium nitrate and $2\,\mathrm{mol\,L^{-1}}$ sodium chloride were made up and nebulised as for the one component solutions. No difference in carbon dioxide production was observed.

4.1.4 Analysis and calculations

Analysis of partial pressure data

The RGA software permits data from pressure versus time scans to be saved as comma delimited text files. These files were then analysed with software such as Microsoft Excel spreadsheet or Matlab [86, 104]. Most of the analysis was performed with Excel but plots were formatted with Matlab. From the raw partial pressure data, a quadratic baseline[4] was fitted to the partial pressure of ions at a mass to charge ratio of 44 a.m.u. (corresponding to carbon dioxide) for the periods during which the shutter was closed (see Figure 4.8)[5]. The partial pressures took two minutes to equilibrate after each opening or closing of the shutter; these periods were not used for either constructing the baseline or measuring the rise in carbon dioxide. The baseline was subtracted from the

[4]A quadratic fit for the baseline was chosen since the baseline had a significant curve. A quadratic function appeared visually to be the best fit.

[5]The labels used in Figure 4.8 are denoted 'lamp on' and 'lamp off' for emphasis. In reality the lamp was on continuously and the shutter was opened and closed.

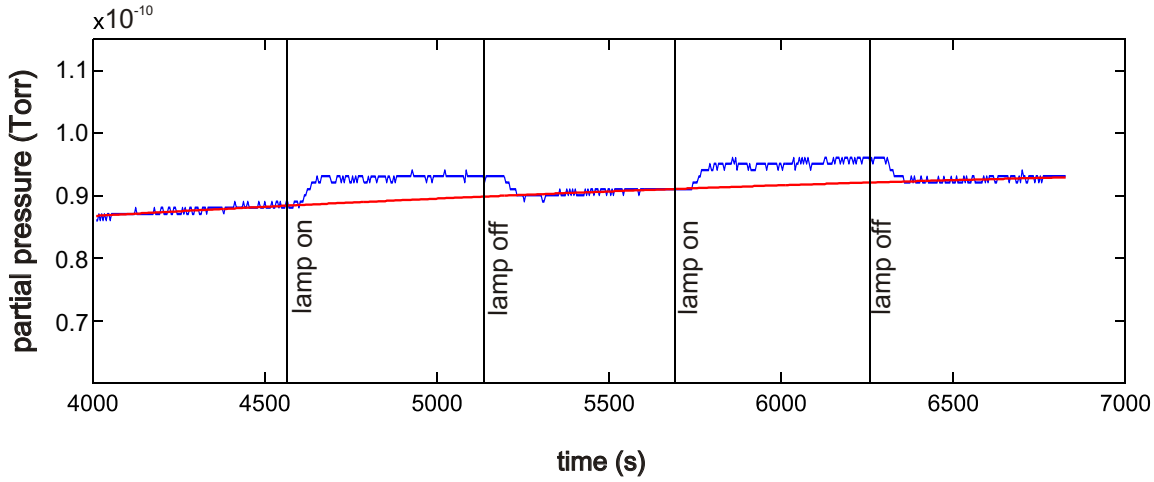

Figure 4.8: Partial pressure for m/z = 44 with fitted baseline. The aerosol used was 5 mol L^{-1} $LiNO_3$

.

partial pressure, leaving the difference as the rise in carbon dioxide pressure. The relative rise in carbon dioxide with respect to the partial pressure of argon for the periods where the shutter was open was converted into a mixing ratio in ppm. The total pressure in the mass spectrometer was controlled via valves on the inlet manifold. Since the total pressure was arbitrary, the ratios of the partial pressures are the crucial values. From these ratios and the known flow rates into the chamber, the absolute partial pressures of the various components were calculated.

A discrepancy between the total pressure and the sum of the partial pressures was noted throughout the entire project. The total pressure appeared to be a more accurate measure, since it responded predictably to changes in pressure in the inlet manifold of the RGA. The partial pressures did not always respond predictably to such pressure changes, although their ratios were consistent with the ratios of flow rates of the corresponding gases into the chamber. The total pressure is stated with a precision of only two significant figures, presumably because of the variation in ionisation cross sections from gas to gas, so it is not a precise measure in comparison with the measured partial pressures, which are measured to three significant figures.

It was noticed that sudden changes in the total pressure corresponded to sudden changes in the m/z = 44 pressure. It was not possible to construct a baseline across such a jump, but it was possible to construct a baseline up to the jump. The rise calculated from such

constructions corresponded very well to rises calculated from scans with no changes in total pressure.

Each rise in the carbon dioxide levels, as the nitrate aerosol was irradiated, generated between 80 and 100 data points. The number of data points depended on the sampling rate, which in turn depended on the sum of the dwell times for the m/z ratios monitored (see Section 4.1.1). These data, once the background carbon dioxide levels had been subtracted and the data ratioed to the argon-38 pressure, were averaged to produce the mean rise for that period of irradiation. A standard deviation was also computed for each period.

Calculations of total hydroxyl radical produced

It was assumed that all of the hydroxyl radical reacted with carbon monoxide to form carbon dioxide, so the concentration of carbon dioxide would correspond to the total amount of hydroxyl radical produced over the period of irradiation, that is, the 40 s the aerosol took to move down the chamber.

The reaction:

$$\mathrm{CO} + \mathrm{OH} \rightarrow \mathrm{CO_2} + \mathrm{H}, \tag{4.3}$$

obeys the rate law:

$$\frac{d\,[\mathrm{CO_2}]}{dt} = k_{4.3}[\mathrm{CO}][\mathrm{OH}]. \tag{4.4}$$

The rate constant for this reaction ($k_{4.3}$) and those for many other atmospherically important reactions have been compiled by Atkinson *et al.* [105]. The characteristic time of reaction, $\tau_{reaction}$, is essentially the lifetime of hydroxyl radical in the droplet, assuming the product $k_{4.3}[\mathrm{CO}]$ is large in relation to the characteristic time of diffusion ($\tau_{diffusion}$). The characteristic time of reaction is:

$$\tau_{reaction} = \frac{1}{k_{4.3}[\mathrm{CO}]}. \tag{4.5}$$

From Equation (1.31), Section 1.6.2, we have an estimate of the characteristic time for diffusion to the surface:

$$\tau_{diffusion} = \frac{d_p^2}{\pi^2 D_g}, \tag{4.6}$$

for a gas with a diffusion coefficient of D_g diffusing towards the surface of a droplet of diameter d_p. If $\tau_{diffusion}$ is of the same magnitude as $\tau_{reaction}$, approximately equal amounts of the reacting species will react and leave the droplet.

The rate constant $k_{4.3}$ is dependent on pressure and temperature. Atkinson *et al.* [105] recommend a value of:

$$k_{4.3} = 1.44 \times 10^{13} \left(1 + \frac{[\mathrm{N_2}]}{4.2 \times 10^{19}} \mathrm{molecule\,cm^{-3}}\right) \mathrm{cm^3\,molecule^{-1}\,s^{-1}}, \tag{4.7}$$

over the temperature range of 200 to 300 K and the pressure range of 0 to 1 bar of N_2. $k_{4.3}$ is in units of s^{-1}. Argon, not nitrogen, was used as the carrier gas for all the gas phase experiments reported here, but a comparison of the various measured rate constants tabulated by Atkinson *et al.* show little variation between the two gases. Temperatures and pressures measured during the experiments were used to calculate [Ar] in units of molecule cm^{-3}. These temperatures and pressures varied between 298 and 301 K and 745 and 768 Torr respectively. This variation does not affect the results significantly, but this calculation was nonetheless carried out for each experiment.

From the ratio of m/z = 44 to m/z = 38, corresponding to the ratio of CO_2 to argon-38, the concentration of CO_2 in units of molecule cm^{-3} could be obtained as shown in Equations (4.9) to (4.11), taking into account the ratio of argon-38 to total argon and the ratio of argon to total gas in the chamber.

$$C_{total} = \frac{n}{V} = \frac{P}{RT}, \tag{4.8}$$

$$C_{total}\,(\mathrm{molecule\,cm^{-3}}) = 101.3\,(\mathrm{kPa}) \times \frac{P_{chamber}\,(\mathrm{Torr})}{760\,(\mathrm{Torr})} \frac{10^{-6}\,(\mathrm{m^3})}{8.314\,(\mathrm{J\,mol^{-1}\,K^{-1}}) \times T(\mathrm{K})} N_A, \tag{4.9}$$

$$[\mathrm{CO}] = C_{total} \frac{F_{CO}}{F_{CO} + F_{Ar}}, \tag{4.10}$$

$$[\mathrm{CO_2}] = C_{total} Q\, RF \frac{F_{Ar}}{F_{CO} + F_{Ar}} X, \tag{4.11}$$

where X is the naturally occurring ratio of argon-38 to total argon, Q is the measured (relative to m/z = 38) rise in partial pressure at m/z = 44 and RF is the response factor (see Section 4.1.2). These equations calculate the concentration of each species in units of molecules per cubic centimetre.

For each concentration and chemical species studied, the average of all the carbon dioxide yields was calculated. The uncertainty in each calculated mean was computed by means

of Student's t test, that is,

$$error = \frac{\sigma t}{\sqrt{N}} \tag{4.12}$$

where t is the value from the Student's t table corresponding to 95% certainty and N - 1 degrees of freedom, where N is the number of samples. σ is the standard deviation for each set of measurements of carbon dioxide yield.

4.1.5 Wall effects

It was possible that the observed rise in concentration of carbon dioxide was due not only to photolysis of the nitrate in the aerosol droplets, but also in part due to photolysis of nitrate in a liquid layer on the walls of the reaction chamber. Although reactions on solid surfaces in the atmosphere are known to contribute to atmospheric chemistry with unusual heterogeneous chemistry [106], it was assumed that no surface-specific reactions were taking place.

A quantitative investigation of production of hydroxyl radical from the photolysis of nitrate on the walls of the chamber was carried out by shutting off the aerosol flow after 15 minutes, allowing the system to stabilise, then opening the shutter and irradiating the chamber.

It was difficult to investigate whether the photolysis of aqueous nitrate anions adsorbed to the surfaces of the chamber was contributing to the production of hydroxyl radicals, since it was not possible to measure this without disturbing the conditions in the chamber to some extent. The shutter would normally have been opened 20 minutes into the experiment for the first irradiation. Instead, the gas flow was shut off after 15 minutes then restarted, this time bypassing the nebuliser. Five minutes after this the shutter was opened.

An extra inlet into the chamber (via the carbon monoxide inlet) allowed the argon inlet to be switched so that it was not flowing through the nebuliser itself. Investigations with the Aerodynamic Particle Sizer showed that this was an effective way of stopping the aerosol. The argon flow was at the same rate ($4.4\,\mathrm{L\,min^{-1}}$) and was still humidified.

Of the three experiments run with this method, two showed no rise in the partial pressure of carbon dioxide when the shutter was opened. The third exhibited an ambiguous rise that may have been a random fluctuation in partial pressure; this rise was about 50%

of that expected for a nitrate aerosol. Visual inspections of the chamber showed that only the horizontal or near horizontal surfaces ever collected any significant amount of solution and then only in the absence of the upstream glass impactor.

The glass impactor (nozzle diameter 4 mm ID) was part of the standard system for the inline gas phase radical scavenger experiments. To test if it was having an effect on the measured rise in carbon dioxide levels, it was removed and the experiment was repeated without it. The relative rise in carbon dioxide levels was slightly higher (20%) than in experiments with the glass impactor in place. A considerable amount of solution was seen to collect on the cone at the bottom of the chamber in the absence of the glass upstream impactor. This could have been the major contributor to the measured slight increase, in which case the wall effects for experiments run with the upstream impactor in place were likely to be negligible.

4.1.6 Filter bandwidth

The maximum transmittance (at 310 nm) of the dielectric narrow band filter was 20%. It was hoped that there would still be sufficient irradiance to observe some products with the filter installed, but this was not the case. Without the filter, the dielectric mirror limited the bandwidth to between 260 and 330 nm. This covers the n to π^* band of nitrate.

4.2 Inline gas phase detection with cyclohexane as radical scavenger

Cyclohexane was trialled as a potential alternative to carbon monoxide as a gas phase scavenger for hydroxyl radical. It has several advantages over carbon monoxide: it is readily available, it is not present in the atmosphere, it is not toxic and it has no molecular mass coincidences with other chemicals used in the experiment. It has a similar solubility in water to carbon monoxide. Cyclohexane has been used previously to detect hydroxyl radical. Its rate of reaction with hydroxyl radical is well known [107] and it proved to have a convenient mass spectrum, with a gap at m/z = 36[6]. Unlike carbon dioxide, it is not an atmospheric contaminant, and there is no major

[6]The ratio m/z = 36 corresponds to an isotope of argon which can be used to measure the total pressure in the system relative to the cyclohexane peak at m/z = 84.

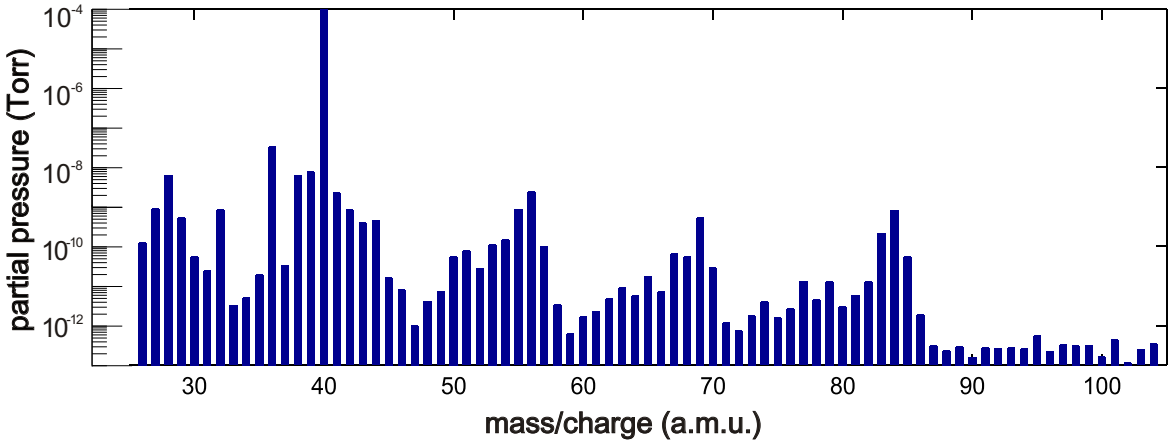

Figure 4.9: Mass spectrum of cyclohexane in argon. This figure was produced from analogue data, although the RGA does have a 'bar' mode which displays data in a similar manner.

atmospheric species with a peak at m/z = 84. This would be expected to increase the sensitivity of a system with cyclohexane as a radical scavenger. Figure 4.9 is a plot of the mass spectrum of cyclohexane in argon. The main disadvantage of cyclohexane was that it is a liquid at room temperature. The carrier gas, argon, was bubbled through it to saturate the argon with cyclohexane. At flow rates of between 1 and 10 sccm[7] of argon, an appreciable amount of cyclohexane could be admitted into the chamber. It proved difficult however to maintain a stable flow of cyclohexane into the chamber; the partial pressure as measured by the mass spectrometer fluctuated. The reason for the fluctuations was that the cyclohexane was encountering turbulence as it entered the chamber. This problem was solved by changing the cyclohexane inlet from a port into the chamber itself[8] to a port into the nebuliser. This port already existed, to allow equilibration of pressure between the top and bottom of the reservoir, so that the solution could drain out.

While moving the cyclohexane inlet to the nebuliser port removed the worst fluctuations in the flow, the change introduced a periodic dip in the cyclohexane partial pressure. This dip was due to the inlet tube becoming blocked with solution during the nebulisation of the solution. The flow through the inlet tube was low enough that the surface

[7] sccm: standard cubic centimetres per minute, that is, cubic centimetres per minute of N_2 at 273 K and one atmosphere.

[8] The 'upper' port for particle size distribution sampling.

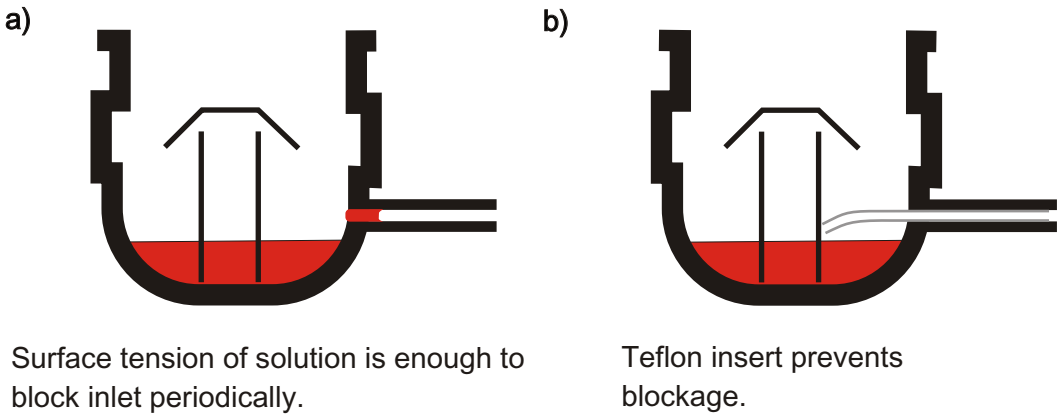

Figure 4.10: (a) Solution collects in the cyclohexane inlet as the solution is nebulised. (b)The Teflon tube prevented liquid collecting in the inlet.

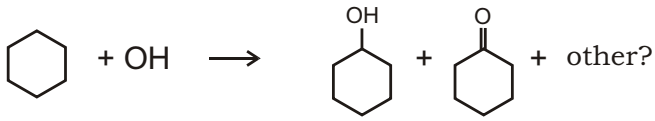

(4.13)

tension of the solution would be enough to contain the gas in the tube, until the pressure built up enough to remove the liquid. A thin Teflon tube inserted through the inlet tube solved the problem, since the aqueous solution would not collect on the Teflon and the flow would be unimpeded (Figure 4.10). Small random fluctuations persisted, however, and limited the sensitivity of cyclohexane detection.

Another major disadvantage of cyclohexane is that although its rates of reaction with hydroxyl radical are well known, the yields of the products are not. The radical reaction generates a great variety of products, including cyclohexanone and cyclohexanol (Equation (4.13)) [108]. Without knowing the yields, it is not possible to calculate the initial concentration of hydroxyl radical. Previous research using cyclohexane as the radical scavenger has measured the decrease in cyclohexane concentrations. The experiments using carbon monoxide as the radical scavenger, in comparison, had well established rate constants and the reaction yields could be quantified by measuring the rise in carbon dioxide concentrations.

4.2.1 Analysis

Analysis of the pressure versus time data for cyclohexane experiments involved a similar procedure to that described for the carbon monoxide experiments. No consistent or reproducible decrease in cyclohexane concentration was observed during irradiation of the aerosol. Analogue scans were conducted over a m/z range of 20 to 105 a.m.u., in the hope that products (cyclohexanol, cyclohexanone) might be observed. The parent peak of cyclohexanone would be found at m/z = 98 while the parent peak of cyclohexanol would be observed at m/z = 100. Within the limits of sensitivity of the RGA, neither of these products were observed. At higher mass/charge ratios, the RGA was able to measure partial pressures as low as 1×10^{-12} Torr. The peak with the highest mass to charge ratio detected was at m/z = 86, corresponding to an isotopologue of cyclohexane.

4.3 Offline gas phase detection with carbon monoxide as radical scavenger

As an alternative to detecting the hydroxyl radical yield via the production of carbon dioxide inline (while the aerosol was being irradiated), attempts were made to trap the carbon dioxide produced and measure it offline. The RGA was again used to measure the yield of carbon dioxide, but this time the measurement was of the pressure in a trap, after isolation, reheating and evaporation of the CO_2, rather than the partial pressure in a gas flow.

The system for measuring the gas phase production of hydroxyl radicals was similar to that used for the aqueous phase analysis (Figure 4.11). The solutions nebulised were $1\,\mathrm{mol\,L^{-1}}$ $NaNO_3$. The nebulising gas flowed at rates of $4.0\,\mathrm{L\,min^{-1}}$ N_2 and $0.5\,\mathrm{L\,min^{-1}}$ CO, the total flow still being $4.5\,\mathrm{L\,min^{-1}}$ as for the other gas phase scavenger experiments. As in previous experiments, the aerosol flowed out of the chamber via an impactor where the droplets were removed. It then passed through a cold trap (-65 °C, cooled by dry ice in ethanol) where the water vapour was removed from the gas stream. This was followed by a filter to remove any remaining aerosol. The gas passed through a second cold trap, cooled by liquid nitrogen. This collected the CO_2 but not the CO or N_2 in the gas stream. The collected (solid phase) CO_2 was isolated in the trap, then the trap was connected to the RGA. The trap was evacuated of gas by a diffusion pump while still immersed in liquid nitrogen, then isolated and warmed to room temperature. Once

the trap was at room temperature, the gas was bled into the spectrometer. Integrating the partial pressure signal over time resulted in a value that was proportional to the initial total pressure of CO_2 in the trap.

The relation of the partial pressure of CO_2 in the trap to the flow of CO_2 generated in the system was determined by calibrating the system with known flows of CO_2. This was admitted directly into the side of the chamber (via the alternate APS port). Admitting the CO_2 directly into the chamber avoided uptake of CO_2 in the gas humidifier or the solution of sodium nitrate in the nebuliser.

Once the total yield of carbon dioxide had been measured, the rate of production of carbon dioxide per cubic centimetre per second could be calculated and the hydroxyl radical yield obtained, as described for the inline gas phase system (Section 4.1.4).

The principal disadvantage of this method was that the RGA was being used to measure what was essentially a total pressure, rather than a partial pressure sampled from a gas flow, a purpose for which it was not designed. Although the spectrometer could distinguish between water vapour and carbon dioxide, both present in the trap, the partial pressures as displayed in the software program were only reliable as ratios to the partial pressures of the other species in the system. The pressures in the trap were also far beyond what the RGA could measure (the partial pressure transducer shut down automatically at 2×10^{-4} Torr) so the gas had to be bled very slowly into the system. Adjusting the flow during a measurement would have affected the total and partial pressures, so a bleed valve had to be opened a tiny amount and left unchanged for the entire set of experiments.

The temperature of the trap was also critical to the pressure measurement. The temperature of the water in the bath surrounding the trap was monitored via a thermometer. When the temperature of the water was constant (within the limits of accuracy of the thermometer, $\pm 0.1\,^{\circ}$C), the valve to the trap was opened to admit the contents of the trap into the RGA manifold via the bleed valve.

To minimise the amount of carbon dioxide collecting in the inlet tube, the tube was warmed to around 60 °C with heat tape. Clayborn electrical resistance heat tape consists of enamel-coated resistance wires sandwiched between two layers of adhesive-impregnated fibreglass dielectric insulator. The heat tape purchased (G-28 1/6" with one conducting wire) had a resistivity of 35.6 ohms per metre and a maximum power

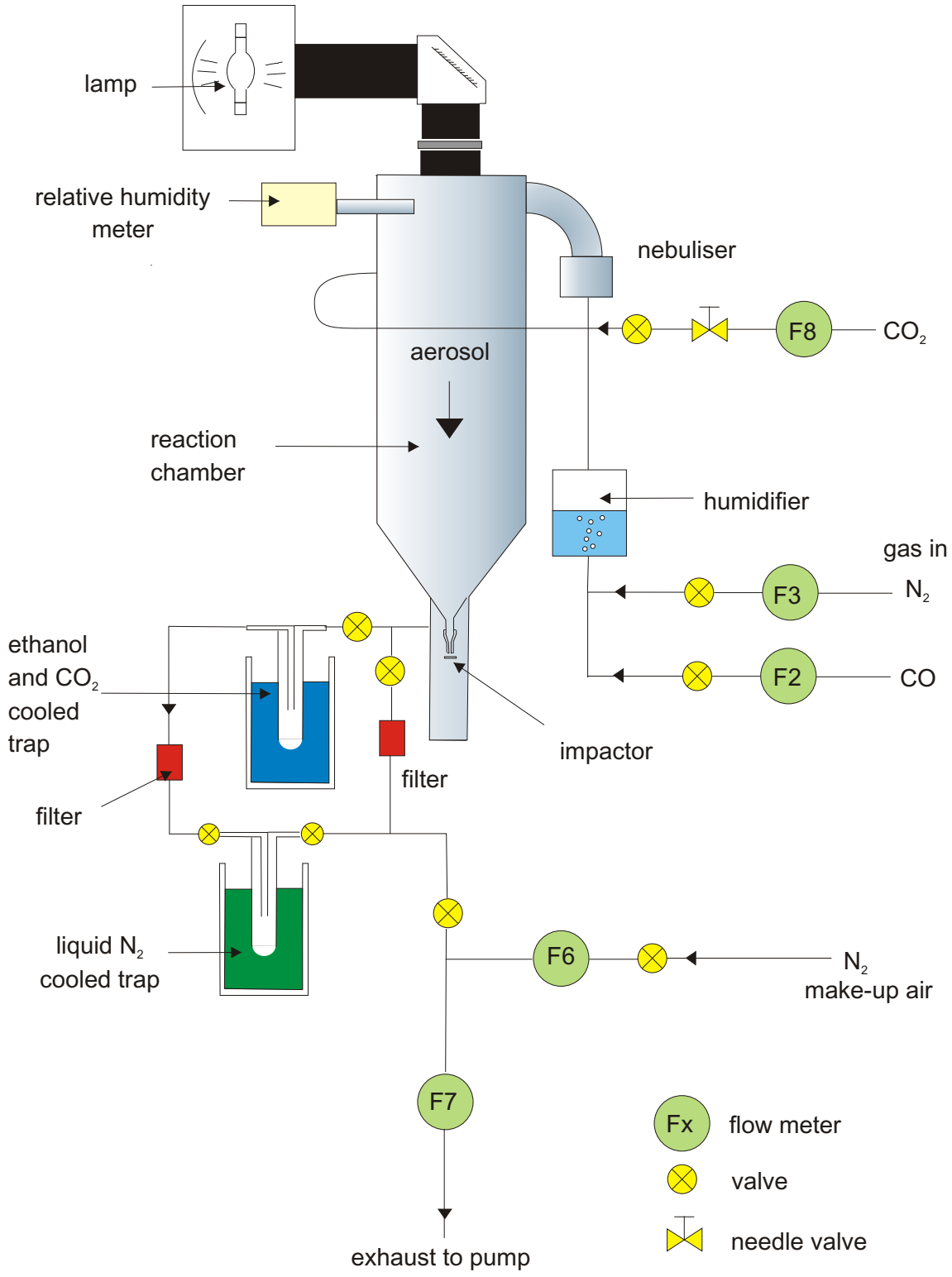

Figure 4.11: Schematic of the offline CO system.

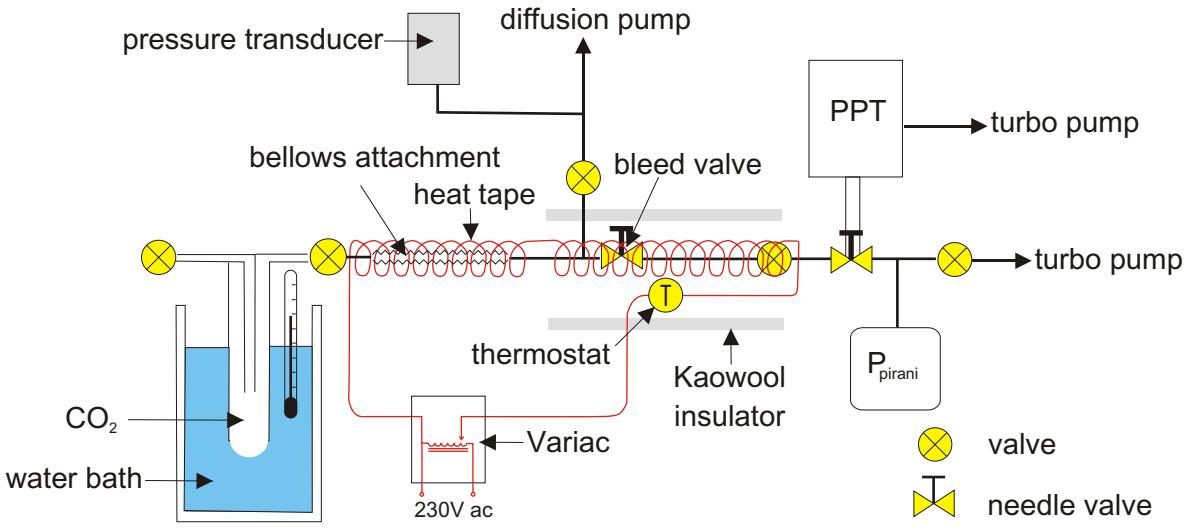

Figure 4.12: Schematic of the offline set-up for measurement of CO_2 pressure in the trap, once isolated.

dissipation of 66 watts per metre (at room temperature). The heat tape was wrapped around both the inlet tube and a thermostat. The thermostat was set to switch the heat tape off once the temperature reached 60 °C. The amount of power converted into heat by the tape was controlled by a Variac (variable ac supply). The system was insulated with heat proof tape and Kaowool, a thermal insulator made of glass alumino-silicate fibres.

The other major problem with the system was the tendency of water to freeze in the liquid nitrogen-cooled trap during the experiment, thus blocking the trap and ending the experiment. The water vapour present in the trap after it had been isolated, pumped down and thawed also complicated the measurement of the carbon dioxide pressure. Water ice would also block the first, dry ice cooled trap. This upstream trap was replaced with a larger one in an attempt to trap a greater fraction of the water before it reached the liquid nitrogen cooled trap and froze there. Copper baffles were added to the trap to increase the amount of surface available for the water to freeze on and to increase the conduction of heat away from the gas. This technique was reasonably successful. It was necessary to purge the system with dry nitrogen before the traps were cooled, to remove all carbon dioxide. These experiments were conducted before the shutter was added to the lamp optics, so a bypass system with a three way valve was constructed so the gas flow could be flowed through the traps for a specific time.

Since there was a delay for the gas to travel through the traps, it was necessary to purge the system with dry gas at the end. This ensured that all of the carbon dioxide in the line was pushed through to the final liquid nitrogen cooled trap.

All of these issues complicated the trapping and measurement of the carbon dioxide. The reproducibility of the results was never high. When it proved possible to detect increases in the partial pressure of carbon dioxide with the inline system, the experiments with the offline system were abandoned.

4.4 Benzene as a radical scavenger; offline analysis

Benzene has also been previously used as a radical scavenger. The advantage of benzene over cyclohexane is that the yields for the reaction of benzene with hydroxyl radical are well characterised, in aqueous solution at least [20, 97]. As a substitute for cyclohexane, benzene was not a good choice. The two compounds have markedly different solubilities in water and different reaction mechanisms with the hydroxyl radical. However, benzene is a relevant atmospheric pollutant and studying its aerosol phase reactions provided direct evidence of the potential for nitration of aromatic compounds in the atmosphere. Benzene reacts with the hydroxyl radical to produce phenol (Equation (4.14)).

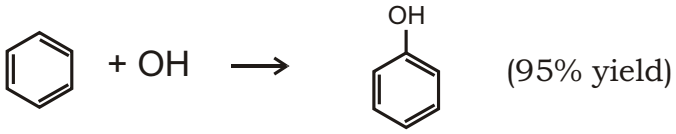

(4.14)

4.4.1 Attempts to trap gas phase phenol

Phenol has a low vapour pressure (0.35 Torr at 20 °C) and a high melting point (41°C) [109]. This should have made it relatively easy to collect in an ice/water cooled trap. Experiments were conducted to establish the reproducibility and detection limit of such a method.

Nitrogen was passed over phenol crystals then admitted directly into the chamber via the upper APS port. At a laboratory temperature of 20 °C, this should result in a phenol vapour/nitrogen mixture with a phenol concentration of 470 ppm. This mixed in the

chamber with the standard flow of $4.4\,\mathrm{L\,min^{-1}}$ of humidified nitrogen, which entered via the nebuliser. With the nitrogen/phenol mixture flowing at 21 sccm, this resulted in a mixing ratio of 2.2 ppm. The hydroxyl radical yield would be expected to be around 1 to 2 ppm, based on the carbon monoxide experiments.

After 60 minutes, the flows were shut off and the trap disconnected from the system. Isopropyl alcohol (IPA) was used to wash out the trap. The washings were made up to 25 mL in a volumetric flask with IPA. 100 μL volumes of this solution were analysed with the Shimadzu HPLC. Well-resolved peaks were seen at retention times of 15 minutes, with an absorption maximum of 270 nm. HPLC analysis of a sample of phenol in IPA confirmed that these peaks did correspond to phenol. Isopropyl alcohol produced no peaks in the region of interest.

The detection limit in parts per million was estimated by comparing the area under these well-resolved peaks with the area under peaks at the detection limit. The detection limit was estimated to be 0.2 ppm. This detection limit was a very rough estimate, since the peak areas were not reproducible between experiments. This lack of reproducibility gave the impetus to trial cyclohexanone in the trapping system instead.

4.4.2 Measurement of hydroxyl radical with trapped phenol

The phenol in the bubbler was replaced with benzene, and the bubbler was shifted to one of the ports on the nebuliser. Nitrogen was set to bubble through the benzene at 54 sccm. $5\,\mathrm{mol\,L^{-1}}$ $LiNO_3$ was nebulised and irradiated as in previous experiments, except that this time the humidified nitrogen flow was $4.05\,\mathrm{L\,min^{-1}}$ and oxygen was added to this flow (pre-humidifier) at $0.45\,\mathrm{L\,min^{-1}}$. Thus the total flow was $4.5\,\mathrm{L\,min^{-1}}$ and the nitrogen/oxygen ratio was 9:1. After 45 min of irradiation, the flows were turned off. The trap was washed out with IPA and the washings collected and diluted to 25 mL as for the phenol calibration experiments. The impacted aerosol at the bottom of the chamber was also collected for analysis.

The concentrations of phenol detected in the ice/water cooled trap were at the detection limit of the HPLC. The estimate of the detection limit corresponded to 0.2 ppm, so the experimental mixing ratio of phenol was around this level. Phenol was detected in measurable quantities, however, in the impacted aerosol. The Henry's law constant for phenol is 1.9×10^3 so it is considerably more soluble than benzene and much more soluble

than carbon dioxide. This explained why most of the product phenol was in the aqueous phase. The experiments continued, but concentrated on determining the concentrations of phenol in the aqueous aerosol phase.

Chapter 5

Experimental: Aqueous phase measurement of hydroxyl radical

Benzoic acid was used as a radical scavenger for hydroxyl radical produced from the photolysis of sodium nitrate. High Performance Liquid Chromatography (HPLC) was used for analysis of the irradiated samples, from bulk liquid solutions and impacted aerosol. The calculations of product concentration (Section 5.4) relied on an internal standard; it proved possible to use one of the reaction products as this standard. These concentrations are not directly useful for the calculation of quantum yields, which requires knowledge of the actual amounts of product collected. Section 5.5 explains the qualitative detection of products from experiments using benzene as the aqueous scavenger.

5.1 Nitrate/scavenger solutions as actinometers

As mentioned in Section 3.1.2, aqueous phase hydroxyl radical scavengers in combination with photolytic, OH-producing reactions have been proposed as actinometers. The photolysis of nitrate at 305 nm was one candidate. Hydrogen peroxide (H_2O_2) has also been used as a source of hydroxyl radicals, via irradiation with 254 nm light [110]. Many suitable aqueous phase radical scavengers have been described in the literature: benzene [111]; 2-propanol [93]; methanol and cyclopentane [17]; and thiocyanate (SCN^-) [112]. For this thesis, benzoic acid was chosen because it had been already been used to study the photolysis of nitrate and detailed methods for its analysis with High Performance Liquid Chromatography (HPLC) have been described elsewhere [4, 97].

Benzene was initially trialled as a gas phase radical scavenger, as described in Chapter 4. However, because of its fairly high solubility in water, it straddles the boundary between

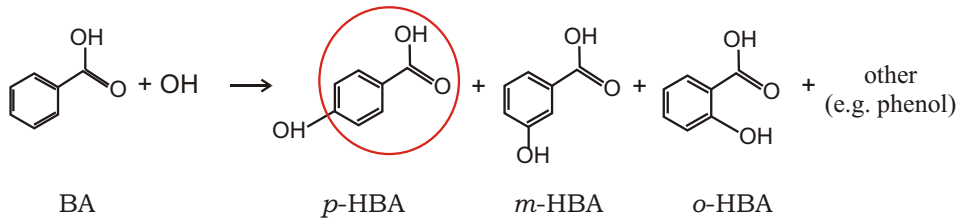

BA *p*-HBA *m*-HBA *o*-HBA (5.1)

a gas phase radical scavenger and an aqueous phase scavenger. The experiments using benzene also involved analysis by HPLC, so they are reported later in this chapter.

Benzoic acid reacted with the hydroxyl radicals as they formed in the aerosol droplets, forming *meta*-, *para*- and *ortho*-hydroxybenzoic acid (*m*-HBA, *p*-HBA and *o*-HBA respectively) (Equation (5.1)).

5.2 Method

Solutions of sodium nitrate, benzoic acid and sodium bicarbonate were nebulised in a similar manner to the potassium ferrioxalate solutions (Section 3.2). The sodium bicarbonate acted as a buffer, maintaining the pH at around 8. A sample of impacted aerosol was collected from the trap, diluted and then analysed with the Shimadzu HPLC system.

Bulk liquid experiments were run as for the bulk liquid actinometry. A Petri dish was filled to a depth of 1 cm with the nitrate/benzoic acid solution and placed halfway up the chamber. After ten minutes to allow the lamp to warm up, the bulk solution was irradiated for 30 minutes under a nitrogen atmosphere. It was then removed from the chamber and a sample was collected.

5.3 High Performance Liquid Chromatography (HPLC)

High Performance Liquid Chromatography was used to measure concentrations of organic products in liquid samples recovered from the impactor at the end of an experiment. Benzoic acid and *p*-hydroxybenzoic acid are strong UV absorbers, but since both were present along with nitrate in the samples, it was necessary to separate them and the nitrate before their concentrations could be measured. HPLC discriminates between

compounds based on their solubility. It is then possible to measure their concentrations separately via their UV absorbance.

Two HPLC instruments were used during the experiment. The system used for the majority of the experiment was a Shimadzu class VP system. When this system was not functioning the newer Dionex HPLC system was used instead. The instruments were similar in their operation and performance. The Shimadzu set-up was a little more difficult to run than the Dionex, but had the advantage that it was seldom used by other experimenters and the resolution was also slightly better.

5.3.1 HPLC theory

Chromatography in general involves a separation of chemical components by virtue of the differing physical properties of these components. There are many specific methods of compound separation. Typically chromatographic systems consist of a mobile phase and a stationary phase. The different physical properties of the two phases dictate how quickly various components will move through the stationary phase.

High Performance Liquid Chromatography involves a liquid mobile phase and a solid stationary phase. Typically, reversed-phase chromatography is used, since it is especially suited to aqueous solutions. Reversed-phase involves a non-polar stationary phase and a polar mobile phase. The stationary phase is usually hydrocarbon based. Non-polar compounds tend to adsorb to the non-polar stationary phase and hence take a longer time to move along the column than polar compounds, which tend to remain in the polar solvent. The polarity of the solvent can be altered during an analysis to influence the retention times [113]. The retention times also depend on the length and type of column used, and on the flow rates of the solvents. These will be constant for any particular system.

The stationary phase (hydrocarbon on silica) is packed into a column. The liquid phase (in this case a mixture of water and acetonitrile) is forced through this column at high pressure (typically 80 bar). Before the liquid phase enters the column, it will have been degassed and mixed to a predetermined concentration. Two minutes into a run, the sample is injected into the liquid flow.

Frequently the gradient of the solvent is ‘ramped’, decreasing the polarity over time

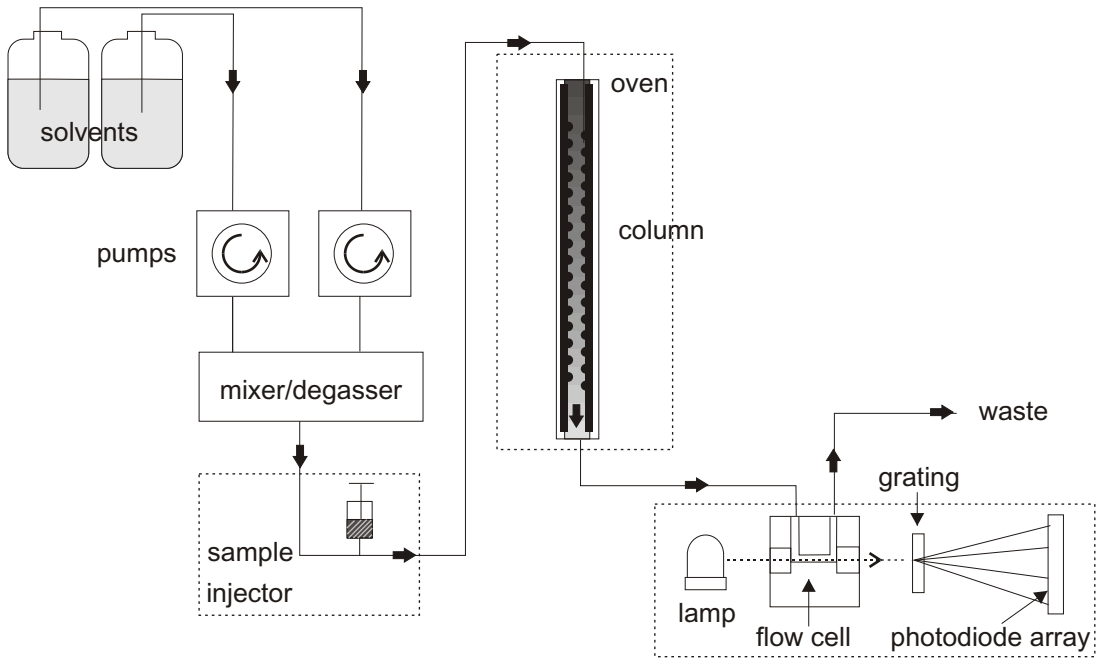

Figure 5.1: Schematic of the HPLC system.

and hastening the elution of the non-polar eluents. Otherwise, the gradient is said to be *isocratic*, with the solvent concentrations constant. Typical solvents are water, acetonitrile and methanol.

5.3.2 Shimadzu HPLC

The class VP Shimadzu system (Figure 5.1) includes a UV-visible photodiode array detector (SPD-M10Avp), a column oven (CTO-10Avp) and an injection unit (SIL-10ADvp). It is designed as a customisable system with exchangeable units. It has two pumps (LC10ADvp) and a degasser (DGU-14A).

Having flowed through the column, the liquid phase flowed through a cell with quartz windows. Light from a deuterium lamp (far UV) and a tungsten lamp (near UV) passed through the flow cell and onto the photodiode array detector (DAD). The signals generated by the DAD were converted into an absorption spectrum. The DAD has a resolution of 1.2 nm with a stated accuracy of ± 1 nm. The combined spectral range from the lamps is 190 to 800 nm. The sampling rate was one spectral measurement every 2 s. The flow cell has a path length of 1 cm and an internal volume of 10 μL.

For each analysis, 100 μL of sample was injected into an isocratic flow of 70% water and 30% acetonitrile. The column was a C18 Prodigy 5μ ODS3 100, 250 $\times$ 4.60 mm. The column was maintained at a temperature of 40 °C. After 7.2 minutes, a *p*-HBA peak was seen at 255 nm. The peak was usually well resolved. After all the species of interest had eluted, the gradient was made as non-polar as possible to remove any chemicals remaining on the column which had the effect of purging the column for the next analysis. A typical purge cycle would take 20 minutes, making each sample analysis take 40 minutes in total.

The pumps maintained a total flow rate of 1 mL min^{-1}, which resulted in a pressure of around 90 bar with mixtures of water and acetonitrile at a ratio of 70:30. The flow rate was measured to a precision of 0.3%. If the ratio was any higher than 70:30, the chromatograph showed an undulating baseline, with an amplitude of about 1 or 2 milli absorbance units, which was high enough to interfere with peak measurement. As long as the percentage of acetonitrile was higher than or equal to 30%, however, the undulations all but disappeared.

The Shimadzu HPLC computer interface was upgraded at the end of 2006. The Shimadzu instrument has since been controlled by the same computer that controls the Dionex HPLC. While the Shimadzu was offline due to the upgrade, the Dionex was used instead. The Dionex proved sufficiently sensitive to measure the bulk phase yields but not sensitive enough for the aerosol phase yields. Once the Shimadzu was back in operation, it was used for the analysis again. The process of finding and integrating the appropriate peaks became considerably simpler after the upgrade due to the different 'Chromeleon' software [114].

5.3.3 HPLC calibration

A stock solution of *para*-hydroxybenzoic acid (3×10^{-4} mol L^{-1}) was made up. A series of calibration standards with concentrations ranging from 1×10^{-7} mol L^{-1} to 8×10^{-6} mol L^{-1} was made up by adding aliquots of the *p*-HBA solution, on the order of 100 to 600 μL, to 25 mL volumetric flasks. Stock solution of sodium nitrate/benzoic acid (that is, the same solution used for the actual experiments) made up the rest of the volume of the flask. These solutions were then analysed with the HPLC using the method described above.

The Chromeleon HPLC software constructs a calibration curve from the standards and automatically generates a report with concentrations of identified species from selected peaks at specified wavelengths.

5.3.4 Detection of peaks

The low concentrations of products from the scavenger reaction resulted in absorbances at the limit of sensitivity of the diode array detector. This meant that it was often necessary to find and classify the peaks manually. The Chromeleon software [114] has a variety of methods for viewing the data. For a specific wavelength, plots of elution time versus absorbance enable measurement of peak area and hence concentration. Colour contour plots confirmed the presence or absence of *p*-HBA for each sample since it showed whether the suspected peak had a maximum at 255 nm and was not simply a shoulder of a peak of another eluent.

A typical HPLC chromatogram is shown in Figure 5.2. The chosen wavelength is 272 nm, corresponding to a maximum in the benzoic acid absorption spectrum. The Chromeleon software has (correctly) identified the peak at 9 minutes as *m*-HBA, although this is in fact a shoulder of the *m*-HBA peak, since *m*-HBA has a maximum at 298 nm. The peak from benzoic acid can be seen at 21.7 min[1]. The retention times varied slightly from run to run, but as long as the gradient program used was the same for each run, the retention times did not vary by more than about ± 0.2 min.

Figure 5.3 is a contour plot of absorbance. This type of plot makes it easy to identify the peaks of interest even when the relative concentrations are hugely different. The large peak at 9.2 min corresponds to *m*-HBA, while the smaller peak at 7.3 min corresponds to *p*-HBA.

5.3.5 Acidification of samples

HPLC analyses typically use acidified solvents. Otherwise, if the pH is fairly neutral, many organic acids are converted to the corresponding conjugate base. If the conjugate base has a different polarity to the acid, it has a different retention time. This complicates the chromatogram considerably; the heights of the peaks of interest change

[1] A peak due to nitrate can also be seen at 3.0 min, although at 272 nm this almost corresponds to a minimum of the nitrate absorption band.

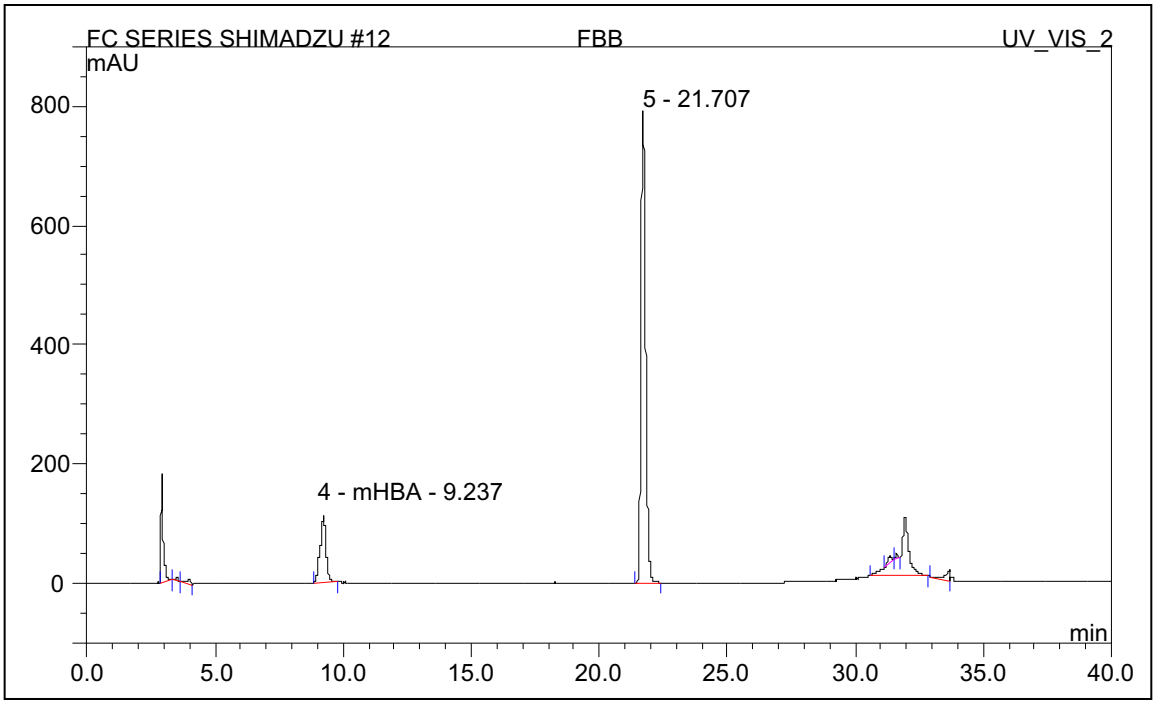

Figure 5.2: Example of a chromatograph produced by the Chromeleon software (non-irradiated bulk liquid sample, 0.1 mol L^{-1} $NaNO_3$, wavelength = 272 nm).

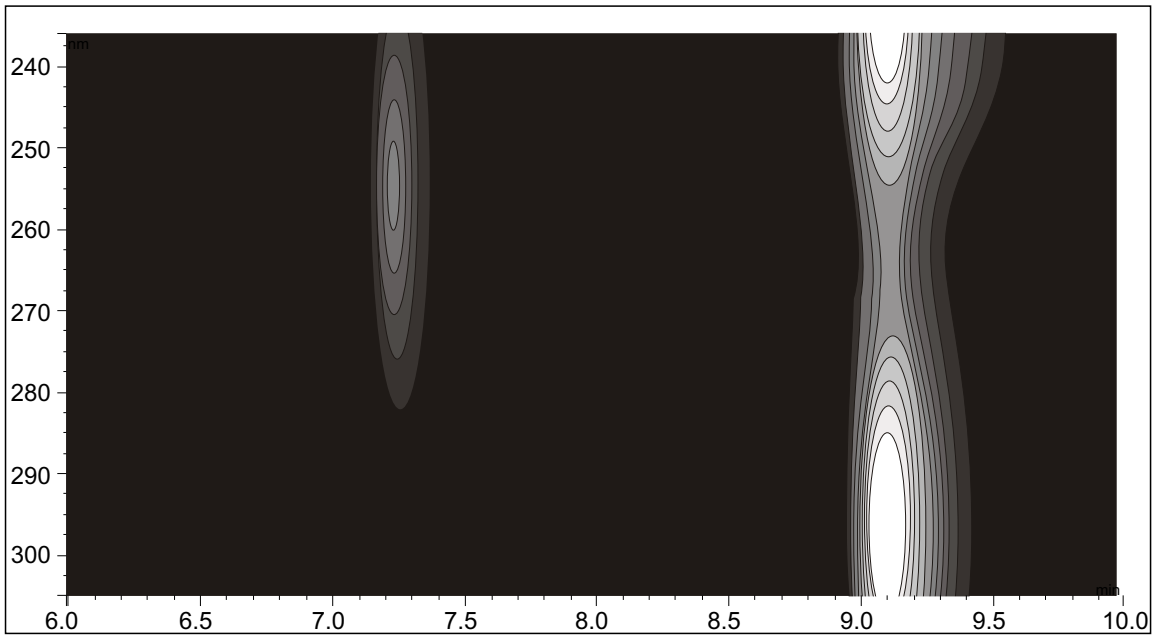

Figure 5.3: Contour plot of wavelength versus retention time from an HPLC chromatogram. Whiter regions signify higher absorbance. Irradiated, bulk liquid sample ($0.1\,\mathrm{mol\,L^{-1}}$ $LiNO_3$). The peaks are *p*-HBA and *m*-HBA, at 7.3 and 9.1 min respectively.

and the concentrations are no longer quantitative. Because the nitrate/benzoic acid solution was buffered with sodium bicarbonate, it was necessary to add dilute nitric acid ($0.05\,\mathrm{mol\,L^{-1}}$) to the samples before they were analysed by HPLC. Also, the water used as solvent was acidified with $0.05\,\mathrm{mol\,L^{-1}}$ of trifluoroacetic acid (TFA).

5.3.6 Internal standard

As for the experiments involving potassium ferrioxalate, the concentration of the impacted aerosol was not that of the original solution. Initially, attempts were made to measure the concentration of nitrate in the collected sample and from this calculate the concentration of *para*-hydroxybenzoic acid relative to the original concentration of nitrate. Samples were collected and measured via the GBC 920 UV-visible spectrometer in quartz cells of path length 0.2 cm. However, due to interference from the nitrite produced during the nitrate photolysis, this technique did not produce consistent results. This was clear from measurements on undiluted, irradiated, bulk liquid samples.

The use of an internal standard that was able to be analysed by HPLC (that is, not too polar) removed the need for the extra measurements and proved a more reliable measure of concentration. Benzoic acid and *meta*-hydroxybenzoic acid were both tested. These species are both present in the reaction anyway. This complicated the concentration calculations, but removed the possibility that the internal standard species was interfering in the reaction. Benzoic acid was present in high enough concentrations that the decrease in concentration due to the reaction with hydroxyl radicals was insignificant. However, the benzoic acid was present in such high concentrations that the peaks in the chromatograms were distorted and generally less reliable than the *m*-HBA peaks. For this reason *m*-HBA was used as the internal standard. The concentration of *m*-HBA could be chosen to suit the expected concentration of *p*-HBA.

As in the ferrioxalate case, the key quantity for calculations involving radiant flux is the total amount of product. The samples were not consistently weighed after each experiment so some experiments were re-run to establish typical volumes of the samples and hence total amounts of product in the samples. An internal standard was still a useful check that the volume injected into the column by the sample injector of the HPLC was consistent. It was also necessary to establish the total volume of aerosol irradiated over the course of the experiment, which could be used to compare the nitrate/benzoic

acid experiments with the nitrate/CO experiments.

5.4 Calculations

The HPLC produced, for each sample, a chromatogram at three different user-defined wavelengths. These were set to 255, 272 and 298 nm. 255 nm corresponds to a *p*-hydroxybenzoic acid absorption maximum, while 297 nm corresponds to a *m*-hydroxybenzoic acid absorption maximum. The concentration of benzoic acid was initially also followed at 272 nm, which corresponds to a shoulder in its absorption spectrum.

Each sample had a method file associated with it; this file contained the concentrations of the compound in the calibration standards and the retention time for each compound. The Chromeleon software package calculated concentrations from the areas under the peaks from the calibration data. These calculated concentrations were then corrected for dilution via the internal standard to obtain the concentration of *para*-hydroxybenzoic acid that would have resulted had there been no dilution.

For a solution of non-diluted nitrate/benzoic acid with no internal standard, if A and B are the concentrations of product *p*-HBA and *m*-HBA respectively, and X is the ratio of product *m*-HBA to product *p*-HBA then:

$$B = XA. \tag{5.2}$$

The concentrations measured via the calibrated HPLC method were A and B, from which X could be calculated.

If the nitrate/benzoic acid solution has a spike of *m*-HBA added as the internal standard, with an initial concentration M, then the measured concentrations for an undiluted solution are $B + M$ moles of *m*-HBA and A moles of *p*-HBA. If the solution is diluted by an unknown factor D, then the measured concentrations are now:

$$[p\text{-HBA}] = \frac{A}{D}, \tag{5.3}$$

$$[m\text{-HBA}] = \frac{B + M}{D}. \tag{5.4}$$

We would like to know A, the concentration of *p*-HBA for a non-diluted solution. So, substituting for D (Equation 5.4) and B (Equation 5.2):

$$[p\text{-HBA}] = \frac{A[m\text{-HBA}]}{AX + M}, \tag{5.5}$$

and making A the subject gives:

$$A = \frac{M[p\text{-HBA}]}{[m\text{-HBA}] - X[p\text{-HBA}]}. \tag{5.6}$$

Thus, as long as X is known, an internal standard of known concentration M can be used to calculate the concentration of p-HBA in spite of the unknown dilution factor.

The calculation of the amount, in moles, of product formed in the aerosol is straightforward assuming that the volume of the sample is known. The amount is the value required for calculations of quantum yields via Equation (3.1) for the bulk liquid or Equation (3.2) for an aqueous aerosol.

5.5 Benzene as an aqueous phase radical scavenger

Benzene was originally trialled as a gas phase scavenger as an alternative to cyclohexane, as detailed in Section 4.4. The gas phase phenol formed was trapped and analysed by HPLC. While the gas phase yields of phenol were low, a considerable amount of phenol was recovered from the aqueous phase via the impacted aerosol. With the ice/water cooled trap removed, the system was essentially the same as that used with benzoic acid. The only major differences were that the benzene was introduced into the system by bubbling nitrogen through liquid benzene and that oxygen was introduced to the chamber at 10% of the total flow. The oxygen mixed with the nitrogen upstream of the humidifier and nebuliser.

The volumes of sample recovered were similar to the volumes recovered in the benzoic acid experiments. The sample was diluted with 1 to 2 mL of Milli-Q water as it was washed out of the trap. This resulted in sufficient sample for both the HPLC analysis and for the measurement of a UV-visible absorption spectrum.

This system had no added internal standard, so in order for the evaporated or diluted samples to be comparable, the concentration of the nitrate was used as the internal standard. This had proved problematic for the nitrate/benzoic acid experiments, but there appeared to be few other options.

5.5.1 Nitrate concentration analysis with the UV-visible spectrometer

Having collected a sample from the chamber, a 0.5 mL aliquot of sample was diluted by a factor of 20 with Milli-Q water in a volumetric flask. The 10 mL of dilute solution this produced was enough for two UV-visible analyses. A quartz cell of path length 1 cm was used in the GBC 920 UV-visible spectrometer to measure spectra from 500 nm down to 225 nm at a resolution of 0.2 nm and a scan rate of 25 nm min^{-1}.

The absorbance at 305 nm was converted into a concentration (with the molar absorption coefficient taken to be 7.3 L mol^{-1} cm^{-1}) which could then be compared with the peak areas measured in the HPLC analysis.

5.5.2 HPLC analysis

HPLC contour plots of samples from irradiated aerosol showed several distinct products, whereas non-irradiated aerosol showed no signs of products. Figure 5.4 (top) shows an HPLC chromatograph at 272 nm from an irradiated nitrate aerosol in the presence of benzene. Phenol appeared on the chromatograph at a retention time of 15.1 min, with an absorption maximum (λ_{max}) at 272 nm (Figure 5.5, (e) and (f)). A peak at 18.0 min with λ_{max} = 315 nm was unambiguously determined to be *para*-nitrophenol (Figure 5.5, (c) and (d)), while a peak at 21.8 min with λ_{max} = 275 nm was assigned to *ortho*-nitrophenol (Figure 5.5, (a) and (b)). These assignations were confirmed by running samples of pure *ortho*-nitrophenol and *para*-nitrophenol on the HPLC (Figure 5.4, bottom). Pure samples of *meta*-nitrophenol and nitrobenzene were also analysed with the HPLC but their absorption maxima and retention times did not correspond to any peaks in the chromatograph of the irradiated aerosol sample (Figure 5.6).

5.5.3 Nitrate analysis with the HPLC

An attempt at calibrating the HPLC analysis for cyclohexanone was not successful due to a lack of reproducibility. Rather than varying the concentration of cyclohexanone (in isopropyl alcohol) the injection volume had been varied. It was clear that this was not an appropriate method. The actual injection volume did not correspond to the programmed injection volume. The sample injector of the HPLC was cleaned, but little improvement in the reproducibility was seen. The vast majority of analyses with the HPLC had been

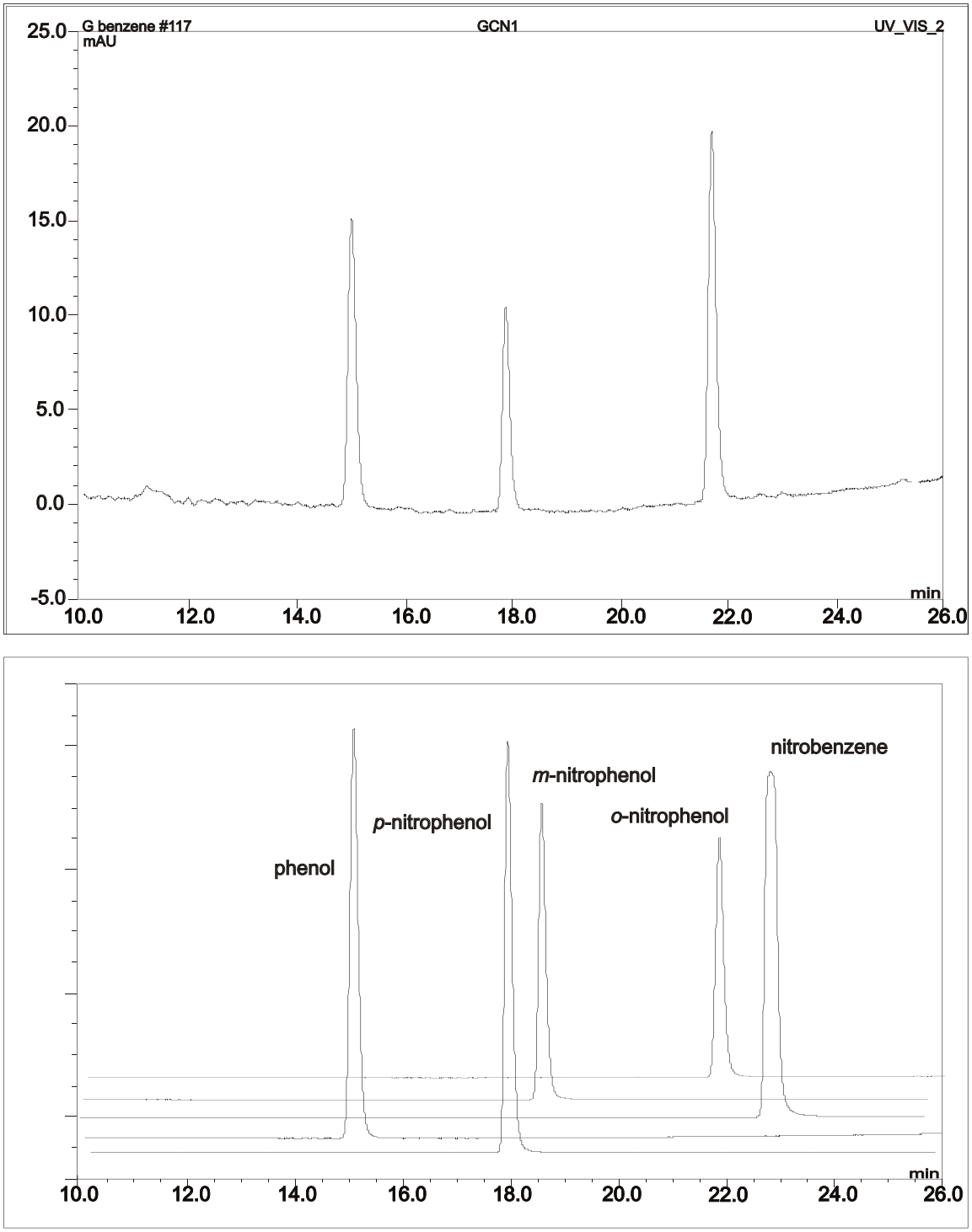

Figure 5.4: Top: an HPLC chromatograph from a nitrate aerosol irradiated in the presence of benzene. Bottom: HPLC chromatographs from pure samples of phenol, nitrobenzene, *para*-nitrophenol, *meta*-nitrophenol and *ortho*-nitrophenol.

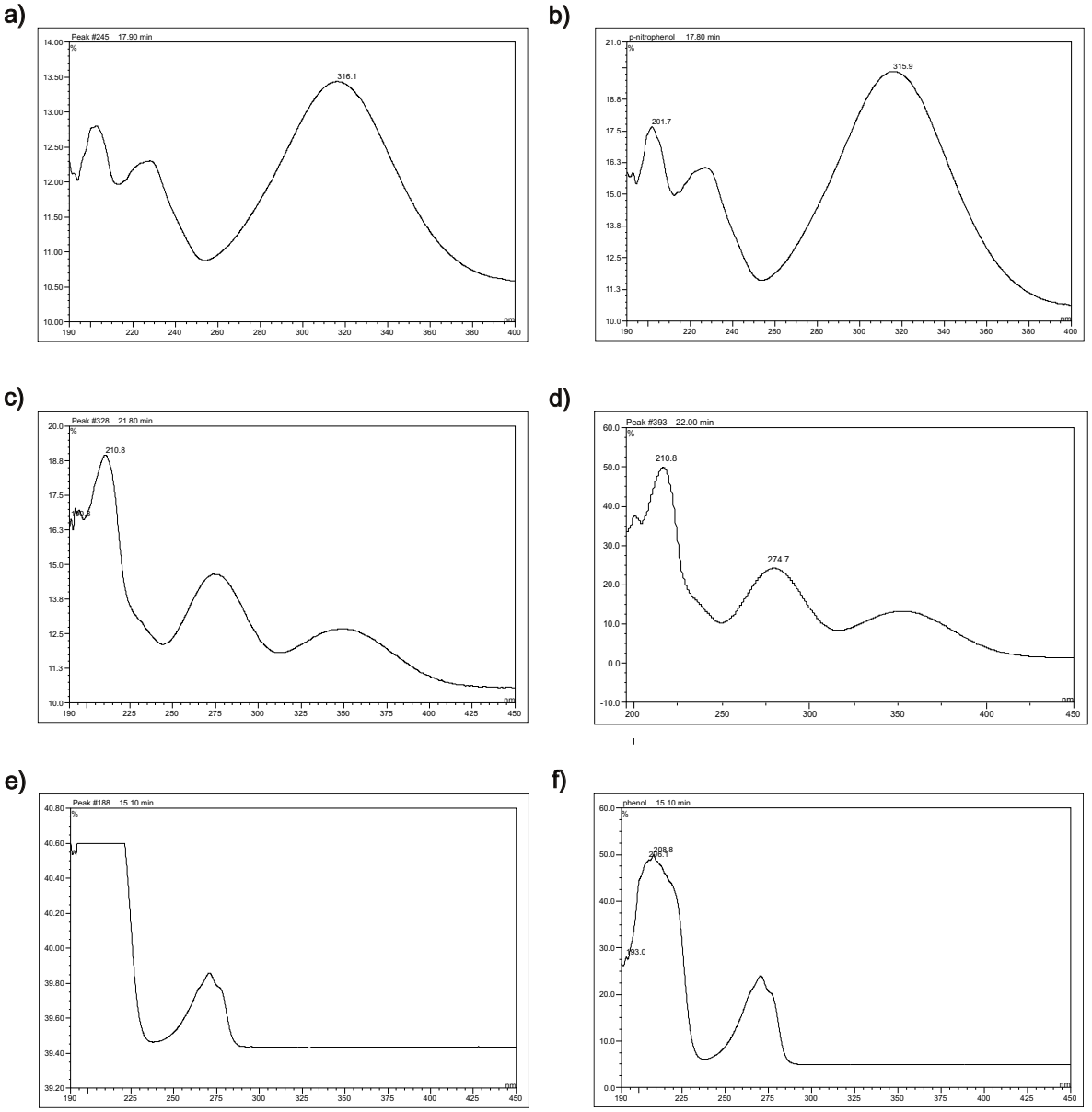

Figure 5.5: Absorption spectra at specific HPLC retention times:
(a) UV spectrum of sample peak with retention time of 17.9 min and $\lambda_{max} = 316$ nm.
(b) UV spectrum of *para*-nitrophenol peak, retention time = 18.2 min.
(c) UV spectrum of sample peak with retention time of 22.0 min and $\lambda_{max} = 275$ nm.
(d) UV spectrum of *ortho*-nitrophenol peak, retention time = 21.8 min.
(e) UV spectrum of sample peak with retention time of 15.1 min and $\lambda_{max} = 275$ nm.
(f) UV spectrum of phenol peak, retention time = 15.3 min.

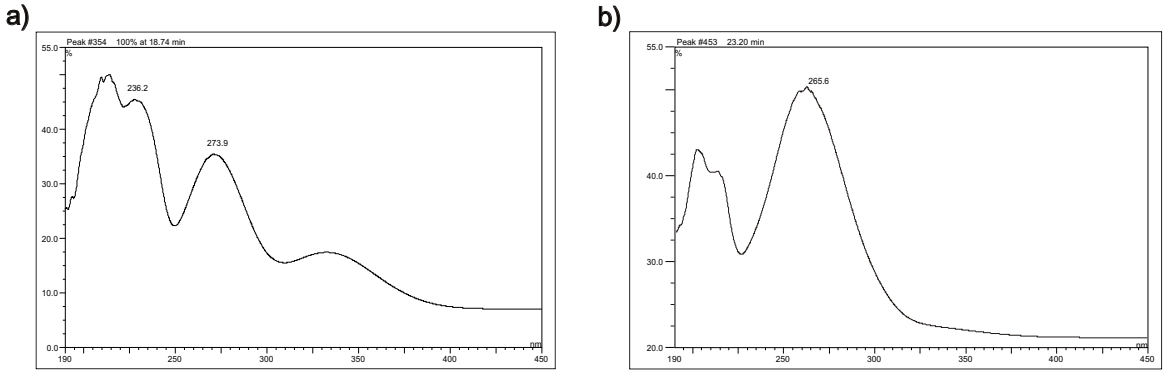

Figure 5.6: (a) UV spectrum of *meta*-nitrophenol peak, retention time = 18.7 min. (b) UV spectrum of nitrobenzene peak, retention time = 23.2 min.

carried out with an injection volume of 100 μL and had provided reproducible results and linear calibrations. The best option was to use injection volumes of 100 μL for every sample. Even when a consistent injection volume was used, repeat measurements of phenol concentrations gave values varying by up to 30% from each other. A clear advantage of having a true internal standard that is measured in the same analysis as the unknown is that variables like injection volume become irrelevant.

The nitrate peak appeared in the chromatographs at a retention time of 3 min. This was very early; it suggested that the peak would not be analysable due to poor reproducibility. Overloading of the UV-visible detector (DAD) was also expected to be a problem. However, the peaks corresponding to nitrate at 298 nm[2] appeared Gaussian in shape. This suggests that not only were they not overloaded, but that there was no other compound coeluting with nitrate. Moreover, the ratios of the nitrate peak areas with the phenol peak areas were reproducible.

The overload limit for a C_{18} reverse phase column is about 2 mg of sample per gram of C_{18} material [113]. A 100 μL aliquot of 1 mol L^{-1} lithium nitrate corresponds to about 6 mg of nitrate. The column used had about 2 g of active stationary phase. This suggests that the column was somewhat overloaded. However, because nitrate is a highly soluble anion, it is eluted with the solvent front. The short retention time ensures a sharp peak,

[2]The absorption maximum of nitrate is at 305 nm but the detector had previously been set to 298 nm to detect *m*-HBA. By keeping the detection wavelength at 298 nm, all previously run HPLC chromatographs could also be analysed for nitrate concentration.

and also lessens the interference with the elution times of the aromatic compounds.

5.5.4 Product concentration calculations

The concentrations of the hydroxylated and nitrated products of the reaction of benzene with hydroxyl radical were calculated from the peak areas of the compounds detected via HPLC. A calibration with standard solutions of phenol, *ortho*-nitrophenol and *para*-nitrophenol enabled the measured peak areas to be converted to concentrations. The ratio of these concentrations with the measured concentration of nitrate was used to calculate the undiluted concentration of the product:

$$[product]_{measured} = Peak\,area \times calibration\,factor,$$

$$[product]_{undiluted} = \frac{[product]_{measured}}{[\mathrm{NO_3}^-]_{measured}}[\mathrm{NO_3}^-]_{original},$$

where $[\mathrm{NO_3}^-]_{original}$ is the concentration of the nebulised nitrate solution.

5.6 Summary of experimental chapters

Together, the experiments reported in Chapters 2 through 5 aimed to build a picture of the physical and chemical processes taking place within the system. The physical properties of the aerosol as measured with the Aerodynamic Particle Sizer (Chapter 2) were used to calculate aerosol absorption cross sections for the aerosols studied in Chapters 3, 4 and 5. The bulk liquid experiments for the chemical actinometer (Chapter 3) gave the radiant flux of the chamber while the bulk liquid radical scavengers (this chapter) gave an experimental scavenger product yield that allowed a comparison with the aerosol phase yields, including the gas phase scavenger experiments of Chapter 4.

Chapter 6

Results and discussion

This project naturally divided itself into the four parts presented in the four Experimental chapters. It was intended that the results from each part would complement the results from the others and a detailed picture of the chemistry of hydroxyl radical in a liquid aerosol would emerge. The results, however, were not as conclusive as was hoped because the scavenger carbon monoxide did not discriminate strongly enough between gas phase and liquid phase hydroxyl radical.

The particle size distributions are the basis which several later calculations rely. Geometric means, geometric standard deviations and total particle concentrations are reported in Section 6.1. These parameters were then used to calculate aerosol absorption coefficients, b_{abs} for both volume-weighted and number-weighted particle size distributions, using refractive indices calculated from the absorption coefficients of the nebulised solutions.

The irradiance in the chamber was measured with the ferrioxalate actinometer contained in a close-fitting Petri dish; this value is reported in Section 6.2. Also reported are the rates of Fe^{2+} produced when ferrioxalate aerosols were irradiated; these values proved to be unexpectedly high. Possible reasons for the difference between bulk liquid and aerosol results are explored in this section.

Yields of hydroxyl radical from nitrate photolysis were measured with nitrate/benzoic acid solutions, both as a bulk liquid and as an aerosol and are reported in Section 6.3. The nitrate/benzoic acid system was the only system for which results were obtained both in the presence and in the absence of the dielectric filter. This provided a link between the ferrioxalate results and the gas phase results. The variation of the lamp output with wavelength is a potential source of error in this comparison.

Section 6.4 reports the measured gas phase concentrations of hydroxyl radical via the carbon dioxide produced when aqueous solutions of sodium nitrate, lithium nitrate and a sodium chloride 'blank' were irradiated in the presence of carbon monoxide. The other gas phase scavenger that was tried, cyclohexane, is also mentioned in this section but, because any changes in concentration were below the limit of sensitivity of the mass spectrometer, only an upper limit of product concentrations can be reported.

Section 6.5 summarises some results from the aqueous reaction of benzene with hydroxyl radical produced in nitrate photolysis. Again, the results were less useful than those obtained with a benzoic acid scavenger. Overall, the results indicate that the quantum yield of the actinometer is significantly enhanced in the aerosol, while the yield of hydroxyl radical from nitrate is somewhat enhanced.

Attempts to draw together the results from the various systems to calculate and compare the hydroxyl radical quantum yields proved unsuccessful, due mainly to the very high yield in aerosols of the ferrioxalate actinometer and in aerosols of benzoic acid/nitrate. Thus the original hypothesis, that the gas phase yields of hydroxyl radical from aerosols would be enhanced due to light intensity enhancements and a reduced solvent cage effect, has not been tested, although it could help account in part for some of the anomalies observed.

The remaining four sections constitute the discussion section of the chapter, starting with an explanation of the physical processes affecting the aerosol during the experiment. The relevance of the results reported here is discussed, both in terms of the solubility problem with gas phase scavengers and in terms of ambient atmospheric aerosol concentrations and particle sizes. The final two sections discuss the limitations of the experimental set-up and suggest some further experiments that would improve the accuracy and applicability of the results.

6.1 Particle size distribution trends

6.1.1 Particle concentration for concentrated nitrate solutions

Concentrated solutions of sodium and lithium nitrate ($2\,\mathrm{mol\,L^{-1}}$) produced high particle concentrations and hence a very narrow range of sampling flow rates over which the concentrations and particle size distributions of the aerosols were measurable (see

Figure 2.18). Over this narrow range of sampling flow rates, a linear relationship between sampling flow rate and particle concentration was observed. By extrapolating this relationship to the point at which the sampling flow rate equalled the total flow rate, total particle concentrations for undiluted aerosols could be calculated. The undiluted particle number concentration for aerosols from concentrated nitrate solutions was $(3.0 \pm 1.0) \times 10^5$ particles cm^{-3}.

6.1.2 Particle concentration for dilute nitrate solutions

Plots of the particle number concentration against sampling flow for dilute solutions ($0.1\,\mathrm{mol\,L}^{-1}$) of sodium and lithium nitrate showed a less distinct knee than plots for concentrated solutions. As with the concentrated solutions, the curve flattened at high sampling flows, with the maximum measured particle number concentrations never higher than 4 000 particles cm^{-3} (see Figure 2.19). The particle number concentration for dilute solutions was $(1.5 \pm 0.3) \times 10^5$ particles cm^{-3}.

6.1.3 Particle size distributions of potassium ferrioxalate aerosol

Nebulisation of $0.05\,\mathrm{mol\,L}^{-1}$, 'fresh' (that is, not previously irradiated) solutions of potassium ferrioxalate produced aerosol with similar particle size distributions to those seen for dilute nitrate solution. Plots of sampling flow against particle concentration showed slopes of 22 000 particles $\mathrm{cm}^{-3}(\mathrm{L\,min}^{-1})^{-1}$, corresponding to total particle concentrations averaging $(1.0 \pm 0.1) \times 10^5$ particles cm^{-3}.

6.1.4 Median and geometric mean of particle size distributions

Dilute nitrate solutions produced aerosols with particle size distributions with a median particle diameter of $0.63\,\mu$m, when the particle concentrations were at a measurable level. The median particle diameter for concentrated nitrate solutions was somewhat higher, at $0.7\,\mu$m. The size of the droplets produced by the nebuliser decreased slightly over the course of an experiment. Below the high concentration threshold, the largest median particle diameter observed for any distribution was $0.84\,\mu$m. Figures 6.1 and 6.2 are particle size distributions for a dilute nitrate solution and a concentrated nitrate solution respectively. The sampling flow for both was $0.04\,\mathrm{L\,min}^{-1}$, while the total flow to the Aerodynamic Particle Sizer (sampling flow plus dilution gas flow) ranged from

4.70 to 4.75 $\mathrm{L\,min^{-1}}$ during these experiments.

The geometric means, as calculated from log-normal fits to the data, were higher than the median particle diameters and also varied with concentration. Particle size distributions of dilute nitrate solutions had a geometric mean of 0.69 μm with a standard deviation of 1.45 μm while particle size distributions of concentrated nitrate solutions exhibited a geometric mean diameter of 0.81 μm with a standard deviation of 1.67 μm. The higher values for the geometric mean for log-normal fits than for the raw data are a result of the fairly poor log-normal fits. This is reflected in the normalised Chi-squared values (from Equation (2.13)) for the log-normal distributions as compared to the experimental data, which were 0.19 and 0.16 for dilute and concentrated solutions respectively. Equation (2.13) is not a standard test, but these values can be compared against each other as well as the log-normal fits of Whitby and Sverdrup who achieved tri-modal log-normal fits with χ_n^2 values as low as 0.005 for ambient aerosol size distributions [89].

Potassium ferrioxalate aerosol particle size distributions were similar to the nitrate aerosol size distributions in general. The median particle diameter from the experimental data was 0.67 μm while the geometric mean was 0.72 μm, with a geometric standard deviation of 1.48 μm. The average normalised Chi-squared value was 0.22, indicating an even poorer fit than those of the nitrate solutions.

6.1.5 Aerosol absorption coefficients

Absorption coefficients were calculated in the manner outlined in Section 1.5.2 for potassium ferrioxalate aerosol and for aerosols from the dilute and concentrated solutions of sodium nitrate. The coefficients were calculated for both experimental data and synthesised log-normal distributions. For the ferrioxalate aerosols, the results were similar for experimental and synthesised data, but for both the dilute and concentrated nitrate aerosols the experimental data produced absorption coefficients significantly different from those of the synthesised data. Although the log-normal fits had high χ_n^2 values and did not visually appear to be good fits, it proved necessary to use the synthesised data since the majority of the calculated absorption coefficients are volume-weighted, being dependent on the cube of the particle diameter. The absorption coefficients from these synthesised log-normal distributions are quoted in Table 6.1 and were used to calculate the quantum yields in later sections.

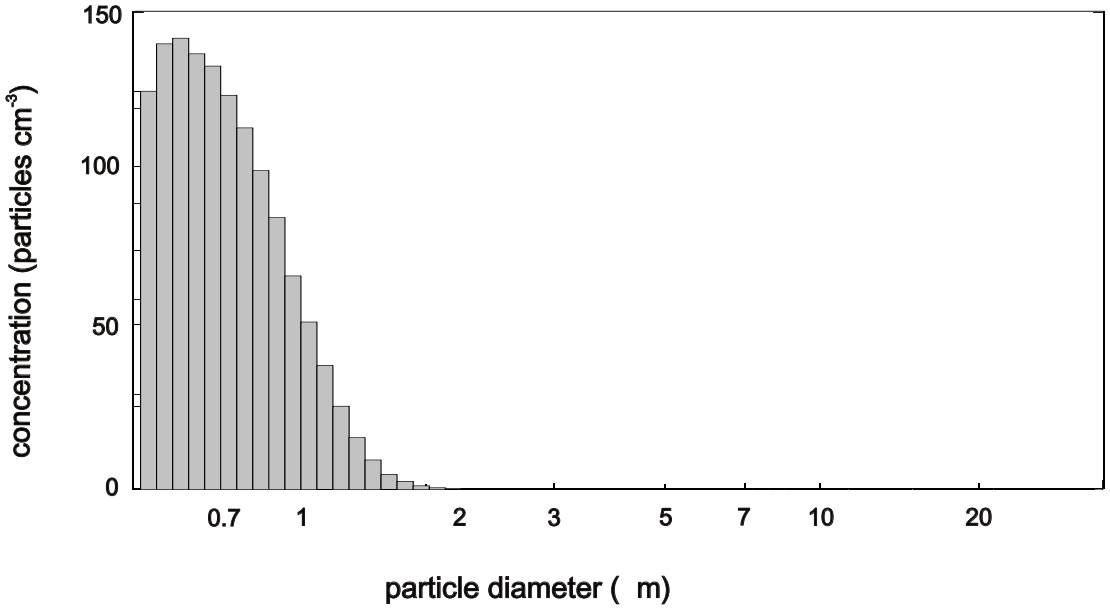

Figure 6.1: Number particle size distributions for a dilute nitrate solution ($0.1\,\mathrm{mol\,L^{-1}}$).

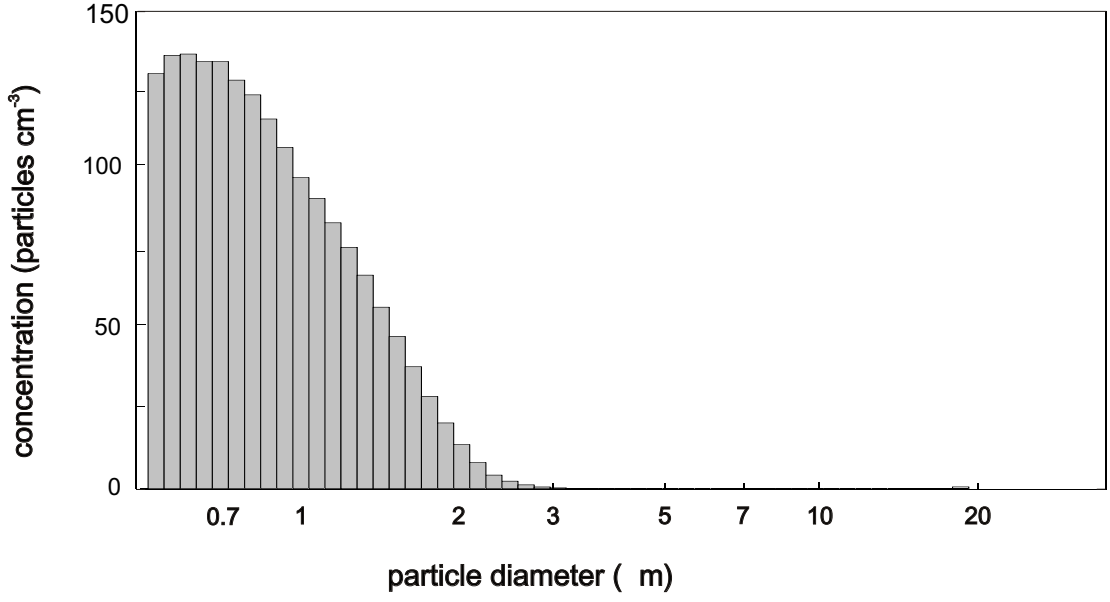

Figure 6.2: Number particle size distributions for a concentrated nitrate solution ($2\,\mathrm{mol\,L^{-1}}$).

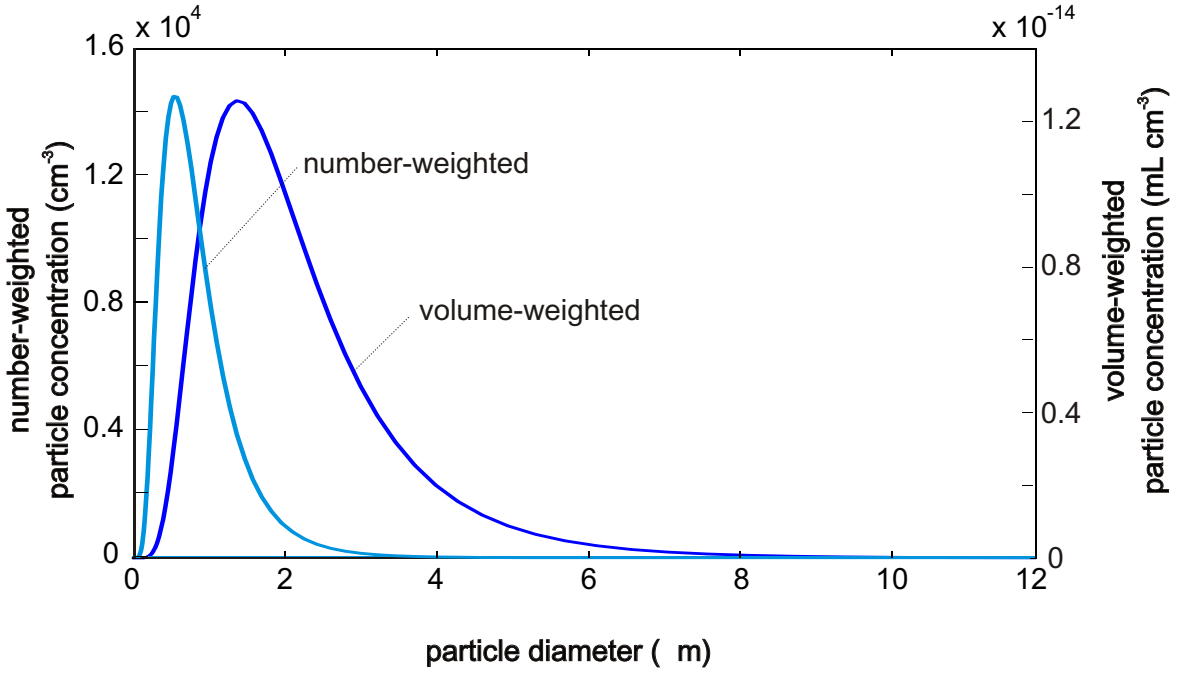

Figure 6.3: A comparison between a fitted log-normal number-weighted particle size distribution and the corresponding volume-weighted distribution ($2\,\mathrm{mol\,L^{-1}}$ $NaNO_3$).

A volume-weighted calculation of the absorption coefficients was necessary when the aerosol was collected by impaction then analysed as a bulk liquid. This includes the ferrioxalate actinometry and all the experiments with an aqueous phase scavenger. This is because once the aerosol has been collected at the impactor, the larger droplets will have contributed an amount of product that is dependent on their volume. This is not the case for gas phase measurements. Calculation of the volume-weighted total absorption coefficients required multiplication of the contribution to the absorption coefficient from each particle diameter by its relative, normalised volume. Figure 6.3 compares a typical number-weighted particle size distribution with the volume-weighted distribution.

solution	filter	particles cm^{-3}	weighting	absorption coefficient (b_{abs}) (m^{-1})
0.05 M FeOx†	dielectric	100 000	volume	$7.4 \pm 1.1 \times 10^{-3}$
0.1 M $NaNO_3$	dielectric	150 000	volume	$4.9 \pm 1.3 \times 10^{-5}$
0.1 M $NaNO_3$	none	150 000	volume	$3.1 \pm 0.8 \times 10^{-5}$
2 M $NaNO_3$	none	300 000	volume	$6 \pm 4 \times 10^{-3}$
2 M $NaNO_3$	none	300 000	number	$1.0 \pm 0.5 \times 10^{-3}$

† potassium ferrioxalate

Table 6.1: Calculated aerosol absorption coefficients (b_{abs}) for the various aerosols studied, for light of wavelength 305 nm. While the absorption coefficients are directly proportional to the particle concentrations and the optical density of the original solution, variations in the particle size distributions prevent direct comparisons. The potassium ferrioxalate aerosol was intended to have a similar absorption coefficient to 10 mol L^{-1} nitrate aerosol; the three-fold higher particle concentrations and somewhat larger geometric mean diameters for the concentrated nitrate aerosol resulted in comparable volume-weighted absorption coefficients for the 2 mol L^{-1} nitrate aerosol and the ferrioxalate aerosol. Molar absorption coefficients (α, base e) for potassium ferrioxalate and sodium nitrate are 5500 and 17 L mol^{-1} cm^{-1} respectively.

6.2 Actinometry results

The results reported in this section were all obtained from experiments with the 5 mm glass impactor upstream of the chamber and using a O.D. = 2.0 neutral density filter.

Calvert and Pitts [58] compiled quantum yields for potassium ferrioxalate. The quantum yield at 313 nm for 0.006 mol L^{-1} potassium ferrioxalate is reported as 1.24. The values reported in the literature for the quantum yield of the reduction of potassium ferrioxalate vary by up to 10% depending on the concentration used. The two standard concentrations of potassium ferrioxalate used for actinometry are 0.006 mol L^{-1} and 0.15 mol L^{-1}. The experiments reported here used solutions with concentrations of 0.05 mol L^{-1} and 0.15 mol L^{-1}.

6.2.1 Bulk phase actinometry results

The radiant flux entering the Petri dish halfway down the chamber was measured to be $(2.7 \pm 0.4) \times 10^{15}$ quanta s^{-1}, corresponding to an irradiance of $(1.4 \pm 0.2) \times 10^{18}$ quanta s^{-1} m^{-2},

set	Fe^{3+} concentration ($mol\,L^{-1}$)	$N^{\dagger}$	radiant flux ($quanta\,s^{-1} \times 10^{15}$)	rate of Fe^{2+} production ($molecules\,s^{-1} \times 10^{15}$)
BD	0.055 ± 0.001	4	3.6 ± 1.3	4.0
BE	0.164 ± 0.005	5	3.6 ± 0.8	4.0
BF	0.053 ± 0.001	3	3.6 ± 0.8	4.1
BG	0.050 ± 0.001	5	3.2 ± 0.6	3.6
BH	0.053 ± 0.001	4	2.9 ± 0.7	3.2
overall		21	3.4 ± 0.3	0.3
non-irradiated		12	0.3 ± 0.1	3.8
corrected			3.1 ± 0.5	3.5

† N is the number of samples

Table 6.2: Results from bulk phase actinometry for experiments using both the O.D. = 2 neutral density filter and the narrow band dielectric filter.

since the Petri dish used had a radius of 0.045 m. Since the potassium ferrioxalate has a large molar absorption coefficient ($\epsilon = 2378\,L\,mol^{-1}\,cm^{-1}$) and the depth of solution in the dish was 1 cm, all of the light that enters the Petri dish of ferrioxalate solution was absorbed regardless of the concentration of ferrioxalate used. The five individual sets of measurements along with the average of these five sets and the average dark reaction are given in Table 6.2. Because the walls of the Petri dish were about 2 mm thick, the radiant flux for the entire chamber is slightly higher than the radiant flux entering the Petri dish; the values in Table 6.2 have been corrected for this factor.

6.2.2 Aerosol phase actinometry results

Table 6.3 shows the calculated rate of production of Fe^{2+} in molecules per second for aerosol in the chamber; Table 6.4 presents earlier results calculated retrospectively using the average collected sample volume of the results in Table 6.3. The measured rate is considerably lower than the rates reported in Table 6.2 for the bulk results. Since the bulk liquid actinometer is absorbing all of the light in the chamber due to its high optical density, the rate of production of Fe^{2+} in the aerosol cannot be higher than the bulk liquid value. A quick calculation of the total cross sectional area of the aerosol particles in the chamber shows that, even with the ferrioxalate aerosol particle concentration of 100 000 $particles\,cm^{-3}$, only 12% of the light should even encounter a particle, let alone be absorbed. The aerosol absorption coefficient, b_{abs}, is such that 0.3% of the light will be absorbed by the aerosol.

set	Fe^{3+} concentration ($mol\,L^{-1}$)		N	rate of Fe^{2+} production ($molecules\,s^{-1}$ $\times 10^{14}$)
BH	0.05	irradiated	6	3.4 ± 0.2
		dark reaction	5	0.4 ± 0.2
		corrected for dark reaction		3.0 ± 0.4

Table 6.3: Results from aerosol phase actinometry for experiments using both the O.D. = 2 neutral density filter and the narrow band dielectric filter.

set	Fe^{3+} concentration ($mol\,L^{-1}$)		N	rate of Fe^{2+} production ($molecules\,s^{-1}$ $\times 10^{16}$)
BD	0.05	corrected for dark reaction	8	2.9 ± 0.8
BF	0.05	corrected for dark reaction	9	3.3 ± 1.2

Table 6.4: Results from earlier aerosol phase actinometry experiments, calculated retrospectively from the average collected sample volume measured during set BH.

Quantum yields for the aerosol phase actinometry were calculated, using a rearranged version of Equation (1.27). This gives a quantum yield for BG series of 32, a factor of 26 larger than the quantum yield for the bulk ferrioxalate. The quantum yields for the actinometry and for the OH scavenging experiments are compared later in Table 6.10 page 154.

Although Mie theory has been applied analytically to dielectric spheres, the emphasis has been on light scattering outside of the droplet. The calculated absorption efficiencies were assumed to be the difference between the calculated extinction efficiencies and scattering efficiencies: they do not take into account the light intensity enhancements from morphology dependent resonances within the droplet. The situation is not straightforward, since the resonances create a much longer effective path length for light within the droplets. The calculations of intensity averaged over the volume of the droplet and over all relevant size parameters indicate an average enhancement by a factor of 2 [2, 3]. This goes a small way towards explaining the discrepancy, but cannot explain the dramatic enhancements observed in the present experiments.

The molar absorption of the solution is incorporated into b_{abs} as k, the imaginary component of the index of refraction. As explained in Section 1.5.2 values for k vary widely for solid and liquid particles. For a liquid aerosol, k as derived from the molar

absorption coefficient (Equation (1.18)) should apply, namely:

$$k = \frac{\alpha\lambda c}{4\pi},$$

where λ is the wavelength, c is the concentration of the solution and α is the molar absorption coefficient in base e. It is possible that this variation in k is another indication of the failure of Mie theory to explain the observed light enhancements in aerosols.

The full mechanism for the photoreduction of potassium ferrioxalate involves a second reduction of Fe^{3+} (Equation (3.4)) which results in a quantum yield greater than one. If the reduction of the solvent cage effect in the aerosol droplets meant that the $CO_2{\cdot}^-$ radicals produced in the reaction were less likely to recombine, this would increase the quantum yield, but the theoretical maximum quantum yield possible from this mechanism is 2; not nearly enough on its own to account for the very large yields for the aerosol.

Oxygen is known to reoxidise some of the Fe^{2+} produced:

$$Fe^{2+} + 2H^+ + \frac{1}{2}O_2 \rightarrow Fe^{3+} + H_2O, \tag{6.1}$$

which lowers the measured product yields. Calvert and Pitts recommend stirring the solution with oxygen-free N_2 [58]. Although the bulk liquid experiments were carried out under a flow of N_2 they were not typically stirred, so the bulk liquid would have had some oxygen dissolved in it. The Henry's law constant for oxygen is $1.3\times10^{-3}\,\mathrm{mol\,L^{-1}\,atm^{-1}}$ so the concentrations of oxygen in the ferrioxalate solution were about $3\times10^{-4}\,\mathrm{mol\,L^{-1}}$. This initial concentration of oxygen applies to the aerosol too; however, the small size of the droplets suggests that in an oxygen-free carrier gas, the oxygen would have ample time to diffuse out of the droplets between the nebuliser and the chamber. The photoreduction in the aerosol, then, would not be retarded to the same extent as the reaction in the bulk liquid and the aerosol yields would hence be higher. However purging the bulk solution of oxygen (by bubbling nitrogen through the solution in the Petri dish for several hours) did not result in an increase in yields from the bulk liquid solutions.

None of the explanations proposed above come close to explaining the high yields of Fe^{2+} in the aerosol phase on their own. Even combined, the contribution from these factors is insufficient to explain the high yield. The only remaining explanation is that the ferrioxalate anion concentration is enhanced on the surface of the droplets. Although this

may conflict with the standard picture from the Gibb's isotherm surface model, it does correspond with recent molecular dynamics calculation that point to large, polarisable anions preferring the gas-liquid interface over the bulk liquid [52]. The calculation of an average enhancement factor of 2 due to resonances depended on the Mie resonances occurring only for discrete wavelengths; their effect is then swamped by non-resonant light during broadband illumination. However, the effect of the evanescent wave on illumination at the surface of the forward hemisphere of the droplet is not strongly wavelength dependent and so does not average out. Thus the scattered light produces photolysis in addition to the absorbed light. This effect would be very important for a species which was concentrated in the surface layer. It is proposed that this is the reason for the enhanced yield for the ferrioxalate actinometer in the aerosol.

6.3 Aqueous phase radical scavenger

Equation (5.6) was used to calculate the yield of *para*-hydroxybenzoic acid for aerosol phase and bulk liquid experiments. Each sample was typically measured twice, so the average of the two yields was calculated. For each set of experiments, averages and standard deviations were calculated for irradiated aerosol, for non irradiated aerosol and for bulk liquid solutions. Uncertainties were estimated via Student's t distribution. Table 6.5 lists the conditions for each set of experiments, serving as a key to the bulk liquid results, Table 6.6, and the aerosol phase results, Table 6.7. The buffer (sodium bicarbonate) maintained the pH at around 8; without a buffer, the presence of the benzoic acid ($pK_a = 4.2$) lowered the pH to around 4.

6.3.1 Bulk liquid results

The neutral density filter was not used for any of the experiments with nitrate/benzoic acid, so the radiant flux in the chamber is 100 times that measured with the bulk ferrioxalate solutions. This results in a value of $3.1\times10^{17}\,\mathrm{quanta\,s^{-1}}$. Substituting this and the measured rate of production of p-HBA into Equation (3.1) results in a quantum yield for p-HBA of 3.0×10^{-4}. Thus, for every mole of photons absorbed by the solution, just 3.0×10^{-4} moles of p-HBA were produced. The quantum yield for the production of the hydroxyl radical from the photolysis of nitrate is 0.017, so only 1.8% of the hydroxyl radical produced was reacting with benzoic acid to form *para*-hydroxybenzoic acid.

set	$[NO_3^-]$ ($mol\,L^{-1}$)	[BA] ($mol\,L^{-1}$)	cation	dielectric filter	buffer pH = 8
DA	0.11	4.5×10^{-3}	Na	yes	yes
DB	0.11	7.8×10^{-3}	Na	yes	yes
DC	0.11	4.3×10^{-3}	Na	yes	no
DD	0.10	4.2×10^{-3}	Li	yes	yes
DE	0.11	4.3×10^{-3}	Na	no	yes
DF	0.55	8.0×10^{-3}	Na	no	yes
DG	2.09	7.9×10^{-3}	Na	no	yes
DH	0.11	1.4×10^{-3}	Na	no	yes

† N is the number of samples

Table 6.5: Summary of conditions used in nitrate/benzoic acid experiments.

set	N	Rate of production of p-HBA ($mol\,L^{-1}\,s^{-1}$)
DA	5	$2.1 \pm 0.2\times10^{-9}$
DB	6	$2.2 \pm 0.3\times10^{-9}$
DC	5	$2.01 \pm 0.04\times10^{-9}$
DD	5	$2.6 \pm 0.5\times10^{-9}$
DE	4	$8.0 \pm 1.5\times10^{-9}$
DF	3	$1.4 \pm 0.3\times10^{-8}$
DG	4	$1.3 \pm 0.3\times10^{-8}$
DH	4	$1.6 \pm 0.2\times10^{-8}$

Table 6.6: p-HBA yield from irradiated bulk nitrate/benzoic acid solutions.

Previous investigations using benzoic acid as a scavenger have reported yields of 8.1 and 8.3% for the reaction of hydroxyl radical with benzoic acid [4, 115]. The concentrations of nitrate in these previous experiments were lower by several orders of magnitude, so it is possible that the discrepancy with the yields measured in this experiment is due to the much higher nitrate concentrations used. The yield of *p*-HBA has been observed to be dependent on ionic strength but in fact the previous experiments suggest it should increase at higher ionic strengths. Ideally, the experiments reported here would have included much lower nitrate concentrations, but the sensitivity of the HPLC system used was not high enough to detect products at these concentrations.

Effect of benzoic acid concentrations

Between set DA and set DB, the benzoic acid concentrations were doubled. There was no significant difference in the yields of *p*-HBA for either the bulk liquid solution (Table 6.6) or the aerosol phase solution (Table 6.7). This implies that the concentration of benzoic acid was in excess and was not the limiting factor in the scavenging of the hydroxyl radical.

Sets DE and DH are another pair of sets where the only difference between the two is the benzoic acid concentrations (4.3×10^{-3} and $1.4\times10^{-3}\,\mathrm{mol\,L^{-1}}$ respectively). The yields of *p*-HBA of set DH were in fact somewhat higher in spite of the lower scavenger concentrations.

6.3.2 Aerosol results

Similarly to the yields from the ferrioxalate aerosol, yields for the nitrate aerosol can be compared with the yields from the bulk using the aerosol absorption coefficient b_{abs} and the measured radiant flux. Substituting these values into Equation (3.2) results in a quantum yield for *p*-HBA of 0.27% for the set DB, which was run with the dielectric filter in place and with dilute nitric acid ($0.1\,\mathrm{mol\,L^{-1}}$). Again, this value is a little high, given that the quantum yield of hydroxyl radical is 1.7% and of this only 2% would be expected to react with the benzoic acid to yield *p*-HBA.

set	N	final concentration [p-HBA](mol L^{-1})	rate (amount) molecule s^{-1}
DA	10	$(2.2\pm1.1)\times10^{-7}$	$(2.0\pm0.7)\times10^{10}$
DB	7	$(2.7\pm0.7)\times10^{-7}$	$(1.6\pm1.0)\times10^{10}$
DC	10	$(1.5\pm0.4)\times10^{-7}$	$(1.1\pm0.4)\times10^{10}$
DD	9	$(2.6\pm0.4)\times10^{-7}$	$(1.9\pm0.4)\times10^{10}$
DE	10	$(3.0\pm0.2)\times10^{-5}$	$(2.2\pm0.3)\times10^{12}$
DF	6	$(1.1\pm0.1)\times10^{-4}$	$(7.7\pm1.3)\times10^{12}$
DG	8	$(2.0\pm0.2)\times10^{-4}$	$(1.4\pm1.9)\times10^{13}$
DH	9	$(3.9\pm0.3)\times10^{-5}$	$(2.9\pm0.4)\times10^{12}$

Table 6.7: p-HBA yields in terms of concentration and rate of molecules produced per second from irradiated nitrate/benzoic acid aerosol, corrected for the dark reaction.

Effect of dielectric filter

A comparison of the bulk liquid p-HBA yields for set DB and set DE shows a four-fold increase in yield when the dielectric filter was removed from the optical path. The aerosol phase results for DB and DE show yields measured without the filter are about 210 times those measured with the filter.

The dielectric filter was used in an attempt to limit the light to a single wavelength. The bandwidth of the filter is 27 nm at 50% transmission. The quantum yields for both hydroxyl radical from nitrate photolysis and the photoreduction of ferrioxalate are largely independent of wavelength [4, 112], but the molar absorption coefficient of potassium ferrioxalate is heavily wavelength dependent. The dielectric filter was assumed to limit the wavelength to 305 nm, but the absorption coefficient at 305 nm was actually an effective average across the band of transmitted light.

This assumption introduces some uncertainty, but of more importance is the intensity of light from the mercury-xenon arc lamp as a function of wavelength. The lamp emitted intense light at wavelengths corresponding to the mercury emission lines, such as 313 nm. Even over the bandwidth of the dielectric filter, several spikes in intensity can be seen in the spectrum from the lamp (Figure 2.8). This variation in the emission spectrum generates a level of uncertainty that makes it very difficult to produce a meaningful measurement of the radiant flux at 305 nm. It should be noted, however, that the aerosol absorption coefficients for monochromatic light of wavelength 313 nm are similar

to the broadband absorption coefficients.

The nitrate/benzoic acid system provided an opportunity to quantify the effect of the dielectric filter, since measurable yields of *p*-HBA were produced both with and without the dielectric filter. This was necessary since gas phase yields were detected only in the absence of the dielectric filter. However, given the spikes in intensity at various points in the mercury-xenon arc lamp spectrum this is necessarily a crude measure. One difference was manifest in the aerosol absorption coefficients, since the molar absorption coefficient of nitrate varies with wavelength. For this reason, b_{abs} for experiments without the dielectric filter is an average over the contributions to b_{abs} at each individual wavelength, for each size parameter.

Quantum yields were calculated for aerosol from concentrated nitrate solutions irradiated in the absence of the dielectric filter, with the radiant flux 2×10^4 times the value measured with the bulk ferrioxalate solution, since both the dielectric filter and the neutral density filter were absent. The quantum yield calculated for *p*-HBA under these conditions was 9×10^{-5}, lower than that calculated for the aerosol from dilute nitrate solutions as well as the bulk liquid value. If the enhanced quantum yields are due to enhancements in the radiation in the droplet, it would follow that a higher concentration of sodium nitrate would result in damped resonances enhancements and negligible enhancements in quantum yield. The scavenging of the hydroxyl radical may in fact be inhibited by the high concentrations of sodium nitrate.

Effect of pH on hydroxyl radical yield

The aerosol phase *p*-HBA yields for the experimental set without the buffer (DC) were only 60% of the set with the buffer (DB; Table 6.7). This effect was not observed for the bulk liquid phase experiments: the *p*-HBA yield of non buffered solutions was within experimental uncertainty of the yield of buffered solutions. In the absence of the buffer, the nitrate/benzoic acid solutions have an initial pH of 4. With the buffer, the pH is 8. The OH quantum yields reported by Zellner *et al* [112] and the other OH quantum yields in the summary by Mack [1] are largely pH independent, over the pH range of 4 to 9.

The extra acidity would have corresponded to a greater fraction of the benzoic acid being protonated. Benzoic acid has a pK_a of 4.19 [109] so would be almost equal

in concentrations to its conjugate base, benzoate, at pH = 4. At pH = 8, the pH of the buffered nitrate/benzoic acid solutions, benzoic acid would be almost entirely converted into benzoate anion. However, as implied by the pH independence, the aqueous rates of reaction for benzoic acid and the benzoate ion with hydroxyl radical are similar ($1.8\times10^9\,\mathrm{L\,mol^{-1}\,s^{-1}}$ and $5.9\times10^9\,\mathrm{L\,mol^{-1}\,s^{-1}}$ respectively) and largely diffusion controlled [16, 116].

Effect of the cation on aqueous phase OH yields

The aqueous phase yields showed no statistically significant difference for either the bulk liquid or the aerosol phase solutions, when experiments with lithium nitrate (set DD) and sodium nitrate (set DB) were compared for both phases. This contrasts with the results from the gas phase experiments, where the production of gas phase hydroxyl radical from irradiated nitrate aerosol was measured to be statistically higher for lithium nitrate (set CC) than for sodium nitrate (set CB)(see Table 6.8). These tests were conducted with Student's t test, with 95% confidence limits.

Effect of varying the nitrate concentrations

Sets DF, DG and DH formed a series where the concentration of nitrate was increased for each successive set while the benzoic acid concentrations were kept similar. The sets with higher concentrations of nitrate showed higher yields of *p*-HBA in the aerosol phase, although the increase was not directly proportional. Since the light that is being absorbed is a small fraction of the total, the relationship between lithium nitrate concentration and hydroxyl radical yield can be approximated as linear. Hence, the increase in hydroxyl radical yield is expected to be proportional to the increase in nitrate concentration when the path length is extremely short, as is the case in the aerosol phase. If the increased concentration is dampening any intensity enhancements, non-linear effects would result.

The increase in the bulk liquid *p*-HBA yields was lower than that seen for the aerosol phase, and there was no difference at all between the more concentrated sets DG and DH. This is in line with expectations; a solution of $0.1\,\mathrm{mol\,L^{-1}}$ sodium nitrate with a 1 cm path length will absorb 80% of the light, while a solution of $0.5\,\mathrm{mol\,L^{-1}}$ sodium nitrate also with a 1 cm path length will absorb 100% of the light. Therefore, the

concentrations of *p*-HBA measured for the $0.5\,\mathrm{mol\,L^{-1}}$ set (DG) should only be 1.25 times the $0.1\,\mathrm{mol\,L^{-1}}$ set (DF) and the $2\,\mathrm{mol\,L^{-1}}$ set (DH) should be similar to set DG. Within the limits of experimental uncertainty, this is indeed the case.

Overall the enhancement of hydroxyl radical yield in the aerosol is about ten times. Even in the aqueous phase a significant enhancement can result from a reduced cage effect, if the low yield of OH in the bulk liquid is due to the quenching of excited NO_3^- by solvent according to the reverse reaction of:

$$NO_3^- + h\nu \rightleftharpoons NO_3^{-*}, \tag{6.2}$$

which can otherwise dissociate to eventually generate hydroxyl radical:

$$\begin{aligned} NO_3^{-*} &\longrightarrow NO_2 + O^-, \\ O^- + H_2O &\longrightarrow OH^- + OH. \end{aligned} \tag{6.3}$$

6.4 Gas phase results

6.4.1 Carbon monoxide as the radical scavenger

For experiments with concentrated nitrate solutions and in the absence of the narrow band filter, it proved possible to measure the gas phase yield of carbon dioxide resulting from the reaction of carbon monoxide with hydroxyl radical. However, it is not possible to demonstrate unequivocally whether this yield is due to gas phase hydroxyl radical or whether the carbon monoxide has reacted within the droplets to generate carbon dioxide which has then diffused out into the gas phase because the lifetimes for diffusion and reaction are so similar (see Section 6.7). Table 6.8 summarises the gas phase experiments with carbon monoxide as the radical scavenger. The gas phase concentrations of carbon dioxide and hydroxyl radical, calculated as described in Section 4.1.4, are presented in units of $\mathrm{molecules\,cm^{-3}} \times 10^6$ and $\times 10^{13}$ respectively, along with their uncertainties. The hydroxyl radical concentration is the steady-state concentration, calculated assuming that the reactants are in the gas phase and that gas phase kinetics apply.

As expected, sodium chloride aerosols (set CA) did not produce an appreciable concentration of hydroxyl radical when irradiated. This ruled out the possibility that physical effects from warming (from the lamp) were responsible for the rise in carbon dioxide levels that had been measured with irradiated nitrate aerosols.

	solution ($M = mol\,L^{-1}$)	dielectric filter	$N^{\dagger}$	average [OH] ($molecules\,cm^{-3}\ \times 10^{6}$)	average [CO_2] ($molecules\,cm^{-3}\ \times 10^{13}$)
CA	2 M NaCl	no	3	1 ± 2	0.6 ± 1.2
CB	2 M $NaNO_3$	no	6	9.4 ± 0.9	4.1 ± 0.8
CC	2 M $LiNO_3$	no	9	10 ± 1	5.5 ± 0.5
CD	2 M $LiNO_3$ + 2 M NaCl	no	8	8 ± 1	4.9 ± 0.5
CE	5 M $LiNO_3$	no	27	16 ± 1	8.4 ± 0.4
CF	8 M $LiNO_3$	no	4	19 ± 1	10.0 ± 0.8
CG	5 M $LiNO_3$	yes	6	0.3 ± 0.6	0.2 ± 0.3

† N is the number of samples

Table 6.8: Results from gas phase experiments.

All solutions of $2\,mol\,L^{-1}$ NO_3^- produced similar concentrations of gas phase hydroxyl radical, whether they consisted of sodium nitrate, lithium nitrate or $2\,mol\,L^{-1}$ lithium nitrate plus $2\,mol\,L^{-1}$ sodium chloride (sets CB, CC and CD respectively). The concentrations measured for Set CC are slightly higher than Set CB; the cation does not appear to affect the yield of hydroxyl radical greatly, although it will affect the activity of the solution and hence the relative humidity. This in turn could affect the geometric mean droplet diameter, although the particle size distributions for lithium nitrate solutions showed no statistically significant change in geometric mean diameter when compared with those of sodium nitrate solutions of the same concentration.

The addition of sodium chloride to the $2\,mol\,L^{-1}$ $LiNO_3$ solution made no difference to the measured yield of hydroxyl radical. If nitrate ions are promoted to the surface in the presence of chloride ions, this result implies that the distribution of nitrate ions in the droplet does not affect the reaction with carbon monoxide. This is potential evidence that the reaction of hydroxyl radical with carbon monoxide is taking place within the droplet rather than the gas phase, since if the nitrate is near the surface the hydroxyl radical would have a greater chance of escaping to the gas phase. If the yield of carbon dioxide does not increase correspondingly, it indicates a largely bulk liquid-phase reaction.

If the lithium nitrate experimental sets (CC, CE and CF) are compared, it is clear that higher aqueous phase concentrations of lithium nitrate produced greater concentrations of hydroxyl radical in the gas phase. Again, the fraction of the light that is absorbed is small. As for the experiments with the aqueous phase scavenger, the concentration of

hydroxyl radical produced is not directly proportional to the concentration of nitrate, which implies that quenching effects are significant.

Effect of dielectric filter

Set CG of Table 6.8 was a repeat of set CE, also investigating $5\,\mathrm{mol\,L^{-1}}$ lithium nitrate solution, but in this case the dielectric narrow band filter was used to restrict the light to the wavelength of interest. Because the filter cut the total amount of light down considerably, there was insufficient irradiance to generate a detectable gas phase concentration of hydroxyl radical. This was unfortunate since it meant that the irradiance measured via actinometry did not correspond to the irradiance present in these gas phase scavenger experiments and therefore could not be used to directly calculate the quantum yield.

6.4.2 Comparison with aqueous phase scavenger experiments

The aqueous phase experiments resulted in measurements of OH in terms of rates; molecules formed per second. The inline measurements using the mass spectrometer were in terms of the partial pressure of carbon dioxide which was converted to a concentration. Since the volume of the chamber is accurately known, the gas phase results can be readily converted to a rate. Experimental set CB, with aerosol nebulised from $2\,$,$\mathrm{mol\,L^{-1}}$ nitrate solution, has a gas phase OH formation rate of $2.9\times10^{15}\,\mathrm{molecule\,s^{-1}}$. However, this cannot be directly compared with the results from the aqueous phase experiments, since the method of collection was completely different, necessitating a number-weighted aerosol absorption coefficient. If the aerosol absorption coefficient is factored in, the experiments can be compared via their quantum yields. The set CB has a quantum yield of 0.11 while the aqueous phase set DG has a quantum yield of 2.7×10^{-3} . Potential reasons for this difference are explored in Section 6.7.

A potential complication to the experiments with carbon monoxide as a scavenger is the subsequent reaction of the hydrogen atoms, produced when CO reacts with OH, with NO_2 produced in the photolysis of nitrate. Not only would this produce an extra hydroxyl radical, it would also prevent the photolysis products recombining in

the solvent cage:

$$\begin{aligned} CO + OH &\longrightarrow CO_2 + H, \\ NO_3^- + h\nu &\longrightarrow NO_2^- + O(^3P), \qquad (6.4) \\ H + NO_2 &\longrightarrow HONO, \qquad (6.5) \\ HONO + h\nu &\longrightarrow OH + NO. \qquad (6.6) \end{aligned}$$

The reaction of H with NO_2 is fast both in the gas phase and in aqueous solution. Both impacted aerosol and bulk liquid solutions of nitrate had a deep yellow colour after irradiation. This is attributable to nitrite production in an alternative primary process (see Equation (1.4)) [1].

Nitrite is produced directly from the photolysis of nitrate, at around 11% of the hydroxyl radical yield, but can also be formed from the reaction of the O^- radical with NO_2. Nitrous acid, the conjugate acid of the nitrite anion, has a pK_a of 3.37, so will only be present in the acidified HPLC analysis; the pH of irradiated bulk solutions was around 6. A distinct absorption band was observed at 360 nm in UV-visible spectra of irradiated solutions for both aerosol and bulk liquid phases. On close examination of the HPLC chromatographs, a small peak attributable to nitrous acid was seen at retention times of the order of 5.5 min.

6.4.3 Cyclohexane as the radical scavenger; inline detection of products

No decrease in the partial pressure of cyclohexane was observed for any of the systems investigated:

CH: $5\,\mathrm{mol\,L^{-1}}$ lithium nitrate
CI: $0.1\,\mathrm{mol\,L^{-1}}$ sodium nitrate
CJ: $1\,\mathrm{mol\,L^{-1}}$ sodium nitrate
CK: $8.5\,\mathrm{mol\,L^{-1}}$ lithium nitrate
CL: $2\,\mathrm{mol\,L^{-1}}$ sodium chloride
CM: $2\,\mathrm{mol\,L^{-1}}$ lithium nitrate + $2\,\mathrm{mol\,L^{-1}}$ sodium chloride

An estimate of the sensitivity was calculated by evaluating the standard deviation of stable, non-irradiated sections of the scans. An average of the standard deviations from

scavenger	compound	concentration produced in aerosol ($\mathrm{mol\,L^{-1}} \times 10^{-6}$)
benzene	phenol	5.1 ± 0.2
	para-nitrophenol	1.17 ± 0.06
	ortho-nitrophenol	0.39 ± 0.02
benzoic acid	*para*-hydroxybenzoic acid	200 ± 20

Table 6.9: Product yields from irradiated nitrate aerosol in the presence of benzene, with yield of *p*-HBA from nitrate/benzoic acid solution included for comparison.

four such sections was calculated to be 2.3 ppm. A stable rise due to irradiation from the lamp would have been marginally detectable at one standard deviation from the mean background, so 2.3 ppm can be considered an upper limit for the concentration of products (cyclohexanol and cyclohexanone) from the reaction of cyclohexane with the hydroxyl radical. This is above the levels measured in the carbon monoxide experiments, so does not convey any new information about the photolysis of nitrate.

6.5 Benzene as an aqueous phase radical scavenger

Benzene was not effective as a gas phase scavenger, because its Henry's law constant is high ($0.18\,\mathrm{mol\,L^{-1}\,atm^{-1}}$, 200 times higher than the Henry's law constant for carbon monoxide). Consequently, at chamber concentrations of 910 ppm, concentrations of benzene in the aqueous phase were $1.6\times10^{-4}\,\mathrm{mol\,L^{-1}}$. Table 6.9 lists the product compounds measured by HPLC analysis after irradiation of nitrate aerosol in the presence of benzene. One of the results from the nitrate/benzoic acid aerosol experiments is provided for a rough comparison; however, although the experimental conditions were in general the same, the concentration of nitrate was 2.5 times lower for the nitrate/benzoic acid experiment.

The presence of phenol, *para*-nitrophenol and *ortho*-nitrophenol in the irradiated aerosol samples is not surprising; these compounds are known to form from the reaction of benzene with hydroxyl radical in the presence of NO_2 [111]. More worthy of note, however, is the absence of nitrobenzene or *meta*-nitrophenol. Nitrobenzene would be expected to be formed in much higher yields than any of the nitrophenol isomers [117]. Nitrobenzene also has a relatively high vapour pressure. Benzene, which is very volatile,

was also absent. *Meta*-nitrophenol is formed by hydroxylation of nitrobenzene [111], so if nitrobenzene is either not formed or escapes quickly, this explains the absence of *meta*-nitrophenol.

6.6 Physical processing of the aerosol droplets

Natural aerosols are constantly growing or shrinking in particle diameter, as the ambient conditions change [5]. The most important factor in the rate of change in particle diameter is the relative humidity (RH), as mentioned in Section 1.2.4. In this experiment, the carrier gas had been humidified before entering the chamber. Because of the difference in pressure between the inlet tube and the nebuliser, the gas was not fully saturated when it entered the chamber, but was saturated to around 40 to 50%. Once the solution was admitted into the nebuliser, the relative humidity would increase as the nebuliser started to produce aerosols. This is typical of the Collison nebuliser (jet nebuliser). For dilute solutions, the gas would have become saturated with water in the nebuliser [118].

After solution had been introduced to the nebuliser, the relative humidity, as measured by the Vaisala probe, rose quickly, reaching a maximum value after about 10 minutes. After 10 or so minutes the relative humidity was at a maximum. The value of this maximum depended on the activity of the water in the solution, which depended on the identities and concentrations of the solutes. For a dilute solution ($0.1\,\mathrm{mol\,L^{-1}}$) of lithium nitrate, a maximum relative humidity of 90% was typical. For saturated solutions ($8\,\mathrm{mol\,L^{-1}}$) the maximum RH observed was 50%.

If the density of the solution is known, the activity of the water can be calculated from the molality of the solution. For example, a typical lithium nitrate solution with an initial concentration of $2.1\,\mathrm{mol\,L^{-1}}$ had a molality of $2.2\,\mathrm{mol\,kg^{-1}}$ [119], corresponding to an activity coefficient for water of 0.90 and hence an expected RH of 90%. The maximum measured RH for such solutions was 72%. This implies the solution has evaporated considerably and the particles in actual fact had a molality of $6.7\,\mathrm{mol\,kg^{-1}}$. A more concentrated solution of lithium nitrate, with a concentration of $5.5\,\mathrm{mol\,L^{-1}}$, had an initial molality of $6.6\,\mathrm{mol\,kg^{-1}}$ and an expected RH of 70%. The measured maximum RH was 58%. Such changes in the aerosol would affect the absorption coefficient and hence b_{abs}. However, the aerosol size distributions showed no significant change in particle diameter between the top and bottom of the chamber; b_{abs} was calculated from

the measured distributions. Therefore, as explained in Section 2.9.4, the change in relative humidity was most likely related to the rise in temperature, rather than a change in the partial pressure of water.

6.7 Comparison of radical scavenger systems

6.7.1 Cyclohexane compared with carbon monoxide

Both cyclohexane and carbon monoxide react rapidly with hydroxyl radical, with gas phase rates of 7.49×10^{-12} and $2.24\times10^{-13}\,\mathrm{cm^3\,molecule^{-1}\,s^{-1}}$ respectively [105, 120]. Both have been used for this thesis and elsewhere as radical scavengers. A comparison here is not possible because the limits of detection of the mass spectrometer are much higher for cyclohexane than carbon monoxide. The decrease in cyclohexane concentrations during irradiation was less than 2.3 ppm, which tells us little since the increase in carbon dioxide was of the order of 1 ppm.

Cyclohexane and carbon monoxide are both fairly insoluble in water. Carbon monoxide, with a Henry's law constant of $9.5\times10^{-4}\,\mathrm{mol\,L^{-1}\,atm^{-1}}$, is even less soluble than cyclohexane ($H_B = 5.6\times10^{-3}\,\mathrm{mol\,L^{-1}\,atm^{-1}}$). However, the gas phase concentrations of carbon monoxide used were high enough to ensure significant aqueous phase concentrations of carbon monoxide, relative to the concentration of hydroxyl radical produced. At concentrations of 2%, the aqueous phase concentration of CO would have been $2\times10^{-5}\,\mathrm{mol\,L^{-1}}$. The rate constant for the reaction of CO with OH in aqueous solution is $2\times10^{9}\,\mathrm{mol\,L^{-1}\,s^{-1}}$ [121], which corresponds to a mean OH lifetime of 2.5×10^{-5} s. The characteristic time of diffusion of hydroxyl radical from the middle of the droplet to its surface is of the order of $\frac{r_p^2}{\pi^2 D_{aq}}$ where D_{aq} is 2.2×10^{-5} [16] and d_p is about 1×10^{-4}cm, so the mean diffusion time would be on the order of 1×10^{-5} s (see Section 1.6.2). Hence, a significant fraction of the carbon dioxide observed would have been produced in the aqueous phase[1]. Hydroxyl radical generated directly at the surface might well appear with markedly higher quantum yield because of a reduced solvent cage effect, but it is otherwise indistinguishable from OH generated within the droplet.

The background level of gas phase CO_2 was low when purified CO was used. Any CO_2 formed in the droplets would have left the droplets, since the characteristic time

[1] This would also have been true for the reaction of cyclohexane with OH.

of diffusion within the droplet (and hence the characteristic time for diffusion to the interface) is also on the order of 1×10^{-5} s, for droplets with $d_p = 1\,\mu\text{m}^2$.

The hypothesis that the escape of the hydroxyl radical to the gas phase would be facilitated by the proximity of the hydroxyl radical to the surface of the droplet cannot be proven or disproven with gas phase scavengers, given that one of the least soluble scavengers available was still soluble enough to react in appreciable amounts with the hydroxyl radical within the droplet. However, in an indirect sense, the hypothesis is supported: the small size of the droplets not only allows rapid diffusion of any radical formed within to the interface, but also allows rapid uptake of even insoluble gases into the liquid phase; thus hydroxyl radical produced within aerosol droplets can have a marked influence on the chemistry on the gas phase.

6.7.2 Relative yields in the gas and aqueous phases

The aqueous scavenger experiments used benzoic acid concentrations far higher than other nitrate-aqueous scavenger experiments reported in the literature [4], although the ratio of nitrate to benzoic acid was comparable to that used in previous experiments. Attempts to use lower concentrations of benzoic acid resulted in the concentrations of products being below the limit of detection in the HPLC analysis.

In spite of this difference, the quantum yields were calculated based on the bulk liquid experiments, so they are internally consistent, even though the quantum yields of *p*-HBA are not similar to the literature values. The quantum yields for the aqueous phase and gas phase radical scavenger experiments for both bulk liquid and aerosol phases are compiled in Table 6.10. It is likely that the distributions of the nitrate anion and benzoic acid within the aerosol droplets are not homogeneous. Nitrate is believed to favour the bulk liquid over the surface [53, 55], with enhanced concentration in a layer 0.3 nm below the surface, while the sparingly soluble benzoic acid is expected to favour the surface.

The high quantum yield of OH from the gas phase radical scavenger experiments, relative to the aqueous phase scavenger experiments, is most likely due to secondary reactions in the aqueous phase. If the yield of *p*-HBA from the scavenging of OH by benzoic acid is 1.8%, then the OH quantum yield for the aqueous phase scavenger experiments

[2]The diffusion coefficient for carbon dioxide in water is $2.35\times10^{-5}\,\text{cm}^2\,\text{s}^{-1}$ [122].

Aerosol					
chemical	concentration ($\mathrm{mol\,L^{-1}}$)	filters	product	yield ($\mathrm{molecule\,s^{-1}}$)	quantum yield[†]
FeOx	0.05	ND, dielectric	Fe^{2+}	3.0×10^{14}	32
$NaNO_3$/BA	0.1	dielectric	*p*-HBA	1.6×10^{10}	2.7×10^{-3}
$NaNO_3$/BA	0.1	none	*p*-HBA	2.2×10^{12}	2.7×10^{-3}
$NaNO_3$/BA	2.0	none	*p*-HBA	1.4×10^{13}	9.1×10^{-5}
$NaNO_3$/CO	2.0	none	CO_2	2.9×10^{15}	0.11[*]
Bulk liquid					
chemical	concentration ($\mathrm{mol\,L^{-1}}$)	filters	product	yield ($\mathrm{molecule\,s^{-1}}$)	quantum yield
FeOx	0.05	ND, dielectric	Fe^{2+}	3.8×10^{15}	1.24
$NaNO_3$/BA	0.1	dielectric	*p*-HBA	7.8×10^{13}	3.0×10^{-4}

[†] The irradiance has been adjusted for the effect of the dielectric filter, which was calculated from the ratio of the yields from the dilute sodium nitrate experiments. Thus the quantum yields for these two experiments have identical quantum yields.
[*] This is the quantum yield for OH and hence is not directly comparable to the *p*-HBA yields quoted here.

Table 6.10: A compilation of the results from actinometry and radical scavenging experiments.

is 5.1×10^{-3} compared with 0.11 in for the gas phase scavenger experiments. Hydrogen atoms formed in the aqueous phase from the reaction of OH with carbon monoxide can react with the nitrogen dioxide produced in the alternative decomposition pathway of the nitrate anion (Equation (6.5)). The alternative explanation for the increased gas phase yields is that the aqueous phase scavenger is not reacting with all the hydroxyl radical and some is indeed escaping to the gas phase. However, the concentrations of benzoic acid were such that it is unlikely that much OH could escape to the gas phase. This is backed up by the fact that the concentration of benzoic acid did not affect the yield of *p*-HBA.

It should be noted that the number-weighted particle size distributions used to calculate the aerosol absorption coefficient for the gas phase scavenger system will give, appropriately, a higher weighting to the very small droplets, for which surface effects are likely to be the most important.

The product yields from the gas phase reaction of benzene with OH are limited, because the benzene-OH adduct formed decomposes thermally with a lifetime of about 0.3 s [107]. The vast majority of the phenol produced will have been produced in the aqueous phase, and the small amount detected would have diffused out of the droplets to the gas phase.

6.8 Experimental limitations

During the course of this experiment, many instrumental and physical limitations became apparent. Measuring the ratio of reactions in aerosol droplets to the reactions in the gas phase was never going to be easy. The gas phase hydroxyl radical yield is small, and it was only by pushing several instruments beyond their manufacturers' recommendations that any results could be obtained.

The Residual Gas Analyser (RGA), in particular, is not designed to be used at such high pressures. Only by turning the high pressure protection for the EM off was it possible to measure the rise in carbon dioxide levels. The range of the spectrometer is limited to five orders of magnitude, but by using isotopic ratios it proved possible to calculate the total pressure even when it was outside the range of the RGA.

The particle concentrations were far beyond the limit of what the Aerodynamic Particle Sizer could measure. Even with the dilution system, the concentrations could only be

estimated by extrapolation from extreme levels of dilution that introduced considerable uncertainty into the measurement. The particle size distributions were also at the lower limit of what the APS could measure. This resulted in some truncation of the data in all cases and in about 10% of cases, the truncation was severe enough to prevent a meaningful estimate of the geometric mean particle diameter.

The amount of material in the chamber at any one time was dictated by the flow rates of the gases entering the chamber and the size of the chamber. Even at the highest concentrations of aerosol, 300 000 particles per cubic centimetre, there was only $5\times10^{-5}\,\mathrm{cm}^3$ of liquid per cubic centimetre. That is, the chamber contained a maximum of 50 ppmv* sodium nitrate solution during an experiment. This is very little material to collect and analyse, although it is an extremely concentrated aerosol by atmospheric standards. A typical coarse-mode urban aerosol would have a concentration of around 0.03 ppmv of particles in the coarse mode (that is, around $6\,\mu$m in diameter) and a similar concentration in the fine mode, at around 0.04 ppmv.

A larger chamber with a slower-moving aerosol inside it would make detection and quantification of the products far easier. Large chambers tend to be built out of Teflon bags which have their own problems: permeability to gas, electrostatic charges which attract aerosol particles, and transparency to ultraviolet and visible light.

The mercury-xenon lamp provided light intensities high enough to generate measurable yields of products for some of the systems investigated. However, the uncertainties in its ultraviolet spectrum meant that it was unsuitable for actinometry (or any investigation that requires light of well defined wavelengths) and it would have been better to have replaced the xenon arc lamp with a more powerful xenon arc lamp.

6.9 Future work

A first step to improving the methods used in this thesis would be to replace the lamp with a lamp with a better-defined spectral output. This, combined with careful steps to limit side reactions in the ferrioxalate for both aerosol and bulk liquid phases might produce more consistent results.

Given the rapid uptake of gases of very low solubility into the aerosol droplets, the

*ppmv = parts per million by volume.

gas phase system is not useful for measuring gas phase yields of hydroxyl radical in a multiphase system. A more extensive characterisation of the reactions of aqueous phase scavengers in aerosols over a greater range of concentrations may bridge this gap. Also, the uptake of gas phase benzene to react in the aqueous phase to form detectable products has potential as a method for investigating the ability of aqueous phase reactions to produce secondary organic aerosol.

Chapter 7

Conclusion

Enhanced rates of production of hydroxyl radical were observed in aerosol phase sodium nitrate. These enhancements cannot be explained by Mie theory alone. The high yields may be in part a result of the correspondence of regions of high nitrate concentration with regions in the droplets where the light intensity is dramatically enhanced, *i.e.*, near the surface. The even greater enhancement of photoreduction of potassium ferrioxalate may be due to its surface preference. It is a large, polarisable anion and as such would be expected to be found on or near the surface of a droplet.

7.1 Techniques used

This thesis features a direct application of actinometry to an aerosol system; this is the first time this technique has been used with a degree of success. The potassium ferrioxalate actinometer, used carefully, is a sensitive measure of irradiance. However, the high quantum yield of the actinometer (1.24) compared with that of hydroxyl radical from nitrate (0.017) makes it impossible to compare results under the same conditions of illumination; hence the use of filters. The largest obstacle to a direct determination of intensity enhancements within the aerosol droplets was the uncertainties surrounding the spectrum from the lamp, in addition to the difficulty of defining a pathlength for a sub-micron sized droplet. Using results from Mie theory to produce aerosol absorption coefficients did not solve this problem as neither the particle size distribution of the aerosol or the magnitude of k, the imaginary component of the index of refraction, was properly characterised. Measurements of k for aerosols have yielded values considerably (orders of magnitude) higher than would be expected from the optical density. This points to the failure of Mie theory to account for non-linear optical effects.

Aerosol actinometry has not been well studied and is subject to complications due to the materials of the system. The irradiance in the chamber was measured with bulk solutions of potassium ferrioxalate. This measurement, combined with the relative yields and the relative aerosol absorption coefficients of the ferrioxalate and nitrate/benzoic acid aqueous aerosol systems, allowed a comparison of the enhancements in the bulk liquid phase of aqueous nitrate aerosol.

The use of HPLC for offline analysis of collected aerosol samples proved an effective method for both qualification (for the experiments with benzene as scavenger) and quantification (for the experiments with benzoic acid as scavenger) although the sensitivity of this technique could be usefully improved.

The use of radical scavengers has also been well documented but, while they have been used in gas phase reactions between ozone and VOC which produce secondary aerosol, there are few reports in the literature documenting their use to measure hydroxyl radical production from aqueous aerosol. There are good reasons for this: the applicability of even the most insoluble gas as a radical scavenger is limited since enough will be taken up by the aerosol droplets to obscure the measurement of gas phase radical. Aqueous scavengers, meanwhile, only yield information about the reaction in the aqueous phase. The chemistry of the aqueous phase can be investigated just as effectively with bulk solutions; however, the observed enhancements suggest that reactions in aqueous aerosols deserve further study.

7.2 Summary of results

Standard chemical actinometry was performed for both aerosols and bulk liquid solutions of potassium ferrioxalate. For bulk liquid solutions of 0.05 and 0.15 $\mathrm{mol\,L^{-1}}$ ferrioxalate the radiant flux was measured to be $(2.7 \pm 0.4) \times 10^{15}$ $\mathrm{quanta\,s^{-1}}$ for a bulk liquid solution of pathlength 1 cm in a Petri dish positioned halfway down the reaction chamber. The absorbance of the system was such that all light was absorbed.

A quantum yield of *para*-hydroxybenzoic acid of $(3.0 \pm 0.9) \times 10^{-4}$ was calculated from measurements from bulk aqueous nitrate solutions. Using this value and the calculated value of b_{abs} from the ferrioxalate aerosol actinometry, effective aerosol quantum yields of hydroxyl radical of 2.7×10^{-3} and 9.1×10^{-5} were calculated for dilute nitrate aerosol

and concentrated nitrate aerosol respectively. While the quantum yield is high for the dilute aerosol, these enhancements are lower than seen for the actinometer. This is probably due to a different radial distribution of these chemicals within the droplets; that is, the ferrioxalate is likely to reside at the surface.

The measured gas phase yield of carbon dioxide, and hence total hydroxyl radical, was $(4.1 \pm 0.9) \times 10^{13}$ molecules cm^{-3} for 2 mol L^{-1} solutions of sodium nitrate, or $(2.9 \pm 1.0) \times 10^{15}$ molecules s^{-1}. This was somewhat higher than that calculated for the production of aqueous hydroxyl radical.

Production of hydroxyl radical in the aqueous aerosol was observed. A gas phase yield of carbon dioxide was measured, but due to the fast uptake and outgassing of the species concerned in aerosols of micrometre-sized droplets, whether this carbon dioxide formed in a gas phase reaction or whether it formed in an aqueous phase reaction cannot be directly determined.

The ferrioxalate quantum yield was significantly enhanced in the aerosol. Most of this enhancement would have reflected an actual increase in the amount of light to which the ferrioxalate was exposed. The yield of hydroxyl radical was also enhanced in the aerosol. The surfactant properties of nitrate are so different from those of the ferrioxalate that it is not possible to say how much of this enhancement is genuine.

Appendix A

Aerosol smog chamber experiments at the University of California, Irvine

The University of California, Irvine campus, has a strong atmospheric chemistry section. Under the leadership of Professor Barbara J. Finlayson-Pitts, the AirUCI institute has been set up to provide a platform for the atmospheric chemistry research groups to combine ideas and expertise, not only within the Irvine campus but also internationally, with links to groups doing similar research in the Czech Republic and New Zealand.

Academic and student exchanges are a key part of the AirUCI philosophy. The work presented in this chapter was undertaken during a three month exchange by the author to the Irvine campus, from January to April, 2006. The research was conducted jointly with Huda Shaka', a graduate student at UC Irvine, supervised by Professor B. J. Finlayson-Pitts.

A.1 Sulfur dioxide and marine aerosol

Nitrogen oxides are not the only pollutants to react with marine aerosol. Sulfur dioxide will also react with sea salt aerosol, being oxidised to form sulfate particles. There are other routes to atmospheric sulfate (for example, the reaction of hydroxyl radical with sulfur dioxide) but the vast majority of these involve some form of oxidation of sulfur dioxide. Sources of sulfur dioxide include the burning of fossil fuels and industrial emissions as well as natural sources: volcanoes and the oxidation of dimethylsulfide, which is produced by phytoplankton [123].

Deliquesced sea salt aerosol and mineral dust aerosol are important sites for sulfate production [123]. Dissolved sulfur dioxide forms a hydrate which will dissociate to form

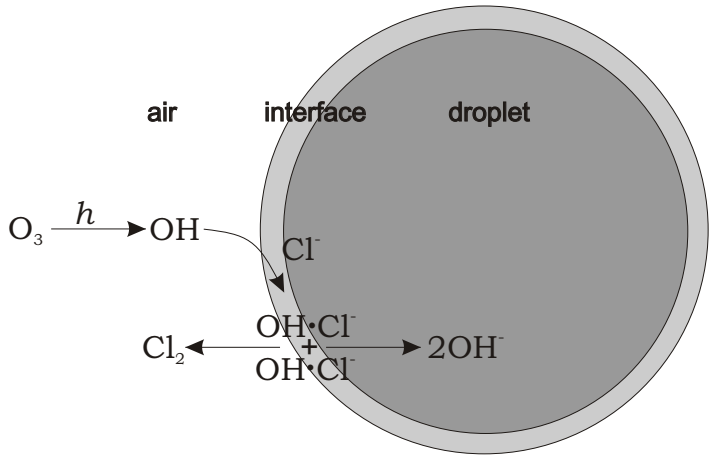

Figure A.1: Hydroxyl radical reacts with chloride ions at the interface to form Cl_2 and OH^-. Adapted from [103].

bisulfite and sulfite ions [14]:

$$SO_2 \cdot H_2O \rightleftharpoons HSO_3^- + H^+ \rightleftharpoons SO_3^{2-} + 2H^+. \tag{A.1}$$

These species share an oxidation level of four, and are known collectively as S(IV). S(IV) can be oxidised to S(VI): sulfate/sulfuric acid, which has its own aqueous equilibria:

$$H_2SO_4 \rightleftharpoons HSO_4^- + H^+ \rightleftharpoons SO_4^{2-} + 2H^+. \tag{A.2}$$

Previous studies, including both experimental studies and molecular dynamics modelling, have investigated the reactions of NaCl particles exposed to ozone and hydroxyl radical. NaCl particles which have been exposed to hydroxyl radical show reaction products under scanning electron microscopy (SEM) [124]. SEM with energy-dispersed analysis of X-rays (SEM-EDX) revealed an increase in the levels of oxygen after treatment but a decrease in the chlorine levels. One possible mechanism involves gas phase hydroxyl radical adsorbing onto the liquid interface where it forms a transition complex with Cl^- ions. This species reacts with a neighbouring complex to produce gas phase Cl_2 and aqueous OH^- (see Figure A.1) [30, 103]. An alternative possibility is that the $OH{\cdot}Cl^-$ complex may react with Cl^-. The outcome of these processes is that not only is Cl_2 formed, but also that the alkalinity of the particles will increase.

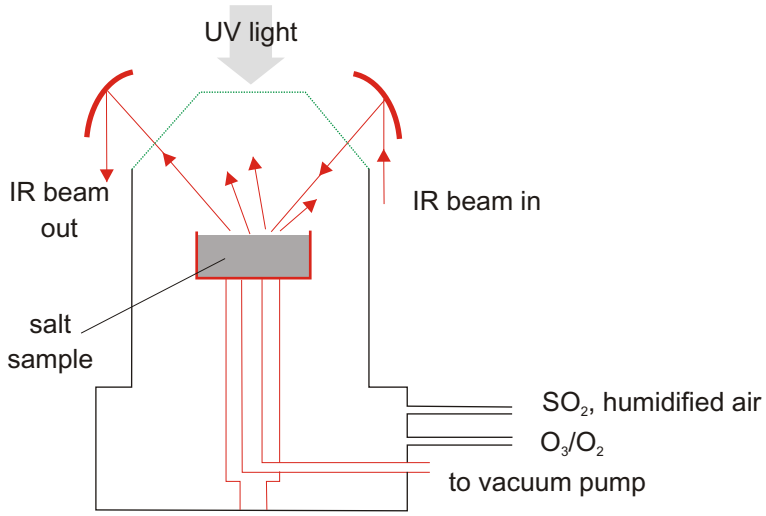

Figure A.2: A schematic of the DRIFTS cell used by Shaka' *et al.*. Adapted from [125].

A.2 Previous DRIFTS experiments

Recent Diffuse Reflectance Infrared Fourier Transform Spectroscopy (DRIFTS) experiments conducted by Shaka' in the Finlayson-Pitts laboratory showed that the products formed from the reaction of NaCl with OH would oxidise adsorbed sulfur dioxide to sulfate while increasing the alkalinity of the system[125]. If the pH of the sea salt aerosol is rising as it is processed, more SO_2 will be taken up due to the sulfite equilibria (Equation (A.1)).

A.2.1 DRIFTS cell

A DRIFTS cell comprises chiefly of a sample holder surrounded by an off-axis parabolic mirror (Figure A.2). The sample holder is filled with a powdered solid, such as sodium chloride. The gas flow rates into and out of the cell can be controlled. Infrared light from an FTIR spectrometer is directed at the sample surface. The random alignment of the powdered crystals reflects diffuse light around the cell. This is collected by the parabolic mirror and reflected in a collimated beam to an infrared detector. If the reactant sample is transparent to infrared light, any products that absorb in the IR region can be measured [15].

A.2.2 Investigation by Shaka' into the uptake and reaction of sulfur dioxide on deliquesced salts

Mixtures of sodium chloride and magnesium chloride in a DRIFTS cell were first exposed to ozone under ultraviolet light. Magnesium chloride has a lower deliquescence point than sodium chloride. Having a mixture of the two, with an intermediate deliquescence point, meant that the experiments could be conducted at convenient relative humidities.

The hydroxyl radicals generated by photolysis of the ozone adsorbed to the surface of the deliquesced salts and reacted with the chloride ions (as illustrated in Figure A.1):

$$\begin{aligned} O_3 + h\nu &\longrightarrow O_2 + O(^1D), \\ O(^1D) + H_2O &\longrightarrow 2OH, \\ OH + Cl^- &\xrightarrow{surface} Cl_2 + OH^-. \end{aligned} \tag{A.3}$$

After this pretreatment, once the system had been purged of ozone, sulfur dioxide was admitted to the cell.

Analysis of the infrared DRIFTS spectra revealed that the sulfur dioxide had indeed been taken up by the deliquesced sample and oxidised to sulfate. The oxidant was thought to be hypochlorous acid (HOCl), an end product of the OH-Cl^- reaction [125, 126]:

$$Cl_2 + OH^- \rightarrow HOCl + Cl^-. \tag{A.4}$$

Ozone and hydrogen peroxide, both potential oxidants that could have been present after the pretreatment of the salt sample, were ruled out on the basis that further irradiation by UV light after the pretreatment (with the O_3 flow off) did not cause any extra oxidation. Both species form the hydroxyl radical on photolysis, so it would be expected that further irradiation would increase the amount of oxidation if these species were present. HOCl has been previously proposed as an oxidant of S(IV) compounds [123, 126].

A.3 Uptake and processing of sulfur dioxide on NaCl aerosol

A.3.1 Instrumentation

The next step was to measure the potential for sulfur dioxide uptake and oxidation in sea salt aerosol. This took place in a 102 L chamber with White cell optics for infrared

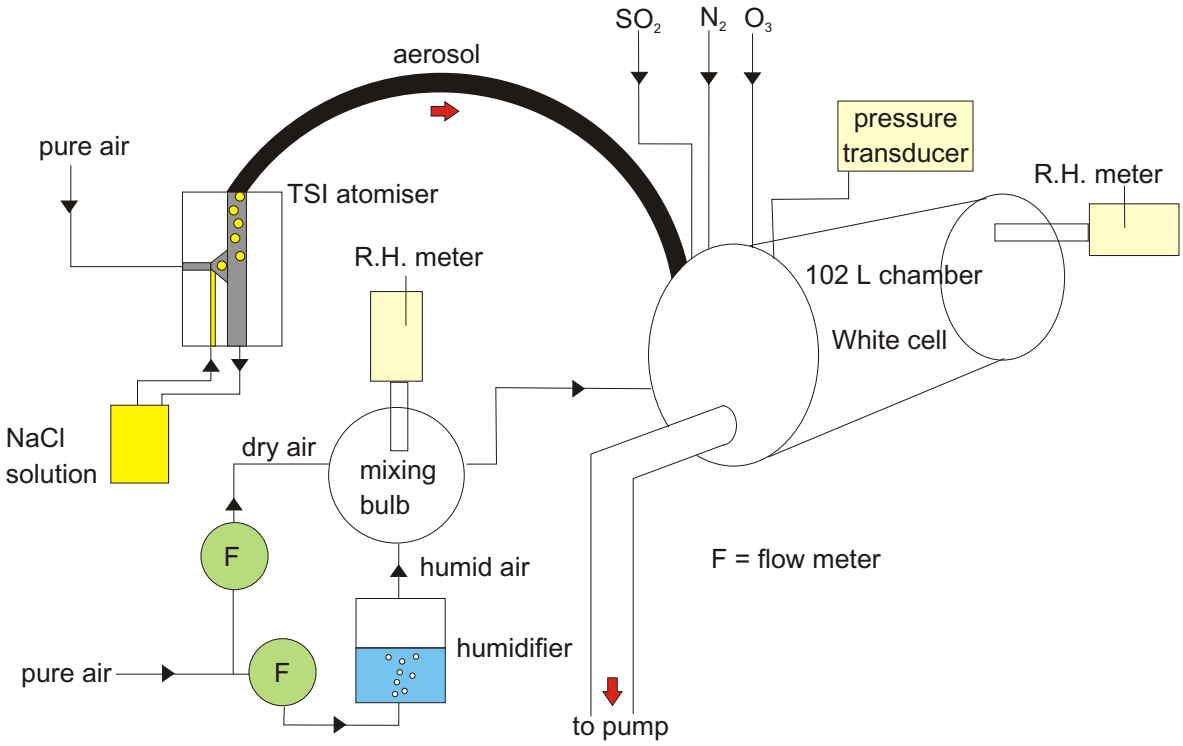

Figure A.3: The aerosol smog chamber in the Finlayson-Pitts laboratory at UC, Irvine. White cell optics and FTIR optics have been omitted for clarity.

spectroscopy (Figure A.3). This system was designed and built by previous members of the Finlayson-Pitts research group [70]. The chamber was made of a tube of borosilicate glass 300 mm in diameter and 1.2 m in length, with stainless steel endplates. For the White cell, gold mirrors were mounted on the end plates, 1.25 m apart. The endplates and the mirror mounts were coated in halocarbon wax to minimise adsorbance of the species of interest on the surfaces in the chamber.

A borosilicate glass tube inserted down the axis of the chamber for its entire length allowed a low pressure mercury lamp (GE, 30 W, G30T8) to be inserted down the axis of the chamber.

The FTIR (Fourier Transform Infrared) spectrometer used was a ThermoNicolet Nexus 670 IR spectrometer. The infrared beam from the spectrometer entered the chamber via a ZnSe window and was reflected along the length of the chamber a total of 38 times before exiting the chamber via the same window, resulting in a total path length of 47.5 m. It was detected by an external liquid nitrogen cooled mercury cadmium

telluride (MCT) detector.

A.3.2 Calibration of long path cell

To ensure the White cell optics were aligned correctly, the path length of the chamber was determined by calibration with methane. A measured amount of methane was admitted into the chamber, which was then filled to around atmospheric pressure with pure air. Five FTIR spectra were then taken of the contents of the chamber. About 40% of the contents of the chamber would then be evacuated and replaced by pure air, thus lowering the concentration of methane by around 40%. The ratio of the evacuated chamber pressure to the pressure of the refilled chamber was used to calculate the new concentration of methane.

This procedure was repeated six or seven times. This gave a range of methane concentrations with five spectra at each concentration. The spectra were analysed by integrating over the methane P Q and R infrared absorption bands at $3\,000\,\mathrm{cm}^{-1}$. Measured cross sections were plotted against standard data from the US Environmental Protection Agency (EPA) database [127]. This procedure generated linear calibration plots and allowed the calculation of the White cell path length. However, the path length of the cell varied considerably between calibrations, because the optics of the cell were moving into and out of alignment as the pressure in the cell changed. This problem was not solved during my stay in the laboratory.

A.3.3 Experimental procedure

Humidified pure air was admitted into the previously evacuated chamber up to a pressure of around 300 Torr. Sodium chloride aerosol generated by a Collison nebuliser[1] (TSI Atomiser 3076) was then admitted carefully into the chamber. This was a difficult operation as the valve could not simply be opened fully as the drop in pressure would result in the sodium chloride solution being sucked into the chamber. However, ideally the aerosol flow path would be free of sudden constrictions. Furthermore, the nebuliser only works properly at atmospheric pressures.

After the aerosol had been admitted, the chamber pressure would be around 500 Torr. Ozone was then admitted into the chamber and the mercury lamp turned on. After

[1] See Figure 2.3 for a general schematic of such a nebuliser.

irradiation, the chamber was left for several minutes. The concentration of ozone present in the chamber could be monitored via FTIR spectrometry. Sulfur dioxide was then admitted into the chamber, at concentrations such that the final concentration would be around 5×10^{14} molecules cm^{-3}. Following the introduction of sulfur dioxide to the chamber, FTIR spectra were measured for 10 minutes. At the scan rate chosen, this resulted in a total of 5 spectra. The FTIR spectra of pure sulfur dioxide and ozone were also measured.

A.4 Analysis and results

From the ThermoNicolet software, the FTIR spectra were exported into Microsoft Excel where they were easy to manipulate. The ThermoNicolet software also has a user-friendly graphical interface for data manipulation. Before any conclusions could be made about the presence of sulfite or sulfate peaks, the peaks due to ozone and sulfur dioxide had to be subtracted from the aerosol spectra. This was straightforward, since both species had well defined peaks at wavelengths that did not overlap the sulfate/sulfite region. Since the measured spectrum was a linear combination of the spectra of the individual species, it was possible to subtract spectra of known species, leaving just the unknown species. Hence, the spectrum of sulfur dioxide was multiplied by a constant and subtracted from the aerosol spectrum. The constant was chosen so that the well defined sulfur dioxide peaks at $2\,500\,\mathrm{cm}^{-1}$ were cancelled out. A similar procedure was followed for ozone.

Figure A.4 shows infrared spectra obtained for sodium chloride aerosol that has been exposed to sulfur dioxide and for the same aerosol having been further exposed to ozone. Spectrum (a) is the infrared spectrum of pure sulfur dioxide. Peaks due to sulfur dioxide are also apparent in (b), a spectrum from NaCl aerosol that has been treated with SO_2. Spectrum (c) shows no features attributable to sulfur (IV) or sulfur (VI); the only peaks are those due to ozone, between $1\,000$ and $1\,070\,\mathrm{cm}^{-1}$. Sulfate has a peak at $1\,100\,\mathrm{cm}^{-1}$ while sulfite has a peak at $950\,\mathrm{cm}^{-1}$. Neither is apparent in either of the spectra from the NaCl aerosol in Figure A.4. These peaks had been observed by Shaka' during the DRIFTS experiments [125]. Although no conclusive evidence for sulfate or sulfite aerosol was observed before the end of my involvement in April 2006, later experiments by Shaka' did provide qualitative evidence of sulfate formation.

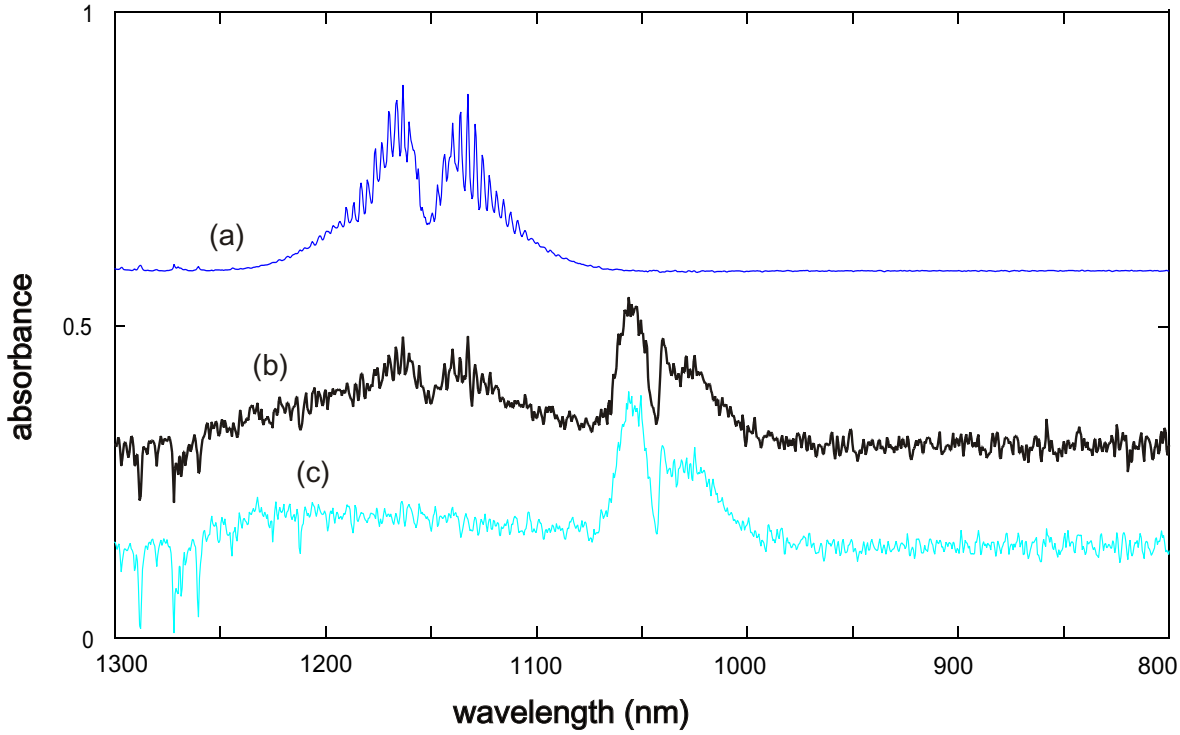

Figure A.4: Spectra obtained from NaCl aerosol: (a) pure SO_2, (b) NaCl aerosol treated with SO_2, (c) the same aerosol after further exposure to O_3.

References

[1] J. Mack and J. R. Bolton, *Journal of Photochemistry and Photobiology A: Chemistry*, 1999, **128**, 1–13.

[2] B. Mayer and S. Madronich, *Atmospheric Chemistry and Physics*, 2004, **4**, 2241–2250.

[3] P. Nissenson, C. J. H. Knox, B. J. Finlayson-Pitts, L. F. Phillips, and D. Dabdub, *Physical Chemistry Chemical Physics*, 2006, **8**, 4700–10.

[4] L. Chu and C. Anastasio, *Journal of Physical Chemistry*, 2003, **107**, 9594–9602.

[5] E. R. Gibson, P. K. Hudson, and V. H. Grassian, *Journal of Physical Chemistry A*, 2006, **110**, 11785–11799.

[6] L. B. Lave and E. P. Seskin, *Journal of the Americal Statistical Association*, 1973, **68**(342), 284–290.

[7] L. D. Claxton, P. P. Matthews, and S. H. Warren, *Mutation Research*, 2004, **567**(2-3), 347–399.

[8] P. B. Shepson, T. E. Kleindienst, E. O. Edney, G. R. Namie, J. H. Pittman, L. T. Cupitt, and L. D. Claxton, *Environmental Science and Technology 1985, 19, 249-255*, 1985, **19**, 249–255.

[9] M. S. Goldberg, R. T. Burnett, J. Brook, J. C. Bailar, M. F. Valois, and R. Vincent, *American Journal of Epidemiology*, 2001, **154**(9), 817–826.

[10] Ministry for the Environment, Health effects of PM_{10} in New Zealand: Air quality Technical Report 39, Ministry for the Environment, Wellington NZ, 2003.

[11] Environmental Protection Agency, *Federal Register*, 2006, **71**(200), 61144.

[12] R. J. Griffin, J. Chen, K. Carmody, S. Vutukuru, and D. Dabdub, *Journal of Geophysical Research*, 2007, **112**(D10), S17.

[13] J. H. Seinfeld and S. N. Pandis, *Atmospheric Chemistry and Physics: From Air Pollution to Climate Change*, John Wiley and Sons, Inc., New York, 1998.

[14] P. Warneck, *Chemistry of the natural atmosphere*, Vol. 71 of *International Geophysics Series*, Academic Press, San Diego, 2nd ed., 1999.

[15] B. J. Finlayson-Pitts and J. N. Pitts, *Chemistry of the Upper and Lower Atmosphere: Theory, Experiments and Applications*, Academic Press, San Diego, CA, 2000.

[16] G. V. Buxton, C. C. Greenstock, W. P. Helman, and A. B. Ross, *Journal of Physical and Chemical Reference Data*, 1988, **17**(2), 513–886.

[17] G. Mark, H.-G. Korth, H.-P. Schuchmann, and C. von Sonntag, *Journal of Photochemistry and Photobiology A: Chemistry*, 1996, **101**, 89–103.

[18] P. Warneck, *Berichte der Bunsen-Gesellschaft*, 1992, **96**(3), 454–460.

[19] M. Exner, H. Herrmann, and R. Zellner, *Berichte der Bunsen-Gesellschaft*, 1992, **96**(3), 470–477.

[20] T. Arakaki and B. C. Faust, *Journal of Geophysical Research - Atmospheres*, 1998, **103**(D3), 3487–3504.

[21] Y. G. Zuo and Y. W. Deng, *Chemosphere*, 1998, **36**(1), 181–188.

[22] D. E. Kinnison, K. E. Grant, P. S. Connell, and D. A. Rotman, *Journal of Geophysical Research, [Atmospheres]*, 1994, **99**(D12), 25705–25731.

[23] W. Guelle, M. Schulz, and Y. Balkanski, *Journal of Geophysical Research, Atmospheres*, 2001, **106**(D21), 27509–27524.

[24] C. Zdanowicz, G. Hall, J. Vaive, Y. Amelin, J. Percival, I. Girard, P. Biscaye, and A. Bory, *Geochimica et Cosmochimica Acta*, 2006, **70**(14), 3493–3507.

[25] H. J. Hwang and C. U. Ro, *Journal of Geophysical Research, Atmospheres*, 2005, **110**(D23).

[26] S. Seisel, C. Borensen, R. Vogt, and R. Zellner, *Physical Chemistry Chemical Physics*, 2004, **6**(24), 5498–5508.

[27] C. R. Usher, A. E. Michel, and V. H. Grassian, *Chemical Reviews*, 2003, **103**, 4883–4939.

[28] E. R. Lewis and S. E. Schwartz, *Sea salt aerosol production: mechanisms, methods, measurements and models - a critical review*, Vol. 152 of *Geophysical Monograph Series*, American Geophysical Union, Washington D.C., 2004.

[29] W. Zhao and P. K. Hopke, *Atmospheric Environment*, 2004, **38**(35), 5901–5910.

[30] B. J. Finlayson-Pitts and J. C. Hemminger, *Journal of Physical Chemistry A*, 2000, **104**, 11463–11477.

[31] D. D. Weis and G. E. Ewing, *Journal of Physical Chemistry A*, 1999, **103**, 4865–4873.

[32] A. L. Goodman, G. M. Underwood, and V. H. Grassian, *Journal of Geophysical Research*, 2000, **105**(D23), 29053–29064.

[33] C. E. Jordan, J. E. Dibb, B. E. Anderson, and H. E. Fuelberg, *Journal of Geophysical Research, Atmospheres*, 2003, **108**(D21), GTE 38/1–GTE 38/10.

[34] Y. Wang, G. Zhuang, X. Zhang, K. Huang, C. Xua, A. Tang, J. Chen, and Z. An, *Atmospheric Environment*, 2006, **40**, 2935–2952.

[35] L. S. Hughes, J. O. Allen, M. J. Kleeman, R. J. Johnson, G. R. Cass, D. S. Gross, E. E. Gard, M. E. Gaelli, B. D. Morrical, D. P. Fergenson, T. Dienes, C. A. Noble, D.-Y. Liu, P. J. Silva, and K. A. Prather, *Environmental Science and Technology*, 1999, **33**(20), 3506–3515.

[36] M. Zheng, L. G. Salmon, J. J. Schauer, L. Zeng, C. S. Kiang, Y. Zhang, and G. R. Cass, *Atmospheric Environment*, 2005, **39**(22), 3967–3976.

[37] T. S. Bates, P. K. Quinn, D. J. Coffman, D. S. Covert, T. L. Miller, J. E. Johnson, G. R. Carmichael, I. Uno, S. A. Guazzotti, D. A. Sodeman, K. A. Prather, M. Rivera, L. M. Russell, and J. T. Merrill, *Journal of Geophysical Research, Atmospheres*, 2004, **109**(D19), D19S19.

[38] I. N. Tang and H. R. Munkelwitz, *Journal of Geophysical Research*, 1994, **99**(D9), 18801–18808.

[39] R. Symes, R. M. Sayer, and J. P. Reid, *Physical Chemistry Chemical Physics*, 2004, **6**, 474–487.

[40] C. T. Mills, G. A. Rowland, J. Westergren, and L. F. Phillips, *Journal of Photochemistry and Photobiology A: Chemistry*, 1996, **93**, 83–87.

[41] S. L. Wrenn, L. J. Butler, G. A. Rowland, C. J. H. Knox, and L. F. Phillips, *Journal of Photochemistry and Photobiology A: Chemistry*, 1999, **129**, 101–104.

[42] C. J. H. Knox *The Photochemistry of Liquid Aerosols* PhD thesis, University of Canterbury, 2002.

[43] C. F. Bohren and D. R. Huffman, *Absorption and scattering of light by small particles*, John Wiley and Sons, New York, 1983.

[44] P. W. Barber and S. C. Hill, *Light scattering by particles: Computational methods*, World Scientific, Singapore, 1990.

[45] A. E. Bate, *Proceedings of the Physical Society, London*, 1938, **50**, 293–297.

[46] H. Cotte, C. Devaux, and P. Carlier, *Journal of Atmospheric Chemistry*, 1997, **26**, 1–28.

[47] A. Ruggaber, R. Dlugi, A. Bott, R. Forkeli, H. Herrmann, and H. Jacobi, *Atmospheric Environment*, 1997, **31**(19), 3137–3150.

[48] L. Wind, L. Hofer, A. Nagy, P. Winkler, A. Vrtala, and W. W. Szymanski, *Aerosol Science*, 2004, **35**, 1173–1188.

[49] F. Kitagawa and N. Kitamura, *Physical Chemistry Chemical Physics*, 2002, **4**, 4495–4503.

[50] G. A. Rowland, R. van Eldik, and L. F. Phillips, *Journal of Photochemistry and Photobiology A: Chemistry*, 2002, **153**(1-3), 1–10.

[51] ed. P. Warneck, *Heterogeneous and Liquid-Phase Processes*, Vol. 2 of *Transport and Chemical Transformation of Pollutants in the Atmosphere*, Springer-Verlag, Berlin, 1995.

[52] P. Jungwirth and D. J. Tobias, *Journal of Physical Chemistry B*, 2002, **106**, 6361–6373.

[53] L. X. Dang, T.-M. Chang, M. Roeselova, B. C. Garrett, and D. J. Tobias, *Journal of Chemical Physics*, 2006, **124**, 066101.

[54] L. M. Wingen, A. C. Moskun, J. L. Thomas, M. Roeselová, D. J. Tobias, and B. J. Finlayson-Pitts, Unpublished, to be submitted to The Journal of Physical Chemistry A, 2008.

[55] D. Vione, C. Minero, A. Hamraoui, and M. Privat, *Atmospheric Environment*, 2007, **41**, 3303–3314.

[56] J. Franck and E. Rabinowitsch, *Transactions of the Faraday Society*, 1934, **30**, 120.

[57] Y. Dubowski, A. J. Colussi, C. B. Boxe, and M. R. Hoffmann, *Journal of Physical Chemistry A*, 2002, **106**, 6967–71.

[58] J. G. Calvert and J. N. Pitts, *Photochemistry*, John Wiley and Sons, New York, 1966.

[59] D. S. Covert, A. P. Waggoner, R. E. Weiss, N. C. Ahlquist, and R. J. Charlson in *The Character and Origins of Smog Aerosols*, ed. G. M. Hidy, P. K. Mueller, D. Grosjean, B. R. Appel, and J. J. Wesolowski, Vol. 9 of *Advances in Environmental Science and Technology;* John Wiley and Sons, 1980; pp. 559–581.

[60] E. M. Patterson, D. A. Gillette, and B. H. Stockton, *Journal of Geophysical Research*, 1977, **82**(21), 3153.

[61] T. Di Iorio, A. di Sarra, W. Junkermann, M. Cacciani, G. Fiocco, and D. Fua, *Journal of Geophysical Research, Atmospheres*, 2003, **108**(D10), 4316.

[62] C. Pilinis, *Journal of Geophysical Research, Atmospheres*, 1989, **94**(D7), 9937–9946.

[63] D. J. Jacob, *Atmospheric Environment*, 2000, **34**, 2131–2159.

[64] R. Haberman, *Applied partial differential equations with Fourier series and boundary value problems*, Pearson Education Inc., Upper Saddle River, New Jersey, 2004.

[65] J. Crank, *The mathematics of diffusion*, Oxford University Press, Oxford, 1956.

[66] D. Grosjean, *Environmental Science and Technology*, 1985, **79**, 1059–1065.

[67] D. Grosjean and P. H. Mc Murry, *Environmental Science and Technology*, 1985, **19**, 1176–1182.

[68] D. S. Gross, M. E. Gälli, M. Kalberer, A. S. H. Prevot, J. Dommen, M. R. Alfarra, J. Duplissy, K. Gaeggeler, A. Gascho, A. Metzger, and U. Baltensperger, *Analytical Chemistry*, 2006, **78**, 2130–2137.

[69] M. Jaoui and R. M. Kamens, *Atmospheric Environment*, 2003, **37**, 1835–1851.

[70] K. A. Ramazan, L. M. Wingen, Y. Miller, G. M. Chaban, R. B. Gerber, S. S. Xantheas, and B. J. Finlayson-Pitts, *Journal of Physical Chemistry A*, 2006, **110**, 6886–6889.

[71] T. F. Mentel, D. Bleilebens, and A. Wahner, *Atmospheric Environment*, 1996, **30**(23), 4007–4020.

[72] S. W. Hunt, M. Roeselova, W. Wang, L. M. Wingen, E. M. Knipping, D. J. Tobias, D. Dabdub, and B. J. Finlayson-Pitts, *Journal of Physical Chemistry A*, 2004, **108**, 11559–11572.

[73] M. L. Walser, J. Park, A. L. Gomez, A. R. Russell, and S. A. Nizkorodov, *Journal of Physical Chemistry A*, 2007, **111**, 1907–1913.

[74] C. Anastasio and J. T. Newberg, *Journal of Geophysical Research, Atmospheres*, 2007, **112**(D10), D10306/1–D10306/13.

[75] C. George, D. Rousse, E. Perraudiny, and R. Strekowski, *Physical Chemistry Chemical Physics*, 2003, **5**, 1562–1569.

[76] D. Grosjean, E. Grosjean, and E. L. I. Williams, *Environmental Science and Technology*, 1994, **28**, 186–196.

[77] P. Baron, Aerosol calculator Computer program, 2001.

[78] T. F. Mentel, M. Sohn, and A. Wahner, *Physical Chemistry Chemical Physics*, 1999, **1**, 5451–5457.

[79] K. Willeke and P. A. Baron, *Aerosol Measurement - Principle, Techniques and Applications*, Van Nostrand Reinhold, New York, 1993.

[80] Mks type m100b mass-flo controller and m10mb mass-flo meter, instruction manual. MKS Instruments, Inc, Wilmington, MA 01887, USA, 1999.

[81] Model 3320 aerodynamic particle sizer spectrometer instruction manual. TSI Incorporated, St. Paul, MN, USA, 1997.

[82] P. C. Reist, *Aerosol Science and Technology*, McGraw-Hill, Inc, New York, 2nd ed., 1993.

[83] Aerosol instrument manager software instruction manual. TSI Incorporated, St. Paul, MN, USA, 1997.

[84] J. Mitchell in *Physical and Chemical Properties of Aerosols;* Blackie Academic and Professional, London, 1998; p. 34.

[85] A. J. Armendiraz and D. Leith, *Aerosol Science*, 2002, **33**, 133–148.

[86] Matlab. The MathWorks, Natick, MA 01760, U.S.A., 2002.

[87] W. W. Hines and D. C. Montgomery, *Probability and Statistics in Engineering and Management Science*, John Wiley and Sons, Inc, New York, 1980.

[88] D. L. Harnett, *Introduction to Statistical Methods*, Addison-Wesley Publishing Company, Inc., Reading, Massachusetts, U.S.A., 2nd ed., 1975.

[89] K. T. Whitby and G. M. Sverdrup in *The Character and Origins of Smog Aerosols*, ed. G. M. Hidy, P. K. Mueller, D. Grosjean, B. R. Appel, and J. J. Wesolowski, Vol. 9 of *Advances in Environmental Science and Technology;* John Wiley and Sons, 1980; pp. 477–518.

[90] P. Atkins, *Physical Chemistry (4th Ed)*, Oxford University Press, Oxford, 4th ed., 1990.

[91] A. J. Allmand and W. W. Webb, *Journal of the Chemical Society*, 1929, pp. 1518–31,1531–7.

[92] C. G. Hatchard and C. A. Parker, *Proceedings of the Royal Society (London)*, 1956, **A235**, 518.

[93] K. A. Hislop and J. R. Bolton, *Environmental Science and Technology 1999, 33, 3119-3126*, 1999, **33**, 3119–3126.

[94] H. A. Taylor in *Analytical Photochemistry and Photochemical Analysis*, ed. J. M. Fitzgerald; Marcel Dekker Inc., New York, 1971.

[95] J. F. Rabek, *Experimental Methods in Photochemistry and Photophysics*, John Wiley and Sons, Chichester, 1982.

[96] H. J. Kuhn, S. E. Braslavsky, and R. Schmidt, *Pure Applied Chemistry*, 2004, **76**(12), 2105–2146.

[97] C. Anastasio and K. G. McGregor, *Atmospheric Environment*, 2001, **35**, 1079–1089.

[98] J. J. Jankowski, D. J. Kieber, and K. Mopper, *Photochemistry and Photobiology*, 1999, **70**(3), 319–328.

[99] R. C. Johnson, *Journal of Chemical Education*, 1970, **47**(10), 702.

[100] K. L. Willett and R. A. Hites, *Journal of Chemical Education*, 2000, **77**(7), 900–902.

[101] A. D. Kirk and C. Namasivayam, *Analytical Chemistry*, 1983, **55**, 2428–2429.

[102] Technical supplement ppt-1a. The NGS Division of MKS Instruments, Inc, Walpole, MA, USA, 1993.

[103] E. M. Knipping, M. J. Lakin, K. L. Foster, P. Jungwirth, D. J. Tobias, R. B. Gerber, D. Dabdub, and B. J. Finlayson-Pitts, *Science (Washington, D. C.)*, 2000, **288**(5464), 301–306.

[104] Microsoft office excel. Microsoft Corporation, Bellevue, WA 98004 U.S.A., 2003.

[105] R. Atkinson, D. L. Baulch, R. A. Cox, J. N. Crowley, R. F. Hampson, R. G. Hynes, M. E. Jenkin, M. J. Rossi, and J. Troe, *Atmospheric Chemistry and Physics*, 2006, **6**, 3625–4055.

[106] K. A. Ramazan, D. Syomin, and B. J. Finlayson-Pitts, *Physical Chemistry Chemical Physics*, 2004, **6**, 3836–3843.

[107] R. Atkinson, *Atmospheric Chemistry and Physics*, 2003, **3**, 2233–2307.

[108] S. M. Aschmann, J. Arey, and R. Atkinson, *Atmospheric Environment*, 1996, **30**(17), 2939–2943.

[109] ed. D. R. Lide, *CRC Handbook of Chemistry and Physics*, CRC Press, Boca Raton, FA, USA, 73rd ed., 1992.

[110] G. Heimann and P. Warneck, *International Journal of Chemical Kinetics*, 2006, **38**(11), 677–688.

[111] D. V. Vione, V. Maurino, C. Minero, M. Lucchiari, and E. Pelizzetti, *Chemosphere*, 2004, **56**, 1049–1059.

[112] R. Zellner, M. Exner, and H. Herrmann, *Photochemistry and Photobiology*, 1990, **10**, 411–425.

[113] V. R. Meyer, *Practical High-Performance Liquid Chromatography*, John Wiley and Sons, Chichester, 2nd ed., 1994.

[114] Chromeleon. Dionex Corporation, Sunnyvale, CA 94085, U.S.A., 2006.

[115] L. Chu and C. Anastasio, *Journal of Physical Chemistry A*, 2005, **109**, 6264–6271.

[116] L. Ashton, G. V. Buxton, and C. R. Stuart, *Journal of the Chemistry Society, Faraday Transactions*, 1995, **91**(11), 1631–1633.

[117] G. Mark, H.-P. Schuchmann, L. Prager, and C. von Sonntag, *Environmental Science and Technology*, 2003, **37**, Environ. Sci. Technol. 2003, 37, 372–378.

[118] K. R. May, *Aerosol Science*, 1973, **4**, 235–243.

[119] J. N. Pearce and A. F. Nelson, *Journal of the American Chemical Society*, 1932, **54**, 3544.

[120] S. M. Aschmann, A. A. Chew, J. Arey, and R. Atkinson, *Journal of Physical Chemistry A*, 1997, **101**, 8042–8048.

[121] F. P. Laming, G. Buxton, and W. K. Wilmarth, *Journal of Physical Chemistry*, 1969, **73**(4), 867–873.

[122] K. H. Gertz and H. H. Loeschcke, *Zeitschrift für Naturforschung*, 1956, **11b**, 61–64.

[123] B. Alexander, R. J. Park, D. J. Jacob, Q. B. Li, and R. M. Yantosca, *Journal of Geophysical Research*, 2005, **110**(D10307).

[124] A. Laskin, D. J. Gaspar, W. Wang, J. P. Hunt, Sherri W. Cowin, S. D. Colson, and B. J. Finlayson-Pitts, July , 2003, **301**(5631), 340.

[125] H. Shaka, W. H. Robertson, and B. J. Finlayson-Pitts, *Physical Chemistry Chemical Physics*, 2007, **9**, 1980–1990.

[126] R. Vogt, P. J. Crutzen, and R. Sander, *Nature*, 1996, **383**, 327–330.

[127] E. P. A. Emission Measurement Centre.